Available online at www.sciencedirect.com

ScienceDirect

Surface Science Reports 70 (2015) 1–41

surface science reports

www.elsevier.com/locate/surfrep

Electromagnetic density of states in complex plasmonic systems

R. Carminati[a,*], A. Cazé[b], D. Cao[a], F. Peragut[a], V. Krachmalnicoff[a], R. Pierrat[a], Y. De Wilde[a]

[a]ESPCI ParisTech, PSL Research University, CNRS, Institut Langevin, 1 rue Jussieu, F-75238 Paris, France
[b]Department of Mathematics, University of Michigan, Ann Arbor, MI 48109, USA

Received 18 September 2014; received in revised form 30 October 2014; accepted 24 November 2014

Abstract

Nanostructured materials offer the possibility to tailor light–matter interaction at scales below the wavelength. Metallic nanostructures benefit from the excitation of surface plasmons that permit light concentration at ultrasmall length scales and ultrafast time scales. The local density of states (LDOS) is a central concept that drives basic processes of light–matter interaction such as spontaneous emission, thermal emission and absorption. We introduce theoretically the concept of LDOS, emphasizing the specificities of plasmonics. We connect the LDOS to real observables in nanophotonics, and show how the concept can be generalized to account for spatial coherence. We describe recent methods developed to probe or map the LDOS in complex nanostructures ranging from nanoantennas to disordered metal surfaces, based on dynamic fluorescence measurements or on the detection of thermal radiation.

Keywords: Local density of states; Plasmonics; Spontaneous emission; Thermal radiation; Spatial coherence; Cross density of states

Contents

*Corresponding author.
E-mail address: remi.carminati@espci.fr (R. Carminati).

http://dx.doi.org/10.1016/j.surfrep.2014.11.001
0167-5729/

1. Introduction

Plasmonics couples surface plasmon excitations [1,2] with nanostructures in view of enhancing and controlling light emission and absorption at small length and time scales. This field of research has become an important branch of nano-optics [3,4], and several reviews have been published, describing developments towards applications in integrated subwavelength photonics [5–7], light concentration and manipulation at the nanoscale [8–10] including the design of optical antennas [11], active [12] and quantum plasmonics [13]. Our goal here is not to present another review of the field of plasmonics, but rather to revisit fundamental aspects based on the unifying concept of density of states. Measuring and engineering the electromagnetic local density of states (LDOS) in plasmonic structures is a major issue, since the LDOS drives basic processes of light–matter interaction such as spontaneous emission (fluorescence), thermal emission and absorption. New possibilities are emerging for the design of efficient sources and absorbers of visible and infrared radiation, for optical storage and information processing with ultrahigh spatial density, or for the development of nanoscale markers for biomedical imaging and therapy. In the last decade, methods have emerged that enable us to map the LDOS on nanostructured surfaces, or to engineer the LDOS in order to control light emission by single quantum sources. On the theoretical side, the concept of LDOS itself has been clarified to better account for specific features of the optics of metal surfaces, for example regarding the electric and magnetic contributions, or the splitting into radiative and non-radiative components. The purpose of this review article is to give a self-contained presentation of the concept of LDOS and of the connection between the LDOS and real observables in optics, and a state-of-the-art description of the methods permitting to probe or map the LDOS in real structures (from nanoantennas to complex disordered surfaces). The extension of the concept of density of states to include a description of spatial coherence, through the introduction of a cross density of states (CDOS), is also introduced. The concepts of LDOS and CDOS allow us to connect different aspects of plasmonics in complex structured geometries. They also help establishing connections with other fields of wave physics, in which wave–matter interaction is controlled by similar quantities.

2. Electromagnetic local density of states

2.1. Non-absorbing closed cavity: a canonical example

The concepts of density of states (DOS) and local density of states (LDOS) can be introduced starting from the textbook situation of a non-absorbing and non-dispersive medium embedded in a closed cavity with volume $V = L^3$ (it is usually

assumed that $L \ll \lambda$, λ being the wavelength in vacuum). In such a situation, a discrete set of eigenmodes of the vector Helmholtz equation can be introduced [14]. The mathematical procedure is detailed in Appendix A.1, and here we summarized the useful results. The eigenvectors $\mathbf{e}_n(\mathbf{r})$ and eigenfrequencies ω_n are solutions of the vector Helmholtz equation

$$\nabla \times \nabla \times \mathbf{e}_n(\mathbf{r}) - \epsilon(\mathbf{r}) \frac{\omega_n^2}{c^2} \mathbf{e}_n(\mathbf{r}) = 0 \tag{1}$$

where $\epsilon(\mathbf{r})$ is the dielectric function of the medium and c the speed of light in vacuum. The eigenmodes also obey the orthogonality condition

$$\int_V \epsilon(\mathbf{r}) \mathbf{e}_m(\mathbf{r}) \cdot \mathbf{e}_n^*(\mathbf{r})\, \mathrm{d}^3 r = \delta_{mn} \tag{2}$$

where the superscript $*$ stands for complex conjugate.

The DOS $\rho(\omega)$ at a frequency ω counts the number of eigenmodes in an infinitely small frequency range, and is defined as

$$\rho(\omega) = \frac{1}{V} \sum_n \delta(\omega - \omega_n). \tag{3}$$

This DOS is a global quantity that characterizes the spectral density of eigenmodes of the medium as a whole. A local quantity $\rho_e(\mathbf{r}, \omega)$ (LDOS) can be introduced, through a summation weighted by the amplitude of the eigenmodes at point $\mathbf{r}$:

$$\rho_e(\mathbf{r}, \omega) = \sum_n |\mathbf{e}_n(\mathbf{r})|^2 \delta(\omega - \omega_n). \tag{4}$$

This relation defines the LDOS in the particular case of a medium for which a discrete set of eigenmodes can be introduced. The subscript e is used since this definition of the LDOS is based on the eigenmodes of the Helmholtz equation written in terms of the electric field. A LDOS defined in terms of the magnetic field will be introduced later.

Another expression of the (electric) LDOS can be established, using the electric Green function $\mathbf{G}^E(\mathbf{r}, \mathbf{r}', \omega)$ of the vector Helmholtz equation. The electric Green function is defined as the solution of

$$\nabla \times \nabla \times \mathbf{G}^E(\mathbf{r}, \mathbf{r}', \omega) - \epsilon(\mathbf{r}) \frac{\omega^2}{c^2} \mathbf{G}^E(\mathbf{r}, \mathbf{r}', \omega) = \delta(\mathbf{r} - \mathbf{r}')\mathbf{I} \tag{5}$$

where $\mathbf{I}$ is the unit tensor, together with appropriate boundary conditions on the surface of the closed cavity (the boundary conditions are the same as that satisfied by the electric field). The Green function defined this way has a simple physical interpretation: For a monochromatic point electric-dipole source $\mathbf{p}$ located at a position $\mathbf{r}'$, the electric field radiated at a point $\mathbf{r}$ is $\mathbf{E}(\mathbf{r}) = \mu_0 \omega^2 \mathbf{G}^E(\mathbf{r}, \mathbf{r}', \omega)\mathbf{p}$. A magnetic Green function will be introduced later, connecting a magnetic dipole source to the radiated magnetic field.

In terms of the eigenmodes introduced above, the Green function can be written as (the derivation is given in Appendix A.1)

$$\mathbf{G}^E(\mathbf{r}, \mathbf{r}', \omega) = \sum_n c^2 \mathbf{e}_n^*(\mathbf{r}') \otimes \mathbf{e}_n(\mathbf{r}) \times \left[\mathrm{PV}\left(\frac{1}{\omega_n^2 - \omega^2} \right) + \frac{i\pi}{2\omega_n} \delta(\omega - \omega_n) \right] \tag{6}$$

where PV stands for principal value. This expression is often cast in the simplified form

$$\mathbf{G}^E(\mathbf{r}, \mathbf{r}', \omega) = \sum_n c^2 \frac{\mathbf{e}_n^*(\mathbf{r}') \otimes \mathbf{e}_n(\mathbf{r})}{\omega_n^2 - \omega^2} \tag{7}$$

in which the splitting into a principal value and a singular part is implicit. From Eqs. (4) and (6), one can rewrite the LDOS in the form

$$\rho_e(\mathbf{r}, \omega) = \frac{2\omega}{\pi c^2} \mathrm{Im}\left[\mathrm{Tr}\, \mathbf{G}^E(\mathbf{r}, \mathbf{r}, \omega) \right] \tag{8}$$

where Tr denotes the trace of a tensor.

2.2. LDOS and Green's function: general definition

The simplicity of the expression of the LDOS in terms of the imaginary part of the Green function is striking. In particular, it shows that the correct counting of eigenmodes is implicit in the Green function, although the latter can be computed by solving the Helmholtz equation without referring to any set of eigenmodes. In the most general case of an open absorbing medium, described by a complex frequency-dependent dielectric function $\epsilon(\mathbf{r}, \omega)$, the Green function can be defined as the solution of

$$\nabla \times \nabla \times \mathbf{G}^E(\mathbf{r}, \mathbf{r}', \omega) - \epsilon(\mathbf{r}, \omega) \frac{\omega^2}{c^2} \mathbf{G}^E(\mathbf{r}, \mathbf{r}', \omega) = \delta(\mathbf{r} - \mathbf{r}')\mathbf{I} \tag{9}$$

satisfying an outgoing wave condition (Sommerfeld's radiation condition) when $k_0 |\mathbf{r} - \mathbf{r}'| \to \infty$, with $k_0 = \omega/c = 2\pi/\lambda$ (this Green function is sometimes denoted by retarded Green function). In an open geometry and/or in the presence of lossy materials, a basis of eigenmodes cannot be defined based on the canonical approach for Hermitian operators. Although the eigenmodes picture can be recovered using appropriate procedures even for open and lossy systems [15,16], the Green function approach has the advantage to be unambiguously defined. Therefore we use Eq. (8) as a *definition* of the LDOS in an arbitrary environment. This definition does not assume any particular set of eigenmodes. Let us also note that we restrict in this review the discussion of the LDOS calculated, or measured, at a point $\mathbf{r}$ lying in vacuum, although this point might be at close proximity from a material surface, including the surface of an absorbing metal. In these conditions, the imaginary part of the Green function at $\mathbf{r} = \mathbf{r}'$ is non-singular and the LDOS in Eq. (8) is a well-defined quantity [17].

3. Dipole radiation, spontaneous decay rate and LDOS

The relevance of the LDOS introduced in the previous section in terms of Green's functions becomes apparent in the

study of classical radiation and quantum spontaneous emission by an electric dipole.

3.1. Power radiated by a classical oscillator

Radiation by a point electric dipole source is a standard problem in classical electrodynamics [18]. In the monochromatic regime, the time-averaged power transferred from a source described by a current density $\mathbf{j}(\mathbf{r})$ to the electromagnetic field is

$$P = -\frac{1}{2}\,\mathrm{Re}\int \mathbf{j}^*(\mathbf{r})\cdot\mathbf{E}(\mathbf{r})\,\mathrm{d}^3r. \tag{10}$$

For a point electric-dipole source located at a position $\mathbf{r}_s$, the current density is $\mathbf{j}(\mathbf{r}) = -i\omega\mathbf{p}\delta(\mathbf{r}-\mathbf{r}_s)$, so that

$$P = \frac{\omega}{2}\,\mathrm{Im}\left[\mathbf{p}^*\cdot\mathbf{E}(\mathbf{r}_s)\right] \tag{11}$$

where $\mathbf{E}(\mathbf{r}_s)$ is the field at the position of the dipole. Using the Green function $\mathbf{G}^E(\mathbf{r},\mathbf{r}_s,\omega)$ the emitted power can be rewritten in the form

$$P = \frac{\mu_0\omega^3}{2}|\mathbf{p}|^2\,\mathrm{Im}\left[\mathbf{u}\cdot\mathbf{G}^E(\mathbf{r}_s,\mathbf{r}_s,\omega)\mathbf{u}\right] \tag{12}$$

with $\mathbf{u}$ being the unit vector along the direction of the dipole. In this expression we assume that the source point $\mathbf{r}_s$ is located in vacuum, but the Green function $\mathbf{G}^E(\mathbf{r},\mathbf{r}_s,\omega)$ can describe an arbitrary environment surrounding the emitter. In particular, the power P calculated in this way accounts both for far-field radiation and absorption in the environment.

In the case of a dipole with a fixed orientation $\mathbf{u}$, we can define a *projected* LDOS (sometimes denoted by *partial* LDOS) [3]:

$$\rho_{e,\mathbf{u}}(\mathbf{r}_s,\omega) = \frac{2\omega}{\pi c^2}\,\mathrm{Im}\left[\mathbf{u}\cdot\mathbf{G}^E(\mathbf{r}_s,\mathbf{r}_s,\omega)\mathbf{u}\right]. \tag{13}$$

In terms of the projected LDOS, the emitted power can be rewritten in the form

$$P = \frac{\pi\omega^2}{4\epsilon_0}|\mathbf{p}|^2\rho_{e,\mathbf{u}}(\mathbf{r}_s,\omega). \tag{14}$$

The projected LDOS accounts for radiation by an electric dipole with a given orientation. The full LDOS

$$\rho_e(\mathbf{r}_s,\omega) = \sum_{\mathbf{u}=\mathbf{u}_x,\mathbf{u}_y,\mathbf{u}_z}\rho_{e,\mathbf{u}}(\mathbf{r}_s,\omega) = \frac{2\omega}{\pi c^2}\,\mathrm{Im}\left[\mathrm{Tr}\;\mathbf{G}^E(\mathbf{r}_s,\mathbf{r}_s,\omega)\right] \tag{15}$$

describes the emitted power summed up over the three directions $\mathbf{u}_x,\mathbf{u}_y,\mathbf{u}_z$ of the dipole.

In the particular case of a dipole placed in free space, the power transferred to the environment equals the power radiated to far-field radiation. It can be obtained from the free-space dyadic Green function $\mathbf{G}_0(\mathbf{r},\mathbf{r}_s,\omega)$, whose imaginary part at $\mathbf{r}=\mathbf{r}_s$ is simply [19,20]

$$\mathrm{Im}[\mathbf{G}_0(\mathbf{r}_s,\mathbf{r}_s,\omega)] = \frac{k_0}{6\pi}\,\mathbf{I}. \tag{16}$$

The projected and full LDOS in vacuum are readily deduced:

$$\rho_{\mathbf{u},0}(\mathbf{r}_s,\omega) = \frac{\omega^2}{3\pi^2c^3},\quad \rho_0(\mathbf{r}_s,\omega) = \frac{\omega^2}{\pi^2c^3}. \tag{17}$$

From Eqs. (14) and (17), we recover the well-known expression of the power emitted by an electric dipole in free space [18]:

$$P_0 = \frac{\omega^4}{12\pi\epsilon_0c^3}|\mathbf{p}|^2. \tag{18}$$

Finally let us point out that starting from the radiation by a magnetic point dipole, a magnetic contribution to the LDOS can be introduced following the same lines, with a Green function describing the magnetic field radiated by a magnetic dipole [21]. The existence of electric and magnetic contributions to the LDOS is discussed in Section 5.2.

3.2. Spontaneous decay rate of a quantum emitter

In the weak-coupling regime, the population of the excited state of a quantum emitter decays exponentially in time, with a characteristic time (fluorescence lifetime) $\tau = \Gamma^{-1}$, where Γ is the spontaneous decay rate. The latter can be calculated from first-order perturbation theory [22,23]. Here we give a heuristic derivation of the expression of the spontaneous decay rate, based on correspondence arguments [24].

We consider a two-level system with excited state $|e\rangle$ and ground state $|g\rangle$, Bohr frequency ω_{eg}, and transition dipole $\mathbf{p}_{eg} = \langle g|\mathbf{D}|e\rangle$, $\mathbf{D}$ being the electric dipole operator. Starting from the time-averaged power emitted by a classical dipole equation (12), with ω replaced by the Bohr frequency ω_{eg}, we can obtain the decay rate (averaged number of quantum transitions per unit time) by dividing the power by the quantum energy $\hbar\omega_{eg}$, and replacing the classical dipole moment $\mathbf{p}$ by the transition dipole $\mathbf{p}_{eg}$. The substitution of $\mathbf{p}$ by $\mathbf{p}_{eg}$ includes a factor of two since only positive frequencies have to be handled in the emission problem (in quantum mechanics positive and negative are treated specifically), while the classical treatment involves both positive and negative frequencies. This simple procedure leads to

$$\Gamma = \frac{2\mu_0\omega_{eg}^2}{\hbar}|\mathbf{p}_{eg}|^2\,\mathrm{Im}\left[\mathbf{u}\cdot\mathbf{G}^E\left(\mathbf{r}_s,\mathbf{r}_s,\omega_{eg}\right)\mathbf{u}\right] \tag{19}$$

where $\mathbf{r}_s$ is the position of the emitter.

It is striking to note that this result coincides exactly with that obtained from the quantum electrodynamics calculation based on perturbation theory [3,22,23]. In terms of the projected LDOS $\rho_{e,\mathbf{u}}$, it can also be rewritten as

$$\Gamma = \frac{\pi\omega_{eg}}{\hbar\epsilon_0}|\mathbf{p}_{eg}|^2\rho_{e,\mathbf{u}}\left(\mathbf{r},\omega_{eg}\right) \tag{20}$$

which takes the form of Fermi's golden rule. In the particular case of free space, the projected LDOS is given in Eq. (17) and the spontaneous decay rate reads

$$\Gamma_0 = \frac{\omega_{eg}^3}{3\pi\hbar\epsilon_0c^3}|\mathbf{p}_{eg}|^2 \tag{21}$$

which is the known result for the spontaneous decay rate of a two-level system in vacuum.

3.3. Purcell factor

The change in the spontaneous decay rate Γ/Γ_0 due to a structured environment was computed by Purcell long ago in the case of a single mode cavity [25]. We show that the formalism introduced above includes Purcell's expression of Γ/Γ_0 as a particular case.

To proceed, we start from the expression of the Green function equation (7) for a perfect lossless cavity. In the presence of dissipation, mode attenuation can be accounted for using a phenomenological approach [26]. One introduces a mode damping rate γ_n and modifies Eq. (7) in the following way:

$$\mathbf{G}^E(\mathbf{r},\mathbf{r}',\omega)=\sum_n c^2\frac{\mathbf{e}_n^*(\mathbf{r}')\mathbf{e}_n(\mathbf{r})}{\omega_n^2-\omega^2-i\omega\gamma_n}. \tag{22}$$

Following the initial formulation by Purcell, we assume that the emitter is resonant with one of the eigenmodes ($\omega_{eg}=\omega_n$), so that the Green function is dominated by the contribution of this specific eigenmode. From Eqs. (19) and (22) we obtain

$$\Gamma=\frac{2}{\epsilon_0\hbar}|\mathbf{p}_{eg}|^2Q|\mathbf{e}_n(\mathbf{r}_s)\cdot\mathbf{u}|^2 \tag{23}$$

the factor $Q=\omega_{eg}/\gamma_n$ being the quality factor associated to mode n. One can also define the mode volume seen by the emitter at point $\mathbf{r}_s$ by the relation

$$\frac{1}{V}=|\mathbf{e}_n(\mathbf{r}_s)\cdot\mathbf{u}|^2 \tag{24}$$

recalling that $|\mathbf{e}_n(\mathbf{r}_s)|^2$ has the unit of a volume due to the orthogonality condition equation (2). Using the expression (21) for the spontaneous decay rate in vacuum, the normalized decay rate can finally be written as

$$\frac{\Gamma}{\Gamma_0}=\frac{3}{4\pi^2}\lambda_{eg}^3\frac{Q}{V} \tag{25}$$

where $\lambda_{eg}=2\pi c/\omega_{eg}$. This is the result given by Purcell [25], and the right-hand side is usually referred to as the Purcell factor. Note that in the original formulation by Purcell, the emitter is supposed to stand at the point $\mathbf{r}_{\max}$ coinciding with the maximum of amplitude of the mode, so that $V^{-1}=|\mathbf{e}_n(\mathbf{r}_{\max},\omega_{eg})\cdot\mathbf{u}|^2$ (this maximizes the Purcell factor).

Although the definition of the mode volume is clear in the case of a system for which a discrete basis of eigenmodes can be defined, its expression in the general case of an open and absorbing medium has been the subject of recent discussions in plasmonics [15,27,28]. It is useful to note that the splitting of Γ/Γ_0 into a contribution from a quality factor Q and a mode volume V is somewhat arbitrary, since there is no reason for these two parameters to be independent (even for the simplest example of a Fabry–Pérot cavity). Actually, the relevant parameter for the change in the decay rate is the LDOS (including radiative and non-radiative contributions), that in the particular case of a single mode cavity is proportional to the ratio Q/V.

A general expression of the normalized decay rate Γ/Γ_0 can be obtained from Eqs. (19) and (21), and reads as

$$\frac{\Gamma}{\Gamma_0}=\frac{6\pi c}{\omega_{eg}}\,\mathrm{Im}\left[\mathbf{u}\cdot\mathbf{G}^E(\mathbf{r}_s,\mathbf{r}_s,\omega_{eg})\mathbf{u}\right]. \tag{26}$$

The right-hand side can be understood as a generalized Purcell factor. This expression applies for any system, including open absorbing media that are usually encountered in plasmonics. It leads to the historical Purcell factor in the particular case of a single mode cavity. It is also interesting to note that from the power emitted by a classical dipole, the same result is obtained. Using Eqs. (12) and (18), the normalized emitted power P/P_0 is readily obtained:

$$\frac{P}{P_0}=\frac{6\pi c}{\omega}\,\mathrm{Im}\left[\mathbf{u}\cdot\mathbf{G}^E(\mathbf{r}_s,\mathbf{r}_s,\omega)\mathbf{u}\right]. \tag{27}$$

The generalized Purcell factor also shows up in the expression of the normalized power emitted by a classical dipole antenna. In the usual antenna formalism, this factor can be understood as a change in the impedance of the medium. This connects the change in the spontaneous decay rate of a quantum emitter to the change in the impedance seen by a classical dipole antenna, as pointed out in Ref. [29].

3.4. Strong coupling regime

Beyond the weak-coupling regime that is at the center of this review, the strong coupling regime also attracts attention in nanophotonics and plasmonics. Strong coupling between a quantum emitter and the electromagnetic field is characterized by Rabi oscillations of the excited-state population, or a splitting in the frequency spectrum of the emitted light. Reaching this regime with solid-state cavities is a crucial issue for, e.g. quantum information processing. Nanophotonics provides new ways of reaching the strong coupling regime, by using integrated photonic cavities (microcavities or photonic crystal cavities) [30–32], or surface-plasmon modes on metallic nanoparticles or substrates [33–37]. Surface plasmons are appealing since they provide subwavelength light confinement without a physical cavity, a price to pay being the large absorption losses that reduce the Q factor. Another approach is to use light confinement in disordered media induced by the process of Anderson localization, which is established for light at least in 1D and 2D geometries [38–40]. It is interesting to note that a criterion for strong coupling amounts to comparing the coupling strength to the losses of the cavity (either the real physical cavity or the virtual cavity created by the confined plasmon or the Anderson localized mode). This criterion involves the Purcell factor, and creating large Purcell factors is a key issue in view of reaching the strong coupling regime [34,40]. Therefore, although the Purcell factor is a weak-coupling concept, engineering the LDOS to increase its value is of interest beyond weak-coupling experiments.

3.5. Radiative and non-radiative decay

The decay rate Γ integrates all possible decay channels available for spontaneous emission. Radiative channels correspond to far-field emission of a real photon, while non-radiative channels correspond to absorption (dissipation in the material degrees of freedom). A measurement of the lifetime τ of the excited state of a fluorescent emitter provides a direct measurement of $\Gamma = \tau^{-1}$. Conversely, the fluorescence intensity (photocounts) is controlled by several parameters that depend on the environment, such as the excitation rate and the apparent quantum yield η, that gives the probability of radiative decay. The apparent quantum yield (i.e. accounting for both internal non-radiative channels and non-radiative processes induced by the environment) is defined as

$$\eta = \frac{\Gamma^{\mathrm{R}}}{\Gamma^{\mathrm{R}} + \Gamma^{\mathrm{NR}}_{\mathrm{int}} + \Gamma^{\mathrm{NR}}} \tag{28}$$

where Γ^{R} is the radiative decay rate, $\Gamma^{\mathrm{NR}}_{\mathrm{int}}$ is the intrinsic non-radiative rate, and Γ^{NR} is the non-radiative rate induced by the environment (e.g. absorption by a metallic structure). In the case of an emitter with an intrinsic quantum yield close to unity, the intrinsic non-radiative rate $\Gamma^{\mathrm{NR}}_{\mathrm{int}}$ can be neglected.

The radiative and non-radiative decay rates Γ^{R} and Γ^{NR} can be defined using the connection with classical theory. For a classical dipole, one can split the total emitted power P into a radiative and a non-radiative contribution. The radiative contribution P^{R} corresponds to the power radiated to the far field, and reads as

$$P^{\mathrm{R}} = \int_S \frac{\epsilon_0 c}{2} |\mathbf{E}(\mathbf{r})|^2 \, \mathrm{d}^2 r \tag{29}$$

where S is the surface of a sphere with radius $R \to \infty$ enclosing the medium. The non-radiative contribution P^{NR} corresponds to absorption in the environment, and reads

$$P^{\mathrm{NR}} = \int \frac{\omega \epsilon_0}{2} \mathrm{Im}[\epsilon(\mathbf{r}, \omega)] |\mathbf{E}(\mathbf{r})|^2 \, \mathrm{d}^3 r \tag{30}$$

where the integral runs over the entire space. Since from Eqs. (26) and (27) we have

$$\frac{P}{P_0} = \frac{\Gamma}{\Gamma_0} \tag{31}$$

provided that the classical frequency ω coincides with the Bohr frequency ω_{eg}, we can define the radiative and non-radiative decay rates by their connection with classical quantities:

$$\frac{\Gamma^{\mathrm{R}}}{\Gamma_0} = \frac{P^{\mathrm{R}}}{P_0} \quad \text{and} \quad \frac{\Gamma^{\mathrm{NR}}}{\Gamma_0} = \frac{P^{\mathrm{NR}}}{P_0}. \tag{32}$$

The relative weight of radiative and non-radiative contributions in the decay rate is a key issue in plasmonics [41].

Since the decay rate is proportional to the LDOS, it is possible to define a radiative and a non-radiative contributions to the LDOS:

$$\rho_e(\mathbf{r}, \omega) = \rho_e^{\mathrm{R}}(\mathbf{r}, \omega) + \rho_e^{\mathrm{NR}}(\mathbf{r}, \omega). \tag{33}$$

A similar splitting can also be used for the projected LDOS $\rho_{e,\mathbf{u}}(\mathbf{r}, \omega)$.

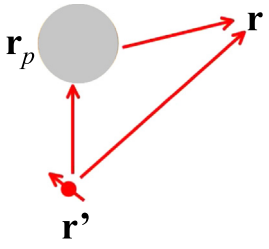

Fig. 1. Schematic diagram showing the two contributions involved in the calculation of the Green function $\mathbf{G}^E(\mathbf{r}, \mathbf{r}', \omega)$ in the presence of a nanoparticle centered at point $\mathbf{r}_p$.

3.6. Dipole–dipole interaction

One of the simplest models in which changes in spontaneous decay rates induced by the environment can be calculated analytically is that of a single dipole emitter interacting with a single nanoparticle, treated itself in the electric-dipole approximation. Provided that the distance between the emitter and the nanoparticle remains larger than approximately two times its radius a, this model gives accurate predictions [42]. It is also useful in providing physical insight and general trends. At short distances from particles or surfaces, more refined models are necessary that take into account multipole interactions and/or microscopic material responses including non-local effects [42–45].

The computation of the decay rate, or equivalently of the LDOS, requires the computation of the (electric) Green function $\mathbf{G}^E(\mathbf{r}, \mathbf{r}', \omega)$ in the presence of the nanoparticle. Following a previous work [20], we describe the nanoparticle response by its electric polarizability including radiative reaction, that takes the form

$$\alpha(\omega) = \frac{\alpha_0(\omega)}{1 - i\dfrac{k_0^3}{6\pi}\alpha_0(\omega)} \tag{34}$$

where $\alpha_0(\omega)$ is the quasi-static polarizability, that for a spherical particle with radius a is given by

$$\alpha_0(\omega) = 4\pi a^3 \frac{\epsilon(\omega) - 1}{\epsilon(\omega) + 2} \tag{35}$$

with $\epsilon(\omega)$ being the dielectric function describing the material composing the nanoparticle. This form of the dynamic polarizability $\alpha(\omega)$ is consistent with energy conservation (optical theorem) [46]. For $\mathrm{Re}[\epsilon(\omega)] \simeq -2$, the quasi-static polarizability exhibits a resonance, that for a metal is the plasmon resonance associated to oscillations of the confined free electron gas. The radiative correction in the dynamic polarizability slightly changes both the frequency and the linewidth of the resonance [47].

The Green function accounts for the two contributions represented diagramatically in Fig. 1. It reads as

$$\mathbf{G}^E(\mathbf{r}, \mathbf{r}', \omega) = \mathbf{G}_0(\mathbf{r}, \mathbf{r}', \omega) + \mathbf{G}_0(\mathbf{r}, \mathbf{r}_p, \omega)\alpha(\omega)k_0^2 \, \mathbf{G}_0(\mathbf{r}_p, \mathbf{r}', \omega) \tag{36}$$

where $\mathbf{G}_0$ is the free-space Green function and $\mathbf{r}_p$ is the position of the center of the nanoparticle. The free-space Green function $\mathbf{G}_0$ is given by [19]

$$\mathbf{G}_0(\mathbf{r},\mathbf{r}',\omega) = \mathrm{PV}\left[\mathbf{I} + \frac{1}{k_0^2}\nabla\otimes\nabla\right]\frac{\exp(ik_0R)}{4\pi R} - \frac{\mathbf{I}}{3k_0^2}\delta(R) \qquad (37)$$

where $\mathbf{I}$ is the unit dyadic and $R = |\mathbf{r}-\mathbf{r}'|$.

From Eqs. (13), (36) and (37), the projected LDOS and the full LDOS can be calculated in the vicinity of the nanoparticle. Moreover, since the Green function is known for arbitrary points $\mathbf{r}$ and $\mathbf{r}'$, the electric field $\mathbf{E}(\mathbf{r})$ can be calculated everywhere and the radiative and non-radiative contributions can be calculated separately using Eqs. (29)–(33). In the dipole–dipole coupling model, the calculation leads to analytical results [20]. A typical behavior is shown in Fig. 2. The distance dependence of the projected LDOS, and of its radiative and non-radiative components, is plotted in the vicinity of a silver nanoparticle (diameter 10 nm) for a wavelength off-resonance (a) and for a wavelength coinciding with the plasmon resonance (b). In Fig. 2(a), the projected LDOS $\rho_{e,\mathbf{u}}$ increases at short distance from the nanoparticle. From the distance dependence of the radiative ($\rho^{\mathrm{R}}_{e,\mathbf{u}}$) and non-radiative ($\rho^{\mathrm{NR}}_{e,\mathbf{u}}$) LDOS, it is also clear that the increase at short distance is dominated by non-radiative coupling. The trends remain identical in Fig. 2(b) where the plasmon resonance of the nanoparticle is excited, with enhanced modifications of the LDOS [note the change in scales on both axes compared to Fig. 2(a)].

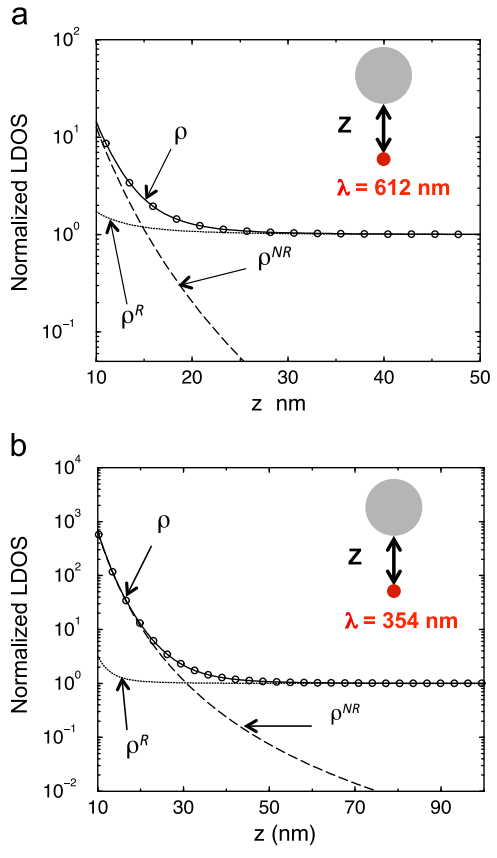

Fig. 2. Normalized LDOS $\rho_{e,\mathbf{u}}/\rho_0$, radiative LDOS $\rho^{\mathrm{R}}_{e,\mathbf{u}}/\rho_0$ and non-radiative LDOS $\rho^{\mathrm{NR}}_{e,\mathbf{u}}/\rho_0$ versus the distance z to a silver nanoparticle with diameter $d=10$ nm. All LDOS are projected LDOS along the direction $\mathbf{u}=\mathbf{e}_z$ pointing towards the nanoparticle. (a) Wavelength $\lambda=612$ nm (off resonance). Dielectric function of silver $\epsilon(612\text{ nm}) = -15.04+1.02i$. (b) Wavelength $\lambda=354$ nm (plasmon resonance). Dielectric function of silver $\epsilon(354\text{ nm}) = -2.03+0.6i$. Adapted from Ref. [20].

The analytical calculation also permits to evaluate the short-distance dependence of $\rho^{\mathrm{R}}_{e,\mathbf{u}}$ and $\rho^{\mathrm{NR}}_{e,\mathbf{u}}$ in the limit $k_0 z \ll 1$, where z is the distance to the center of the nanoparticle. One obtains a scaling $\rho^{\mathrm{NR}}_{e,\mathbf{u}} \sim z^{-6}$, which is typical of non-radiative energy transfer in dipole–dipole interactions. The scaling of the radiative LDOS $\rho^{\mathrm{R}}_{e,\mathbf{u}}$ is more subtle since it involves terms with different power laws from z^{-6} to z^{-3}, with relative weights that depend on the proximity to the plasmon resonance [20]. Off resonance, the radiative LDOS scales as z^{-3}, while on resonance the scaling is dominated by the z^{-6} term. This behavior is the result of a balance between absorption in the particle and interferences between the two radiative paths shown in Fig. 1.

3.7. Semi-infinite geometry

Another useful geometry in which analytical expressions of the LDOS can be found is a flat interface separating a vacuum from a homogeneous material. Taking the Oz-axis normal to the interface, vacuum is assumed to correspond to the half-space $z>0$, and the material fills the semi-infinite medium $z<0$. The material is described by its frequency dependent dielectric function $\epsilon(\omega)$.

Calculating the LDOS amounts to calculating the imaginary part of the Green function. Taking the observation point in vacuum, the Green function $\mathbf{G}^E(\mathbf{r},\mathbf{r}',\omega)$ contains a direct contribution (free-space propagation from $\mathbf{r}'$ to $\mathbf{r}$) and a contribution due to reflection at the interface. An analytical expression can be given in Fourier space (plane wave expansion). It involves the Fresnel reflection factors for s and p polarized wave (see e.g. Ref. [48] for the derivation). From the expression of the Green function, the electric LDOS is deduced using Eq. (8). One obtains

$$\rho_e(z,\omega) = \rho_0(\omega)\times\left\{\int_0^{k_0}\frac{K\mathrm{d}K}{2k_0|q_1|}\left[\left(1-|r_s|^2\right)+\left(1-|r_p|^2\right)\right] + \int_{k_0}^{\infty}\frac{K\,\mathrm{d}K}{k_0|q_1|}\times\left[\mathrm{Im}(r_s)+\left(2\frac{K^2}{k_0^2}-1\right)\mathrm{Im}(r_p)\right] \times\exp\left[-2\mathrm{Im}(q_1)z\right]\right\}. \qquad (38)$$

In this expression, $r_s(K)$ and $r_p(K)$ are the Fresnel reflection coefficients for s and p polarization, respectively, $k_0=\omega/c$ and $K=|\mathbf{K}|$ is the modulus of the component $\mathbf{K}$ of the wavevector parallel to the interface. $q_{1,2}(K)$ are the components of the wavevector perpendicular to the interface on the vacuum side, and on the metal side, respectively. They satisfy $K^2+q_1^2=k_0^2$ and $K^2+q_2^2=\epsilon(\omega)k_0^2$, together with the determination $\mathrm{Re}(q_{1,2})>0$ and $\mathrm{Im}(q_{1,2})>0$. The Fresnel reflection factors are given by

$$r_s(K) = \frac{q_1(K)-q_2(K)}{q_1(K)+q_2(K)} \qquad (39)$$

$$r_p(K) = \frac{\epsilon(\omega)q_1(K) - q_2(K)}{\epsilon(\omega)q_1(K) + q_2(K)} \,. \tag{40}$$

It is important to note that these coefficients describe the electrodynamic response of the medium. In particular, surface plasmons appear as resonances (poles) of the reflection factor for p polarization. Indeed, the resonance condition $\epsilon(\omega)q_1(K) + q_2(K) = 0$ can be satisfied provided that $\mathrm{Re}[\epsilon(\omega)] < -1$, and leads to

$$K(\omega) = k_0 \sqrt{\frac{\epsilon(\omega)}{\epsilon(\omega)+1}} \tag{41}$$

which is the dispersion relation of surface plasmons at a metal–vacuum interface [1,49]. The measurement of the LDOS on flat interfaces and the role of surface-plasmon resonances are discussed in Section 6.

3.8. Extreme near field and non-local effects

At very short distance from a metal surface, the macroscopic description of the electrodynamic response of the metal breaks down. This regime is expected when the distance to the surface is on the order of the microscopic length scales driving the electron dynamics. In this case, the metal has to be described using a spatially non-local dielectric function. This issue has been described by Ford and Weber [43] in the context of molecular fluorescence. Microscopic interactions are expected to substantially enhance the non-radiative decay rate of emitters placed at short distance from a metal surface [44] or adsorbed on nanoparticles [50]. The full crossover between the far-field regime and the extreme near-field regime (below 1 nm) has been studied by Castanié et al. [42]. Here we summarize the approach and the main results.

In Ref. [42], an emitter with an electric transition dipole oriented along the normal to the surface (z direction) is considered. The change in the decay rate Γ_z is therefore due to the change in the projected electric LDOS $\rho_{e,z} = 2\omega/(\pi c^2)\,\mathrm{Im}[\mathbf{u}_z \cdot \mathbf{G}(\mathbf{r},\mathbf{r},\omega)\mathbf{u}_z]$, where $\mathbf{u}_z$ is the unit vector along the z-axis. The normalized decay rate $\Gamma_z/\Gamma_0 = \rho_{e,z}/\rho_0$ for an emitter placed in vacuum at a distance z from the surface is

$$\frac{\Gamma_z}{\Gamma_0} = 1 + \frac{3}{2k_0^2}\mathrm{Re}\int_0^\infty \frac{K^3}{q_1(K)}\, r_p(K)\exp\left[2iq_1(K)z\right]\,\mathrm{d}K \tag{42}$$

where $r_p(K)$ is the Fresnel reflection factor in p polarization, that is the only polarization involved for a dipole emitter oriented along the z direction. When the distance z becomes comparable to (or smaller than) the microscopic length scales describing the electron dynamics, the response of the metal differs from that of the bulk material, and the dielectric function becomes spatially non-local. For a medium with translational symmetry (i.e. for which the non-locality is not due to spatial confinement), the dielectric function becomes wavevector dependent. A widely used model for the non-local response of the electron gas in a metal is the Lindhardt–Mermin model, described in Ref. [43]. This model has also been used to describe nanoscale radiative heat transfer at short distance [51]. Using this model, the Fresnel reflection factor can be calculated. This requires to model the

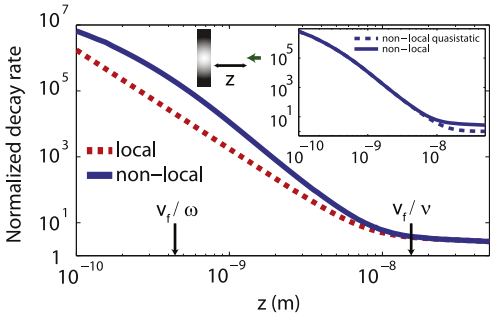

Fig. 3. Normalized decay rate in the extreme near-field regime for a flat surface of silver. Emission wavelength $\lambda = 700$ nm. Red dotted line: bulk dielectric function. Blue solid line: non-local model with parameters $\epsilon_b = 3.6$, $\omega_p = 1.42 \times 10^{16}\ \mathrm{s}^{-1}$, $\nu = 8.79 \times 10^{13}\ \mathrm{s}^{-1}$ [43]. The relevant length scales are indicated on the horizontal axis. Inset: comparison between the quasi-static approximation and the full calculation using the non-local model. From Ref. [42]. (For interpretation of the references to color in this figure caption, the reader is referred to the online version of this paper.)

electron gas at the interface. In the infinite barrier model, in which electrons at the surface undergo specular reflection, the Fresnel reflection factor can be written in terms of a surface impedance $Z(K)$ as [43]

$$r_p(K) = \frac{q_1(K)/(\omega\,\epsilon_1) - Z(K)}{q_1(K)/(\omega\,\epsilon_1) + Z(K)}. \tag{43}$$

The surface impedance depends on the transverse and longitudinal components of the non-local dielectric function of the metal:

$$Z(K) = \frac{2i}{\pi\omega}\int_0^\infty \left[\frac{q^2}{\epsilon_t(k,\omega) - (k/k_0)^2} + \frac{K^2}{\epsilon_l(k,\omega)}\right]\frac{\mathrm{d}q}{k^2} \tag{44}$$

with $k^2 = K^2 + q^2$. In the Lindhardt–Mermin model, the longitudinal and transverse dielectric functions read as

$$\epsilon_l(k,\omega) = \epsilon_b + \frac{3\omega_p^2}{\omega + i\nu}\frac{u^2 f_l(a,u)}{\omega + i\nu\, f_l(a,u)/f_l(a,0)} \tag{45}$$

$$\epsilon_t(k,\omega) = \epsilon_b - \frac{\omega_p^2}{\omega^2(\omega+i\nu)}\left\{\omega\left[f_t(a,u) - 3a^2 f_l(a,u)\right] + i\nu\left[f_t(a,0) - 3a^2 f_l(a,0)\right]\right\} \tag{46}$$

where ω_p is the plasma frequency and ν is the electron collision rate. The constant ϵ_b is an effective parameter accounting for interband transitions. In the large scales limit (small k), this expression simplifies and the classical Drude model is recovered. The arguments $a = k/(2k_F)$ and $u = (\omega + i\nu)/(kv_F)$, with k_F and v_F being the Fermi wavevector and velocity, contain the relevant microscopic length scales: the electron mean free path $\ell = v_F/\nu$, the distance $\delta = v_F/\omega$ travelled by an electron during one period of the electromagnetic field and the Fermi wavelength $\lambda_F = 2\pi/k_F$. The functions $f_l(a,u)$ and $f_t(a,u)$ read as $f_l(a,u) = 1/2 + [1-(a-u)^2]/(8a)\,\ln[(a-u+1)/(a-u-1)] + [1-(a+u)^2]/(8a)\ln[(a+u+1)/(a+u-1)]$ and $f_t(a,u) = 3(a^2+3u^2+1)/8 - 3[1-(a-u)^2]^2/(32a)\,\ln[(a-u+1)/(a-u-1)] - 3[1-(a+u)^2]^2/(32a)\ln[(a+u+1)/(a+u-1)]$. The limit $u \to 0$ has to be taken with a positive imaginary part so that $\ln[(a \pm u + 1)/(a \pm u - 1)] \sim \ln|(a+1)/(a-1)|$. The model

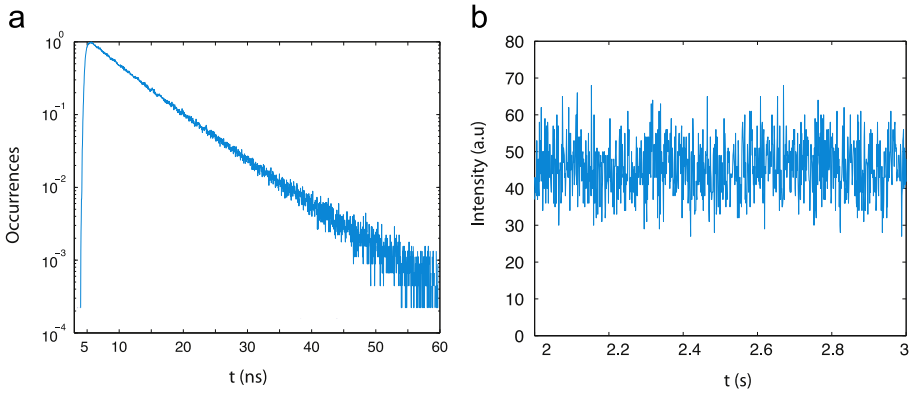

Fig. 4. (a) Fluorescence decay histogram measured for a polystyrene bead filled with dye molecules (diameter 25 nm). (b) Fluorescence intensity of the same bead as a function of time.

includes the mechanism of Landau damping (strong absorption of photons by accelerated free electrons in the regime $k\delta > 1$) that was described previously in Ref. [44].

The result of the model is presented in Fig. 3 that shows the dependence of the normalized decay rate on the distance z to a flat surface of silver, computed using the local model (red dotted line) and the non-local model (blue solid line) at a wavelength $\lambda = 700$ nm. At short distance, the decay rate increases in both cases due to an increase in the non-radiative LDOS (the radiative LDOS is negligible at short distance). In the non-local model, the slope is larger than that predicted by the macroscopic theory, due to non-radiative coupling to free electrons on scales smaller than the mean free path. The deviation starts for $z \lesssim \ell$ ($\ell = v_F/\nu = 16$ nm for silver), which sets the onset of the breakdown of the macroscopic approach. The macroscopic approach predicts $\Gamma_z \sim z^{-3}$. In the regime $z \sim \delta \ll \ell$ where Landau damping is expected to dominate, the microscopic approach predicts $\Gamma_z \sim z^{-4}$ [44], in good agreement with the slope given by the full calculation in Fig. 3. Finally, we note that for $z \lesssim 0.5$ nm, the onset of a saturation of the decay rate is observed. Indeed, for wavevectors $k > k_F$, the model predicts a reduced absorption due to a sharp cut-off in the imaginary part of the dielectric function [51]. Although this saturation is expected physically at some point, a precise computation in this region would require a more refined model, including an atomic description of the interface. The study of plasmonics at sub-nanometer scales, in which quantum confinement and tunneling effects become substantial, has been emerging as a critical and challenging issue, both from the theoretical and the experimental points of view [52,53].

4. Probing and mapping the LDOS in plasmonics

In the preceding section, we have shown that the LDOS is proportional to the spontaneous decay rate Γ of the excited state of a fluorescent emitter, a feature of the weak-coupling regime. The fluorescence lifetime $\tau = 1/\Gamma$ being a measurable quantity, it is straightforward to experimentally probe the LDOS at the position of the emitter and at the fluorescent emission wavelength in a given environment by measuring the fluorescence lifetime. For lifetimes going from a few hundreds of ns to a few tens of ps this can be done by exciting the fluorescent emitter with a pulsed laser and by collecting its fluorescence on an avalanche photodiode. The arrival time of the photons is then recorded with a time resolved single photon counting system which allows us to measure the delay between the detection of the fluorescence photon and the laser pulse that has excited the emitter. This time interval is reported on a histogram which exactly reproduces the probability for a photon to be emitted within a given delay from the excitation pulse. An example of such histogram, obtained for a polystyrene bead (diameter 25 nm) filled with dye molecules, is shown in Fig. 4(a). For an ideal two-level emitter the fluorescence decay is an exponential function and the lifetime of the excited state can be easily measured by fitting the delay histogram with a decreasing exponential. However, in the real world, the scenario is often different and the fluorescence decay can be fitted by a more complex function such as a bi-exponential or log-normal distribution. For the sake of completeness, Fig. 4(b) shows the fluorescence intensity as a function of time for the same fluorescent bead.

Two different experimental approaches for measuring the LDOS by all-optical means are reported in the literature. The first one consists in spreading the fluorescent emitters either inside or on the surface of the sample. The emitters are then addressed individually and the decay rate $\Gamma = 1/\tau \propto \rho_e(\mathbf{r}, \omega)$ is measured, where $\mathbf{r}$ is the position of the emitter and ω the emission frequency (we assume electric-dipole transitions in the emitter so that the electric LDOS ρ_e is actually measured). A review of recent works using this approach is presented in Section 4.1. This approach gives access only to statistical quantities, such as the LDOS distribution overall the sample. A crucial aspect when using this technique is the averaging over dipole orientation, because the LDOS strongly depends on it (see the discussion on projected and full LDOS in Section 3.1).

The second approach consists in grafting the fluorescent emitter at the extremity of an atomic force microscope (AFM) tip and by scanning it in the near field of the sample surface. This method allows us to access more exhaustive information since it allows us to simultaneously acquire the topography of the sample, the map of the fluorescence decay rate and of the

fluorescence intensity in a deterministic way with a resolution of the nanometer. However, this technique can only be used to retrieve informations regarding the influence of the surface of the sample on the emitter. In order to retrieve volume information it will be necessary to use the first technique. A review of experimental works using this method is given in Section 4.2.

The LDOS can also be probed by methods based on electron microscopy, such as electron energy loss spectroscopy (EELS) and cathodoluminescence (CL). The clear advantage of these techniques with respect to all-optical techniques can be found in the very good spatial resolution. However, the physical interpretation of the measured signals is often challenging and not as direct as for all-optical methods. A review on these techniques will be given in Section 4.3.

4.1. Far-field detection techniques (fluorescence microscopy)

Statistical measurements of the LDOS have been done in different kinds of systems, going from plasmonic samples to dielectric samples, either ordered or disordered. The statistical behavior of LDOS fluctuations have been studied for fluorescent emitters located inside or on the surface of three-dimensional random arrangements of dielectric particles [54–56]. Measurements on ordered dielectric structures such as photonic crystals [57] or opals have also been reported (see for example Ref. [58]). Interesting studies on disordered photonics crystal membranes have been reported. Disorder here is introduced by randomly changing the position of the holes of the photonic crystal with respect to the standard ordered arrangement. The Anderson localization regime has been reached in these systems and LDOS fluctuations have been monitored by measuring the decay rate of quantum dots epitaxially grown below the photonic crystal membrane [38,59].

Statistical fluctuations of the LDOS can also be studied on plasmonic samples. Here we focus on random metallic thin films, which have very interesting optical properties that will be described in detail in Section 8. LDOS fluctuations on random gold films have been studied by dispersing polystyrene fluorescent nanobeads [60,47] or colloidal quantum dots on the surface of the film [61,62]. Purcell factors on the order of 10 have been reported and the observed LDOS fluctuations have been related to the spatial extent of the surface plasmon modes [60].

4.2. Scanning fluorescent-probe techniques

As pointed out in the introduction to this section, a thorough characterization of the LDOS, with a resolution in the 1–100 nm range, can be realized by using fluorescent near-field scanning probes. Three approaches are reported in the literature: (i) A fluorescent nanoemitter is grafted on the AFM tip and is then scanned in the near field of a nanostructured sample. (ii) Fluorescent emitters are spread on a glass cover slip and the sample of interest is located on the AFM tip. (iii) The AFM tip is used to push the fluorescent emitter towards the sample or vice versa.

The first method is the most versatile in terms of the large variety of samples and fluorescent emitters that can be used. Experimental demonstrations have been reported by several groups by grafting NV centers in diamond nanocrystals [63–65], polystyrene fluorescent nanobeads [66,67] or terrylene molecules in microcrystals [68] to the AFM tip. Samples under study were simple plasmonic nanowires or nanostructured plasmonic samples such as nanoantennas, triangular metallic islands or nanoholes in metallic films. As an example, the experimental results reported by some of the authors in Ref. [67] will be described in detail in Section 4.4. An interesting original approach has been described in Ref. [69], where a single-crystalline diamond nanopillar AFM probe has been fabricated with an individual NV center artificially created within 10 nm of the pillar tip through ion implantation. Such a probe has been used to measure the magnetic field at the nanometer scale.

The second method can be used with a limited number of samples, such as metallic mirrors directly deposited on the AFM tip [70,71] or nanoantennas which can be etched on the extremity of the AFM tip [72,73]. This requires clean-room facilities and mastering of highly technological methods for nanofabrication.

The third method allows the deterministic positioning of fluorescent nanoparticles [74], but it is hardly usable for mapping the photonic properties of a nanostructured sample. This method has allowed the coupling of photonic crystal cavities with single NV centers in diamond nanocrystals [75,76] and the coupling of single NV centers in diamond nanocrystals with pairs of silver nanowires with different gaps [77].

4.3. Probing the photonic LDOS with electron microscopy

The response of a nanostructured medium to an external excitation can also be probed with electron microscopy techniques, such as electron energy loss spectroscopy (EELS) or cathodoluminescence (CL). The aim of this section is to briefly describe each technique, as well as the connection between the measured quantities and the photonic LDOS. The advantage of these techniques with respect to all-optical techniques resides in the very high resolution that can be achieved, which can go down to the nanometer scale because of the small wavelength of the electron beam. EELS and CL are scanning transmission electron microscopy techniques in which an electron beam is focused, by a set of magnetic lenses, on a small area of a sample. Electrons can then undergo either elastic or inelastic scattering. Elastically scattered electrons are collected and used to image the morphology of the sample, while inelastically scattered electrons can be studied with different spectroscopic techniques. For example, EELS is performed by measuring the energy lost by the electrons that are inelastically scattered at small angles after having been transmitted by the sample. CL is done by studying the electromagnetic radiation coming from the sample due to the

interaction with the electronic beam. Electrons transfer to the sample a given amount of energy which is then released in the form of visible photons allowing the sample to come back to equilibrium via a radiative decay channel. While EELS can be used for the study of sub-wavelength objects such as individual nanoparticles, CL is usually more appropriate for the study of large and/or thick nanostructures exhibiting a large radiation probability. For reviews of these two methods and their applications to LDOS measurement, see Refs. [78–81].

Quantitatively, EELS characterizes the probability for an electron to loose a given amount of energy, referred to as the EEL probability. It can be shown theoretically [80] that this probability is related to the LDOS, in the real space on the xy plane (the sample plane), and in the Fourier space along the z direction. The different behavior along the z-axis can be inferred from the fact that electrons are only affected by the electric field components which are parallel to its propagation direction (here the z direction, orthogonal to the sample plane). An example of the application of the EELS technique to the study of plasmonic systems such as random metallic films can be found in Ref. [82].

CL is based on the fact that the interaction of an electron with a medium can be represented by a transient dipole aligned along the trajectory of the electron and placed either at the position of the impact or along the electron path. For a given material, this dipole has a constant amplitude, but the radiated power depends on the optical properties of the surrounding medium. Therefore the signal measured by CL is related to the LDOS at the impact location. It can be shown [83] that the observed light emission is a measure of the radiative component of the LDOS projected on the direction of propagation of the electron, which coincides with the direction of the transient dipole. Therefore CL allows us to probe a pure vectorial component of the radiative LDOS. For these reasons, CL allows us to probe the LDOS only in polarizable media laying on weakly conducting substrates to allow charge dissipation. A recent work [84] has demonstrated the use of this technique to probe and image the Bloch modes in photonic crystals and in photonics crystal cavities. The presence of localized modes has been demonstrated and a thorough study of the LDOS in these systems has been performed [84].

4.4. Towards a full characterization of a plasmonic nanostructure

In a recent work, some of the authors have demonstrated that the fluorescent scanning near-field probe technique can be used to characterize the electromagnetic field at the surface of a plasmonic nanoantenna [67]. The experimental setup is sketched in Fig. 5.

A home-made atomic force microscope (AFM), presenting a fluorescent nanoemitter grafted at the apex of its tip, is coupled with a confocal microscope. The fluorescent emitter, which is a polystyrene bead (diameter 100 nm) filled with dye molecules (Invitrogen Red Fluosphere), is excited via an oil immersion microscope objective (NA = 1.3), by a super continuous pulsed laser (Fianium SC450) filtered at a wavelength of 560 nm. Fluorescence photons ($\lambda > 594$ nm) are then collected by the same objective and are detected either by an EM-CCD camera or by an avalanche photodiode coupled with a single photon time-resolved counting system, using PMD-series MPD avalanche photodiodes and an acquisition board PicoQuant HydraHarp400. This system allows the simultaneous acquisition of the topography of the sample, the map of the fluorescence intensity and that of the decay rate of the emitter, with a spatial resolution of a few tens of nanometers. The AFM is based on the use of a quartz tuning fork and works in shear force mode in order to keep the distance between the nanoemitter and the sample constant during the scan. This is particularly relevant for the LDOS map which is strongly dependent on the distance between the bead and the sample [47,67]. The AFM tip is a tapered optical fiber and the amplitude oscillation is of the order of 10 nm. Details on the method used to graft the fluorescent bead on the tip can be found in Ref. [67].

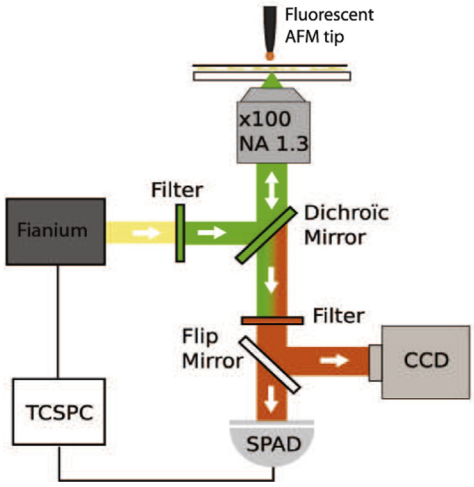

Fig. 5. Sketch of the experimental setup. An AFM system is combined with a confocal microscope and a time-resolved single photon counting system (TCSPC). Photons can be detected either on a CCD camera or on an avalanche photodiode (SPAD).

A first proof of the operation of the experimental setup has been realized on an optical nanoantenna formed by three gold nanodiscs, 30 nm thick, having a diameter of 150 nm and separated by 50 nm. Fig. 6 shows, from top to bottom, the topography of the sample, the map of the fluorescence intensity and the map of the decay rate. As one can notice, the measured topography presents three zones of a height of about 30 nm which are elongated in one direction rather than circularly shaped as one could expect. This is due to the fact that the fluorescent bead, which has a size comparable with the tip apex, is grafted on the side of the tip. Therefore, the antenna is scanned twice, first by the silica tip and then by the fluorescent bead. This results in a doubled topographic image of each disc. This artifact is not observed in the fluorescence intensity and in the decay rate maps. This is easily understood since only the fluorescent bead contributes to the optical signal. In order to guide the eye, the real position of each disc is drawn in dashed

line. The fluorescence intensity map shows a minimum when the bead is on the top of each gold disc, due to the presence of gold. The fluorescence decay rate map shows three regions

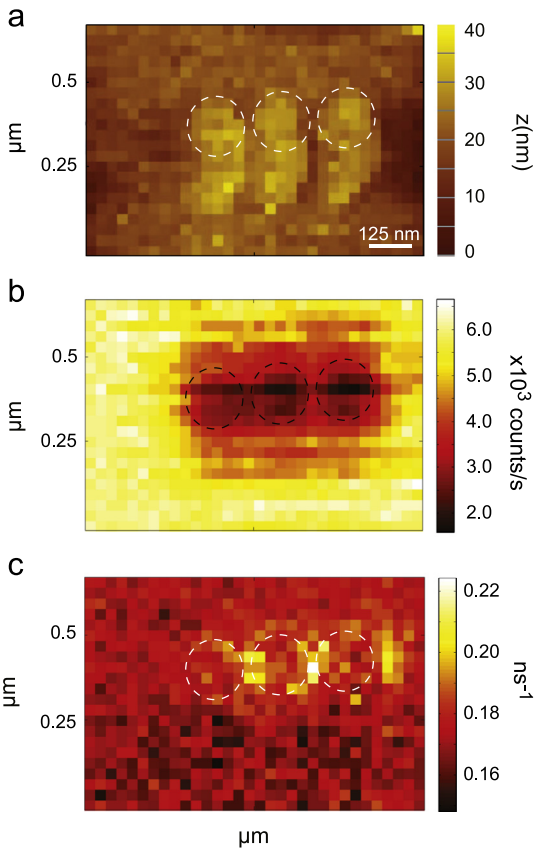

Fig. 6. Topography (a), fluorescence intensity (b) and fluorescence decay rate (c) maps obtained with a polystyrene fluorescent sphere grafted to the extremity of the AFM tip and scanned in the near field of a plasmonic nanoantenna. From Ref. [67].

where the decay rate is enhanced, two of those located in the gap regions, the third one located on the side of the antenna. We may note that the spatial extension of the decay rate (or LDOS) enhanced region is on the order of 50 nm, proving that the resolution of the active probe is of this order of magnitude.

In order to have a better insight in the experimental results we performed numerical calculations of fluorescence intensity and decay rate maps. Numerical simulations are done in the same geometry as in the experiment, by considering an ensemble of dye molecules randomly oriented and distributed inside a sphere of diameter equal to 100 nm. The nanoantenna is floating in vacuum and is discretized in cubes of 5 nm side. In order to calculate the electric field on the top of the nanoantenna, we solve the Lippman–Schwinger equation for both the excitation and emission fields. Once the electric field is known, the Green function in the presence of the nanoantenna $\mathbf{G}^E$ is deduced from $\mathbf{E}(\mathbf{r}) = \mu_0\omega^2\mathbf{G}^E(\mathbf{r}, \mathbf{r}_0, \omega)\mathbf{p}$ and the LDOS and the fluorescence intensity can be calculated. The numerical method is described more precisely in Section 8.2.2. The results of the numerical simulations are displayed in Fig. 7. Experimental and simulated LDOS and fluorescence intensity maps present an almost quantitative agreement. Both numerical simulations and experiments show the same general trends, i.e. a decrease of the fluorescence intensity in coincidence of the gold discs and an enhancement of the LDOS in the gaps. A contrast of about a factor 3 of the fluorescence intensity is observed on both the numerical and the experimental maps. The experimental LDOS map shows a contrast reduced with respect to the numerical map. This is due to the absence of the substrate in the numerical simulation and to the fact that the height of the fluorescent bead with respect to the sample is not exactly known. Numerical simulations have been performed for a distance between the bead and the sample of 20 nm. Moreover, the numerical map shows four regions

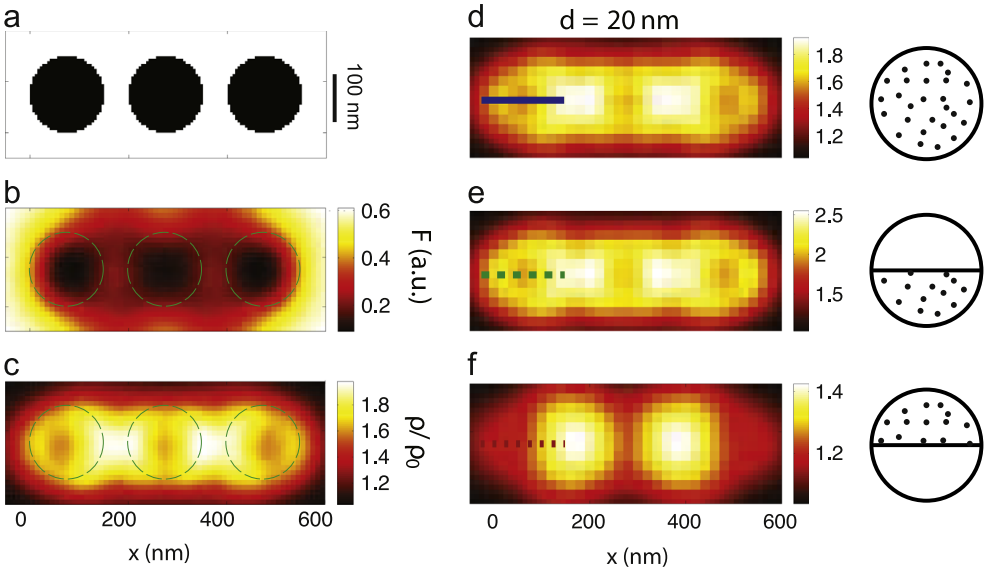

Fig. 7. Numerical simulations. (a) Top view of the topography of the simulated structure. (b), (c) Fluorescence intensity map and LDOS map normalized to its value in vacuum. (d)–(f) LDOS maps calculated for a bead either completely filled with dye molecules or filled only on the top or bottom hemisphere, as sketched on the right side of the figure. All the simulations have been done for a distance between the bottom of the sphere and the sample of 20 nm. Adapted from Ref. [67].

where the LDOS is enhanced, while the experimental data show only three of them. This can be explained either by a fabrication defect of the real antenna or by the asymmetry of the active probe. Since the bead is grafted on the side of the silica tip, the trajectory followed by the bead can be different when the probe climbs up or down the nanostructure, introducing an asymmetry in the images.

The size of the regions where the LDOS is enhanced is of the order of 50 nm. At a first thought it can be surprising to see that we can achieve such a small resolution with an active AFM probe composed of a 100 nm fluorescent bead. In order to clarify this point we calculated the LDOS map by using, as a fluorescent emitter, a 100 nm bead filled by dye molecules located either only in the bottom hemisphere or only in the top hemisphere and we compared the results with the simulation obtained with a sphere completely filled by dye molecules. The results are reported in Fig. 7(d)–(f). The vertical distance between the bead and the sample is fixed again at 20 nm. As one can see, the high spatial frequency details are present in the LDOS map obtained using only the bottom of the sphere and they are conserved in the map obtained using a completely filled sphere (with a smaller contrast). However, they are washed out in the maps obtained using the dyes located on the top of the bead, due to a spatial filtering effect which is common in near-field measurements. Therefore we can conclude that dye molecules located in the bottom part of the sphere are responsible for the resolution of these details and consequently, the effective resolution is not limited by the size of the bead, but in the present case is on the order of 50 nm.

5. Equilibrium radiation. Electric and magnetic LDOS

In Section 3, the concept of LDOS has been introduced in the context of spontaneous emission by a dipole emitter. The LDOS also enters the description of equilibrium (or blackbody) radiation, and therefore plays a key role in the description of thermal fluctuations and heat transfer. This issue has been discussed extensively in another review [49]. Here we will focus on two specific aspects of relevance for plasmonics. We will put forward the existence of both an electric and a magnetic contributions to the LDOS, as initially derived in Ref. [21]. Although light–matter interaction is often dominated by the coupling of the electromagnetic field to electric dipoles, the importance of magnetic interactions in nanophotonics and plasmonics has increased due to the development of metamaterials [85–87] or antennas coupling electric and magnetic responses [88–92], and to the possibility to use fluorophores with efficient magnetic dipole transitions [93–97]. We will also introduce the basic quantities allowing us to describe the measurement of thermal near fields using the thermal radiation scanning tunneling microscopy (TRSTM) technique [98]. This technique provides a direct measurement of the LDOS, and is particularly interesting in plasmonics. It is described in Section 6 in this review.

5.1. Blackbody spectrum

Blackbody radiation is the electromagnetic radiation at thermodynamic equilibrium with matter. In this situation, the field is described statistically, and considered to be generated by a stationary stochastic process. The description of observables, such as energy density or optical forces, requires the computation of field–field correlation functions [22]. Blackbody radiation is also the starting point for the study of radiation transfer in non-equilibrium situations [49,99]. Linear response theory provides a powerful method to compute field–field correlation functions, through the use of the fluctuation–dissipation theorem [100]. We shall briefly review the important steps in this approach.

The electromagnetic energy density at a point $\mathbf{r}$ located in vacuum, but in an arbitrary environment, is defined as

$$\langle U(\mathbf{r})\rangle = \frac{\epsilon_0}{2}\langle|\mathbf{E}(\mathbf{r},t)|^2\rangle + \frac{\mu_0}{2}\langle|\mathbf{H}(\mathbf{r},t)|^2\rangle \tag{47}$$

where the brackets stands for averaging over the fluctuations of the field. We consider an observation point in vacuum, although it can be located at an arbitrarily small distance from a material surface, in order to get an unambiguous definition of the field energy (for a point lying inside a material, the definition of the field energy at the macroscopic level is a complex issue, due to the coupling to material degrees of freedom). A spectral energy density $U(\mathbf{r},\omega)$ is introduced as

$$\langle U(\mathbf{r})\rangle = \int_0^\infty U(\mathbf{r},\omega)\frac{\mathrm{d}\omega}{2\pi}. \tag{48}$$

Its computation requires the knowledge of the cross spectral densities $W_{jk}^{E,H}(\mathbf{r},\mathbf{r}',\omega)$ of the electric and of the magnetic field, that are defined by

$$\langle E_j(\mathbf{r},t)E_k(\mathbf{r}',t+\tau)\rangle = \mathrm{Re}\int_0^\infty W_{jk}^{E}(\mathbf{r},\mathbf{r}',\omega)\exp(-i\omega\tau)\frac{\mathrm{d}\omega}{2\pi} \tag{49}$$

and

$$\langle H_j(\mathbf{r},t)H_k(\mathbf{r}',t+\tau)\rangle = \mathrm{Re}\int_0^\infty W_{jk}^{H}(\mathbf{r},\mathbf{r}',\omega)\exp(-i\omega\tau)\frac{\mathrm{d}\omega}{2\pi}. \tag{50}$$

In the quantum theory of radiation, the field–field correlation functions have to be understood as correlation functions of quantum operators, and ordering has to be handled with care. This point has been discussed precisely in Ref. [22], and summarized in Ref. [49]. Here normally ordered correlation functions are assumed, and the fluctuation–dissipation theorem leads to the following expressions of the cross spectral densities at equilibrium:

$$W_{\mathrm{jk}}^{E}(\mathbf{r},\mathbf{r}',\omega) = 4\mu_0\omega\,\mathrm{Im}\left[G_{\mathrm{jk}}^{E}(\mathbf{r},\mathbf{r}',\omega)\right]\Theta(\omega,T) \tag{51}$$

$$W_{\mathrm{jk}}^{H}(\mathbf{r},\mathbf{r}',\omega) = 4\epsilon_0\omega\,\mathrm{Im}\left[G_{\mathrm{jk}}^{H}(\mathbf{r},\mathbf{r}',\omega)\right]\Theta(\omega,T) \tag{52}$$

where $\Theta(\omega,T) = \hbar\omega/[\exp(\hbar\omega/k_BT)-1]$, T being the temperature and k_B the Boltzmann constant. In these equations, two different Green functions are used. The electric Green function $\mathbf{G}^E(\mathbf{r},\mathbf{r}',\omega)$ connects a point electric dipole source at position $\mathbf{r}'$ to the electric

field radiated at point $\mathbf{r}$. The magnetic Green function $\mathbf{G}^{H}(\mathbf{r},\mathbf{r}',\omega)$ connects a point magnetic dipole source at position $\mathbf{r}'$ to the magnetic field radiated at point $\mathbf{r}$. Note that cross Green functions $\mathbf{G}^{EH}(\mathbf{r},\mathbf{r}',\omega)$ and $\mathbf{G}^{HE}(\mathbf{r},\mathbf{r}',\omega)$ also exist, that couple a magnetic dipole to the electric field and an electric dipole to the magnetic field, respectively. They can be relevant for the description of nano-antennas or metamaterials generating coupled electric and magnetic responses [91,92], but they do not enter the description of the equilibrium energy density.

From Eqs. (47) to (52), one derives the following expression of the spectral equilibrium energy density

$$U(\mathbf{r},\omega)=\frac{\omega}{\pi c^2}\left\{\mathrm{Im}\left[\mathrm{Tr}\,\mathbf{G}^{E}(\mathbf{r},\mathbf{r},\omega)\right]+\mathrm{Im}\left[\mathrm{Tr}\,\mathbf{G}^{H}(\mathbf{r},\mathbf{r},\omega)\right]\right\}\frac{\hbar\omega}{\exp\left(\hbar\omega/k_BT\right)-1} \tag{53}$$

that explicitly contains an electric and a magnetic contribution. From a statistical physics point of view, one can also write the spectral energy density as the product of the local density of states, the averaged number of excitations (photons) per mode (Bose–Einstein statistics) and the energy of one photon, so that

$$U(\mathbf{r},\omega)=\rho(\mathbf{r},\omega)\,\frac{\hbar\omega}{\exp(\hbar\omega/k_BT)-1}. \tag{54}$$

This relation can be considered as an alternative definition of the LDOS [21]. By identification with Eq. (53), we obtain

$$\rho(\mathbf{r},\omega)=\frac{\omega}{\pi c^2}\,\mathrm{Im}\left\{\mathrm{Tr}\left[\mathbf{G}^{E}(\mathbf{r},\mathbf{r},\omega)+\mathbf{G}^{H}(\mathbf{r},\mathbf{r},\omega)\right]\right\} \tag{55}$$

which is the full LDOS entering the expression of the energy density spectrum of blackbody radiation. This approach naturally leads to the introduction of an electric and a magnetic LDOS.

5.2. Electric and magnetic LDOS

We can define the electric and magnetic contributions to the LDOS in the following way:

$$\rho_e(\mathbf{r},\omega)=\frac{2\omega}{\pi c^2}\,\mathrm{Im}\left[\mathrm{Tr}\,\mathbf{G}^{E}(\mathbf{r},\mathbf{r},\omega)\right] \tag{56}$$

$$\rho_m(\mathbf{r},\omega)=\frac{2\omega}{\pi c^2}\,\mathrm{Im}\left[\mathrm{Tr}\,\mathbf{G}^{H}(\mathbf{r},\mathbf{r},\omega)\right]. \tag{57}$$

With this definition, the full electromagnetic LDOS that enters the expression of the energy density spectrum of blackbody radiation is simply

$$\rho(\mathbf{r},\omega)=\tfrac{1}{2}\left[\rho_e(\mathbf{r},\omega)+\rho_m(\mathbf{r},\omega)\right]. \tag{58}$$

The definitions of the electric and magnetic LDOS used here differ by a factor of 2 from that introduced in Refs. [21,49]. This choice is made for consistency with the definition of electric and magnetic LDOS in the context of spontaneous emission by dipole emitters, in which a prefactor of 2 is used, as in Eq. (8) [3]. It is also important that in the far field asymptotic limit, the electric and magnetic Green functions coincide, so that the distinction between electric and magnetic LDOS becomes meaningless when near-field interactions can be ignored. With the definition used here, in the far-field limit one simply has $\rho(\mathbf{r},\omega)=\rho_e(\mathbf{r},\omega)=\rho_m(\mathbf{r},\omega)$.

5.3. Electric and magnetic LDOS in semi-infinite geometry

The expression of the electric LDOS above a flat interface separating a vacuum from a semi-infinite medium has been introduced in Section 3.7. The magnetic Green function and the magnetic LDOS can be calculated along the same line [49]. It turns out that the expression of the magnetic Green function is obtained from that of the electric Green function by simply interchanging the Fresnel reflection factors $r_s(K)$ and $r_p(K)$. The same holds for the LDOS, so that the magnetic LDOS reads as

$$\rho_m(z,\omega)=\rho_0(\omega)\times\left\{\int_0^{k_0}\frac{K\,\mathrm{d}K}{2k_0|q_1|}\left[\left(1-|r_s|^2\right)+\left(1-|r_p|^2\right)\right]+\int_{k_0}^{\infty}\frac{K\,\mathrm{d}K}{k_0|q_1|}\times\left[\left(2\frac{K^2}{k_0^2}-1\right)\mathrm{Im}(r_s)+\mathrm{Im}\left(r_p\right)\right]\exp\left[-2\mathrm{Im}\left(q_1\right)z\right]\right\}. \tag{59}$$

The full LDOS $\rho(\mathbf{r},\omega)=[\rho_e(\mathbf{r},\omega)+\rho_m(\mathbf{r},\omega)]/2$ is readily obtained from Eqs. (38) and (59):

$$\rho(z,\omega)=\frac{\rho_0(\omega)}{2}\times\left\{\int_0^{k_0}\frac{K\,\mathrm{d}K}{k_0|q_1|}\left[\left(1-|r_s|^2\right)+\left(1-|r_p|^2\right)\right]+\int_{k_0}^{\infty}\frac{2K^3\,\mathrm{d}K}{k_0^3|q_1|}\times\left[\mathrm{Im}(r_s)+\mathrm{Im}\left(r_p\right)\right]\exp\left[-2\mathrm{Im}\left(q_1\right)z\right]\right\}. \tag{60}$$

5.4. Measurement of electric and magnetic LDOS in the near field

The influence of both the electric and the magnetic contributions to the LDOS can be probed using fluorophores exhibiting both electric-dipole (ED) and magnetic-dipole (MD) transitions in the same frequency range, and with oscillator strengths on the same order of magnitude. Rare earth doped crystals fill these requirements, and can be used to probe the electric and magnetic near field LDOS, as initially demonstrated by Karaveli and Zia [93,94]. More recently, Aigouy and co-workers have used a Eu^{3+} nanocrystal grafted at the apex of the tip of a near-field scanning optical microscope (NSOM), providing the first example of a fluorescent NSOM using simultaneously ED and MD emission [97]. Fluorescent scanning-probe techniques are discussed in Section 4.2 in this review. Here we describe specifically the measurement of ED and MD emission.

The setup developed by Aigouy et al. is represented in Fig. 8(a). Illumination is made at oblique incidence ($\lambda=532$ nm) and luminescence is collected with a high numerical aperture objective (NA = 0.8), situated above the tip and the sample. The fluorescent nanocrystal (typically 100–200 nm in size) is scanned in the near field of a sample, while recording spectra of the fluorescence intensity. A fluorescence spectrum recorded when the tip is located in front of a flat gold mirror is

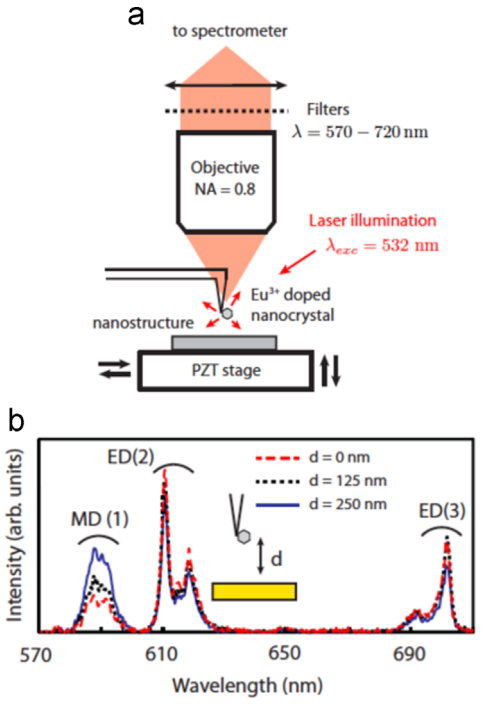

Fig. 8. (a) Experimental setup. The Eu^{3+}-doped nanocrystal is attached to the tungsten NSOM tip and can be scanned across the sample. Crystal size $\simeq 200$ nm. (b) Luminescence spectrum of the Eu^{3+}-doped nanocrystal at several distances from a gold mirror. The spectral peaks corresponding to one magnetic-dipole transition (1) and two electric-dipole transitions (2 and 3) are indicated. Adapted from Ref. [97].

shown in Fig. 8(b). In the spectral range of interest, three luminescence peaks are identified [93]. The peak located between 580 nm and 600 nm corresponds to one MD transition ($^5D_0 \rightarrow {}^7F_1$ labelled as transition 1), and the peaks in the spectral ranges 600–630 nm and 685–705 nm correspond to two ED transitions ($^5D_0 \rightarrow {}^7F_2$ and $^5D_0 \rightarrow {}^7F_4$ labelled as transitions 2 and 3).

As a measure of the relative contribution of each transition, a branching ratio is defined as

$$\beta_j(\mathbf{r}) = \frac{I_j^{\mathrm{fluo}}(\mathbf{r})}{I_{\mathrm{total}}^{\mathrm{fluo}}(\mathbf{r})} \tag{61}$$

where $\mathbf{r}$ is the position of the nanocrystal (emitter). In this expression, $I_j^{\mathrm{fluo}}(\mathbf{r})$ is the fluorescence intensity emitted in the spectral peak corresponding to transition number j, and $I_{\mathrm{total}}^{\mathrm{fluo}}(\mathbf{r})$ is the fluorescence intensity detected over the full spectral detection range. The fluorescence intensity of a given transition is $I_j^{\mathrm{fluo}}(\mathbf{r}) = N(^5D_0)\Gamma_j^{\mathrm{R}}$, where Γ_j^{R} is the radiative spontaneous decay rate and $N(^5D_0)$ is the population of the excited state that can be calculated using a four-level model [93,97]. Considering that the fluorescence intensity is chiefly given by the three transitions, the branching ratio can be rewritten as

$$\beta_j(\mathbf{r}) = \frac{I_j^{\mathrm{fluo}}(\mathbf{r})}{\sum_j I_j^{\mathrm{fluo}}(\mathbf{r})} = \frac{\Gamma_j^{\mathrm{R}}}{\sum_j \Gamma_j^{\mathrm{R}}} \tag{62}$$

which is independent of the excitation intensity. This result is a key point, since it permits to extract information on the radiative electric and magnetic LDOS from the measurement of the fluorescence intensity (and not of the fluorescence lifetime) [94]. For each transition, one can write $\Gamma_j^{\mathrm{R}} \propto f_j \rho_{e,m}(\mathbf{r}, \omega_j)$, where f_j is the oscillator strength of the transition and $\rho_{e,m}^{\mathrm{R}}(\mathbf{r}, \omega_j)$ is the electric (for ED transition) or magnetic (for MD transition) radiative LDOS at the emission frequency of the transition (taken as the maximum frequency of each peak), $3 \times 4.8\ \mu\mathrm{m}^2$ and $4 \times 1\ \mu\mathrm{m}^2$. Experimental near-field maps of the branching ratios $\beta_1(\mathbf{r})$ (MD transition) and $\beta_2(\mathbf{r})$ (ED transition) are shown in Fig. 9(a), on a sample made of a gold stripe on a glass substrate. Maps recorded by scanning the fluorescent nanocrystal in a horizontal plane parallel to the sample, and in a vertical plane on top of the sample, are displayed. The signal due to MD and ED transitions exhibits different variations, with opposite contrast at short distance.

Following a method initially proposed by Taminiau et al. [95], it is possible to deduce the relative electric and magnetic radiative LDOS from the branching ratios (for the detailed theory and processing of the data see Ref. [97]). The relative electric radiative LDOS is defined by

$$\tilde{\rho}_e^{\mathrm{R}}(\mathbf{r}) = \frac{\rho_e^{\mathrm{R}}(\mathbf{r}, \omega_2)}{\rho_e^{\mathrm{R}}(\mathbf{r}, \omega_2) + \rho_m^{\mathrm{R}}(\mathbf{r}, \omega_1)} \tag{63}$$

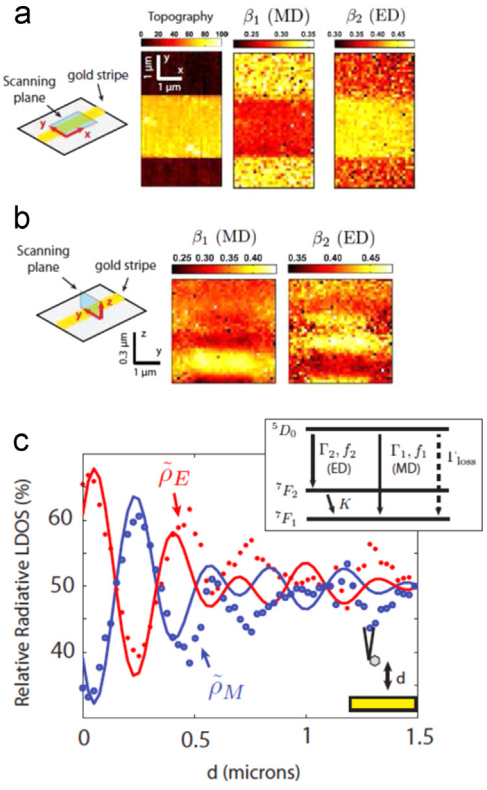

Fig. 9. (a) Topography of a gold stripe on a glass substrate and images of branching ratios of transitions MD1 and ED2 in the x–y plane. Image size $3 \times 4.8\ \mu\mathrm{m}^2$. (b) Branching ratios of transitions MD1 and ED2 in the y–z plane. Image size $4 \times 1\ \mu\mathrm{m}^2$. (c) Relative radiative electric $\tilde{\rho}_e$ and magnetic $\tilde{\rho}_m$ LDOS versus the distance to a gold mirror. Analytical calculation (full lines) and measurements (red dots and blue circles). Adapted from Ref. [97]. (For interpretation of the references to color in this figure caption, the reader is referred to the web version of this paper.)

where ω_1 and ω_2 are the peak frequency of two nearby MD and ED transitions. The relative magnetic radiative LDOS is defined by $\tilde{\rho}_m^{\mathrm{R}}(\mathbf{r}) = 1 - \tilde{\rho}_e^{\mathrm{R}}(\mathbf{r})$. The distance dependence of the relative radiative LDOS measured in front of a gold surface is shown in Fig. 9(b). The solid lines are calculations obtained using the expressions of the electric and magnetic LDOS in front of a flat surface, Eqs. (38) and (59). The agreement between theory and experiment is very good, especially at short distances from the mirror. This result demonstrates the relevance of this fluorescent NSOM technique to measure the relative contribution of the electric and magnetic radiative LDOS in the near field of nanostructured materials.

6. Thermal radiation scanning tunneling microscopy

We have shown that the photonic LDOS enters the description of equilibrium thermal radiation (also known as blackbody radiation). The purpose of the present section is to describe near-field LDOS measurements based on the detection of infrared thermal radiation in the near field.

Thermal emission finds its origin in fluctuating thermal currents, and gives the possibility to excite both propagating and evanescent modes in a wide range of frequencies. We have shown in Section 5.1 that the spectrum of the energy density of thermal radiation $U(\mathbf{r},\omega)$ is governed by the LDOS. Indeed, for a system at equilibrium at temperature T, $U(\mathbf{r},\omega)$ is the product of the LDOS $\rho(\mathbf{r},\omega)$ and the mean energy of a quantum oscillator $\Theta(\omega,T) = \hbar\omega/[\exp(\hbar\omega/k_BT) - 1]$. In the particular case of an infinite plane interface separating vacuum from a material with dielectric function $\epsilon(\omega) = \epsilon'(\omega) + i\epsilon''(\omega)$, the evolution of the thermal emission spectrum with the distance z to the surface is driven by the LDOS $\rho(z,\omega)$ given in Eq. (60). The behavior of $U(z,\omega)$ in the presence of an interface supporting surface polaritons (surface plasmons on metals or surface phonons on polar materials) has been studied theoretically in Refs. [49,101].

In the near field, a simplified expression of the LDOS can be derived using the quasi-static approximation, valid in the regime $z \ll \lambda$, where $\lambda = 2\pi c/\omega$ is the observation wavelength. The leading term at short distance reads as [21,49,101]

$$\rho(z,\omega) = \frac{\epsilon''(\omega)}{|1+\epsilon(\omega)|^2}\frac{1}{16\pi^2\omega z^3} \tag{64}$$

where the $1/z^3$ dependence is a feature of the quasi-static regime. Note that the leading term in the regime considered here ($z \ll \lambda$ and mid IR frequencies) is due to the electric component of the LDOS $\rho_e(z,\omega)$. This expression shows that at the frequency $\omega_{\max}$ such that $\epsilon'(\omega_{\max}) = -1$, the LDOS exhibits a resonance producing a peak in its spectrum that is also expected in the thermal energy density $U(z,\omega)$. The resonance is sharp provided that the imaginary part of the dielectric function $\epsilon''(\omega_{\max})$ is not too large. The frequency $\omega_{\max}$ corresponds to the surface (plasmon or phonon) polariton resonance frequency. At this frequency, a large number of surface modes with large in plane wave vector components $\mathbf{K}$ exist within a narrow range of frequencies [49]. These surface modes are at the origin of the peak in the LDOS. Since these surface modes are such that $K \gg k_0$, with K being the component of the wavevector along the interface, the wavevector component perpendicular to the interface on the vacuum side is $q_1(K) = \sqrt{k_0^2 - K^2} \simeq iK$, showing that the surface modes are highly confined near the interface.

This has important consequences regarding the spectral properties of thermal radiation as a function of the distance from the surface of materials. In the far field, the emitted spectrum is the product of the free-space blackbody spectrum $U_{BB}(\omega)$ (Planck's function) and the emissivity (a number smaller than unity). The blackbody envelop of far-field thermal emission has a broadband spectrum given by Planck's curve, which according to Wien's displacement law has a maximum at a wavelength $\lambda_{\max} = K_W/T$, with T being the material's temperature, and Wien's constant $K_W = 2.898 \times 10^{-3}$ mK. The near-field regime coincides with distances $z \ll \lambda$. In this regime, according to Eq. (64), the spectrum of $U(z,\omega)$ is expected to increase by orders of magnitude beyond the universal Planck's envelop of the far-field thermal emission, and to become quasi-monochromatic for materials supporting surface polaritons. The energy emitted by the surface of such materials is thus much larger close to the surface than in the far field, and is partially temporally coherent due to the contribution of the thermally excited surface modes, in contrast with the temporal incoherence of the far-field black-body emission [101].

Similarly, it was also predicted that the partial spatial coherence of surface polaritons should be preserved in the thermal near field, leading to coherence lengths on the order of the surface polariton propagation length $L_{\mathrm{spp}}(\omega)$ that can be much larger than the vacuum wavelength λ, while no spatial coherence beyond $\lambda/2$ is expected in far-field thermal radiation [102]. These exciting properties, which were initially theoretical predictions [102,101], have all been verified since then in experiments aimed either at studying the spatial coherence of the thermal emission contribution from thermally excited surface waves which were diffracted in the far-field [103–105] or at directly probing the LDOS in the near-field at the surface of materials [98,106–111]. While at visible frequencies, the latter can be achieved by measuring the decay rate of a fluorescent nano-object as discussed in Section 4.4, we show below that in the infrared spectral range, the use of a sub-wavelength probe which scatters the near-field thermal emission is a convenient way to access both the spatial distribution and the spectrum of the LDOS at the surface of materials [98,106–111].

6.1. Probing the LDOS through the near-field thermal emission

The thermal radiation scanning tunneling microscope (TRSTM) is the first instrument which has been capable to directly probe the LDOS through measurements of the infrared near-field thermal emission at the surface of a sample [98]. Its principle is sketched in Fig. 10. It relies on the strong analogy which has been demonstrated on theoretical grounds between the scanning tunneling microscope (STM) and the near-field scanning optical microscope (NSOM). If weak coupling is assumed between the tip and the sample, both instruments can

be treated using the same unified formalism to relate the detected signal (the electronic current for the STM, and the scattered intensity or photonic current for the NSOM) to the electronic LDOS for the STM or to the LDOS for the NSOM [112]. Charge currents due to thermal fluctuations excite every possible electromagnetic mode in a body at an equilibrium temperature T according to photon statistics. This is responsible for the radiation of a thermal emission with a local density of electromagnetic energy $U(\mathbf{r},\omega)$ from its surface. A point-like isotropic dipole placed in the near-field near the body's surface can then in principle be used to scatter the near-field thermal emission at the dipole's position $\mathbf{r}_d$ to the far-field. Using a detector sensitive to the energy flux at frequency ω would in that case produce a signal proportional to $U(\mathbf{r}_d,\omega)$, and hence to the LDOS. Measurements of this signal while scanning the point-like dipole at the body's surface are expected to produce a map of the LDOS in the near-field. Note that this description is simplified because it neglects polarization issues at the detection, the interaction between the scattering dipole and the sample surface, specular reflections, and the contribution to the signal from the thermal emission of the scattering dipole itself. More detailed descriptions can be found in Refs. [21,49,113].

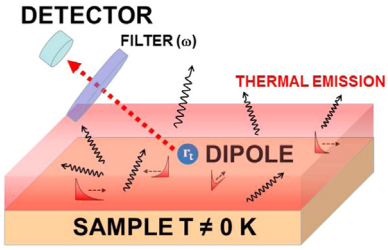

Fig. 10. Sketch illustrating the principle of the TRSTM. The electromagnetic modes are thermally excited at the surface of a body, and scattered by a point dipole placed in the near-field towards a detector located in the far-field. The signal at the detector is ideally proportional to $U(\mathbf{r}_d,\omega,T)$, and hence to the LDOS. In practice, this is only an approximation since the tip is not a passive point detector.

According to Wien's law, Planck's curve has a maximum at a wavelength λ_{max} that is typically in the mid-infrared range for a body near room-temperature ($\lambda_{max} \approx 10\,\mu m$ at $T = 300\,K$). Given this length scale, probing the LDOS through the near-field thermal emission at the surface of a sample, near room temperature and with subwavelength spatial resolution, requires the use of a scanning scattering probe with nanosized dimensions, which can be brought at nanometer distance from the sample surface. This is achieved in the TRSTM. The instrument is essentially a scattering-type NSOM operating in the mid-infrared without any external source. It uses as a source of signal the sole near-field thermal emission radiated by the surface of the sample, which is placed on a hot sample holder [98,108,113,110]. It can therefore be considered as the near-field equivalent of a night vision camera with superresolved imaging capabilities [98]. The invention of the TRSTM led to the development of other probes based on the same principle [106,107]. In particular, it was shown that instead of heating the entire sample to produce an isothermal surface, a heated tip could also be used both to locally heat the sample near the tip, and to scatter the near-field thermal emission excited in this way [107].

A schematic view of the TRSTM is given in Fig. 11, in a configuration intended to image the LDOS in the near field of a

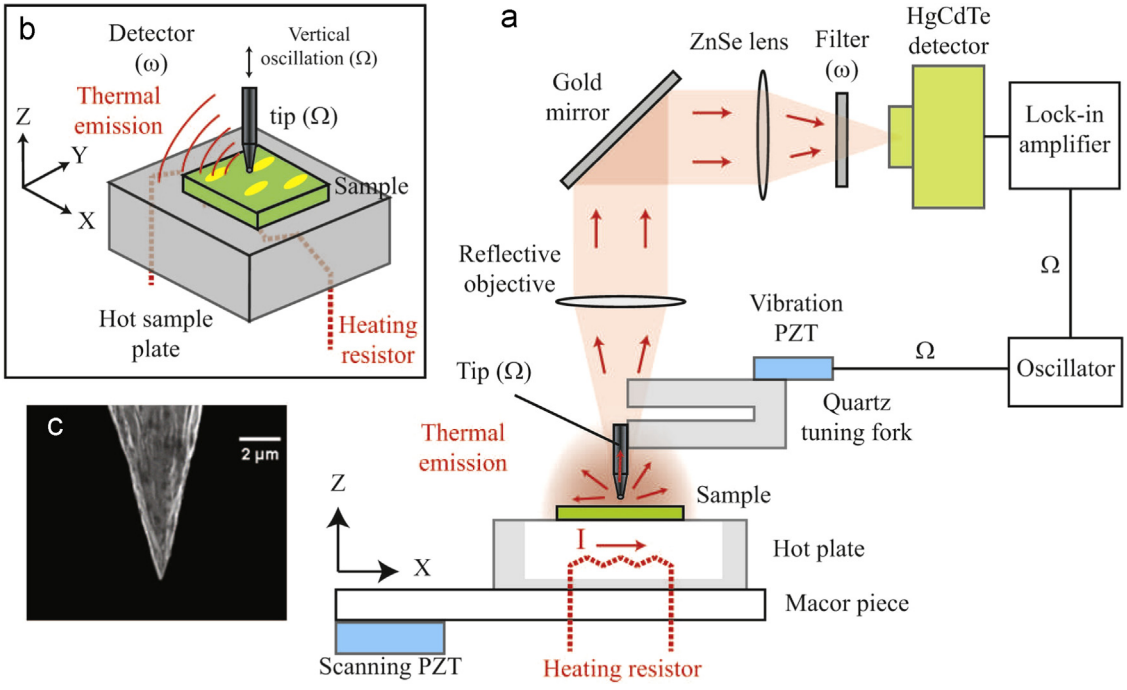

Fig. 11. (a) Experimental set-up of the thermal radiation scanning tunneling microscope (TRSTM) used for mapping the LDOS by measuring the mid-infrared near-field thermal emission scattered by an AFM tip. Inset (b) simplified view of the TRSTM illustrating its basic principle. Inset (c) SEM image of the tungsten (W) AFM tip used to scatter the near-field thermal emission at the sample surface towards the HgCdTe detector which is located in the far field.

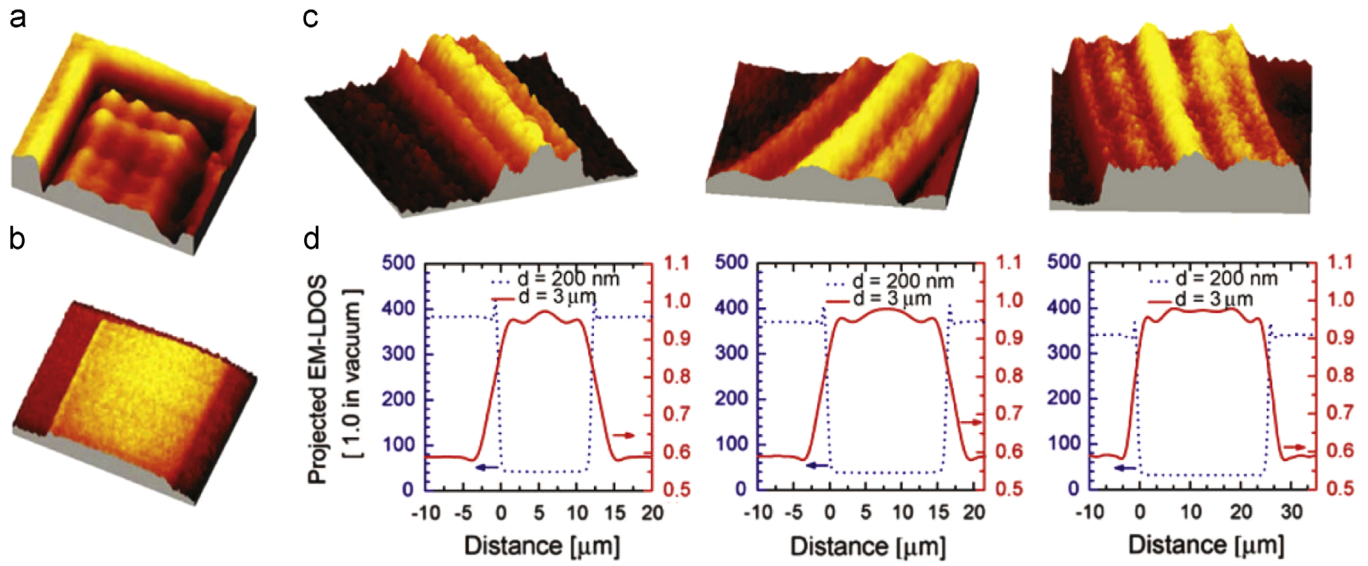

Fig. 12. (a) TRSTM map of the near-field thermal emission taken at Ω at the rectangular extremity of a gold (Au) stripe (width = 30 μm) on a silicon carbide (SiC) substrate using a bandpass filter at $\lambda^* = 10.9$ μm (width 1 μm) in front of the HgCdTe detector. The figure shows the typical structure of the LDOS in a cavity, with two perpendicular sets of fringes which are parallel to the edges of the gold pattern. The gold rectangle constitutes a cavity of thermally excited surface plasmons. (b) Image of the topography (AFM) acquired at the same time as (a) showing the rectangular gold pattern. (c) TRSTM image taken at Ω with the same bandpass filter of gold stripes of width 12 μm, 16 μm, and 25 μm on SiC, showing parallel fringes due to the cavity modes of the structure. (d) Profiles of the LDOS projected normal to the sample surface calculated for the structures investigated in (c) at two different heights: 3 μm and 200 nm. The same structure of fringes as in the experimental TRSTM images (c) is found in the projected LDOS calculated at 3 μm. This shows that when demodulating the TRSTM signal at Ω a field which extends over several micrometers above the sample is probed. This contribution comes predominantly from the surface plasmon polaritons on gold which are weakly confined in the infrared. However, the theoretical curves computed at a height of 200 nm reveal an enhanced LDOS on SiC with respect to gold, which is associated to highly confined surface phonon polariton modes on SiC. In all the experiments shown in this figure, the sample is at an isothermal temperature $T = 440$ K, but TRSTM measurements down to room temperature have also been performed. Adapted from Ref. [98]. (For interpretation of the references to color in this figure caption, the reader is referred to the web version of this paper.)

sample. It is based on an atomic force microscope (AFM) with a hot sample holder, operating in intermittent contact mode under a reflecting microscope objective combined with a single channel mid-infrared mercury–cadmium–telluride (HgCdTe) detector. The AFM uses an electrochemically etched tungsten (W) tip mounted on a quartz tuning fork. The latter is excited by means of a vibrating piezoelectric ceramic, in such a way that the tip oscillate perpendicularly to the sample surface. The tip hits periodically the sample surface at a frequency Ω, while its oscillation amplitude is stabilized around a preset value of ≈ 100 nm by an electronic feedback which dynamically controls the average height of the tip. Measurements of the feedback voltage while scanning the sample under the tip provide the topographic AFM image of the scanned area. The sample holder consists of a planar resistor mounted on a ceramic plate. It allows us to raise the sample temperature up to approximately 470 K. The extremity of the tip has a conical geometry and is terminated by a rounded apex whose radius of curvature is in the range of tens to hundreds of nanometers. When it is placed near the sample surface, it acts as a subwavelength scattering object and radiates in the far-field a signal linearly related to the infrared near-field thermal emission. This signal is collected by the reflecting objective, and directed towards the HgCdTe detector whose wavelengths range (detectivity larger than half its maximum value) extends between 7 μm and 12 μm. The selection of the energy of the scattered photons which contribute to the detected signal is performed by means of a narrowband filter placed before the detector, which performs band-pass filtering on the wavelength λ of the incoming radiation. The infrared thermal radiation from parts of the set-up other than the tip also contributes as a far-field continuous background on the detector signal. As the tip oscillates at the sample surface, it produces a small oscillatory component on the detector signal due to the scattered near-field thermal emission. The latter is demodulated at the frequency Ω and 2Ω using a lock-in amplifier, which allows one to efficiently suppress the far-field background contribution.

The TRSTM has been used to image the near-field thermal emission on 80 nm thick gold (Au) microstructures patterned on a silicon carbide (SiC) substrate [98]. With the set-up, two images are simultaneously recorded during each scan of the sample under the tip. The first one is the AFM topography obtained by measuring the feedback voltage which controls the average tip height as a function of its position. The second one is the corresponding image of near-field thermal emission scattered by the tip, measured at the demodulation frequency Ω or 2Ω at the output of the lock-in amplifier connected to the HgCdTe infrared detector. Fig. 12(a) and (b) presents the result of a recording obtained on the rectangular extremity of a gold stripe when the sample is at $T = 440$ K, with a filter centered at $\lambda^* = 10.9$ μm placed in front of the detector. The resolution in

both images is determined by the size of the tip apex. It is thus approximately two orders of magnitude beyond the diffraction limit as far as the mid-infrared near-field thermal emission image is concerned, which is a result expected for a near-field microscopy probe. Remarkably, the effect of the narrowband filter which selects the wavelengths of the detected photons is the appearance of two perpendicular sets of fringes on the gold rectangular structure in the near-field thermal emission image. The pattern is ascribed to surface plasmon polaritons on gold.

The surface plasmon polariton propagation length at the interface between a metal with dielectric function $\epsilon(\omega)=\epsilon'(\omega)+i\epsilon''(\omega)$ and a dielectric medium with dielectric function ϵ_m is given by

$$L_{\mathrm{spp}}=\frac{c}{\omega}\left(\frac{\epsilon'+\epsilon_m}{\epsilon'\epsilon_m}\right)^{3/2}\frac{\epsilon'^2}{\epsilon''} \tag{65}$$

where c is the speed of light. The dielectric function of an evaporated gold film at mid-infrared wavelength ($\lambda\approx 10\ \mu\mathrm{m}$) which has been precisely measured by spectroscopic ellipsometry [114] is typically $\epsilon_{\mathrm{Au}}=-4100+i1350$. Based on Eq. (65), L_{spp} is in the range of millimeters in the mid-infrared ($L_{\mathrm{spp}}=19$ mm at $\lambda=10\ \mu\mathrm{m}$), which has been verified experimentally [115]. Due to this large value of L_{spp}, the extremity of the gold stripe constitutes a cavity for the thermally excited surface plasmons. As the experiment probes the spatial variation of $U(\mathbf{r},\omega)$, Fig. 12(b) shows the typical structure of the LDOS associated to the surface plasmons at the central frequency $\omega^*=2\pi c/\lambda^*$ which are confined in the cavity. Note that it was experimentally verified with the same sample that the pattern of the near-field thermal emission image shown in Fig. 12(b) can in no instance be obtained using an external laser illumination of the tip as it is done in a scattering-type NSOM. This is because the laser produces an anisotropic excitation of the modes, regardless of the illumination configuration.

To further confirm that the TRSTM produces images of the LDOS, a comparison of experimental images of the near-field thermal emission recorded at Ω on Au stripes of different widths on SiC with theoretical calculations of the LDOS on the same structures is presented in Fig. 12(c) and (d). The quantity calculated theoretically and represented in Fig. 12(d) is the electric component of the projected LDOS $\rho_{e,\mathbf{u}}(\mathbf{r},\omega)$, where $\mathbf{u}$ is the direction perpendicular to the sample surface that coincides with the tip axis (in the regime considered here the LDOS is dominated by the electric contribution [21]). Theoretical curves of $\rho_{e,\mathbf{u}}(\mathbf{r},\omega)$ across the Au stripe are represented for two heights above the surface, 200 nm and 3 μm. A good qualitative agreement is found between the experimental images and the calculated curves of the projected LDOS 3 μm above the surface. While the number of fringes observed experimentally is in good agreement with the theory, the agreement regarding the contrast is only qualitative. The difference owes to the fact that the calculation neglects several aspects: (a) by considering only one projection of the LDOS, the tip is implicitly assumed to be a vertical electric dipole, while in reality it has both an electric and a magnetic response, which should be described by polarizability tensors [116,113,117]. (b) The tip is only assumed to be a point-like scatterer which passively "reads" the local electromagnetic field due to the near-field thermal emission. In reality, the detection process is complexified by the multiple scattering of the EM-field between the tip and the surface [113]. (c) The tip is assumed to be a simple point dipole, while in reality its elongated conical geometry is such that it rather corresponds to a distribution of scatterers along the direction perpendicular to the sample surface.

The qualitative agreement found between the experimental images and the profiles of the projected LDOS calculated 3 μm above the sample surface indicates that these distributed scatterers globally have the same effect as a point-like dipole that would scatter the local electromagnetic field at that height without modifying it. This result clearly points to an averaging process of the electromagnetic field scattered by the tip along the normal axis of the sample. Moreover, the surface plasmon polaritons on Au decay in air over several tens of μm at mid infrared wavelengths [4]. Considering this averaging process, it is thus not surprising that the signal demodulated at Ω coincides with the LDOS calculated a few μm above the Au surface.

6.2. Blackbody spectrum in the near field

While surface plasmon polaritons are excited on gold (Au) in Fig. 12, the interface between air and the SiC substrate supports surface phonon polaritons. Such surface waves are generally expected to occur at the interface between vacuum and polar materials. They correspond to lattice vibrations coupled to the electromagnetic field, which propagate parallel to the interface. Hence, their dispersion relation is expected to exhibit the asymptotic behavior which characterizes surface polaritons (when $\epsilon'=-1$) in the mid-infrared region of the electromagnetic spectrum, against the visible region for surface plasmon polaritons in metals. We show in this section that the TRSTM allows one to measure the near-field spectrum of the thermally excited surface waves, which is associated to the LDOS [107,108]. This issue is addressed by discussing in detail the case of surface phonon polaritons at the surface of SiC.

Infrared frequencies are generally expressed in wavenumbers $\sigma=1/\lambda$ using reciprocal centimeters (cm^{-1}) as units. The wavenumber dependence of the SiC dielectric function is well described by an oscillator model in the mid-infrared: $\epsilon_{\mathrm{SiC}}(\sigma)=\epsilon_\infty[1+(\sigma_L^2-\sigma_T^2)/(\sigma_T^2-\sigma^2-i\Gamma\sigma)]$, where $\epsilon_\infty=6.7$ is the high frequency dielectric function of SiC, $\sigma_L=969\ \mathrm{cm}^{-1}$, $\sigma_T=793\ \mathrm{cm}^{-1}$ are the natural vibrational wavenumbers of the longitudinal (L) and transverse (T) optical modes, and $\Gamma=4.76\ \mathrm{cm}^{-1}$ is a damping term [118]. The region between σ_T and σ_L is the restrahlen band of the material. An external light illumination within this band cannot propagate in the material. This results in a reflectivity close to 1 in the restrahlen band, and therefore an absorptivity close to 0. The directional-spectral emissivity of an object being equal to its directional spectral absorptivity according to Kirchhoff's law, the radiation of thermal emission from a SiC surface is expected to be low in the restrahlen band in comparison

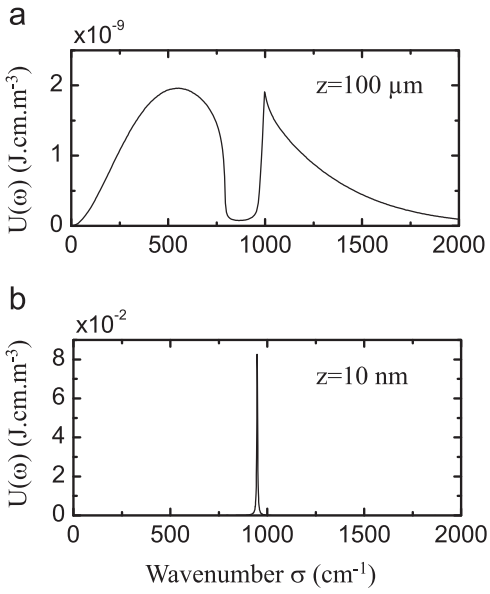

Fig. 13. Spectrum of the local density of electromagnetic energy (thermal emission spectrum) of a semi-infinite sample of SiC at 300 K calculated at two different heights above its surface. (a) At 100 μm (far field) the blackbody-like envelop and the restrahlen band are observed. (b) At 10 nm (near field) a quasi-monochromatic peak is predicted at 948 cm^{-1} with an intensity much larger than the far-field intensity [101].

to a perfect black-body radiator. Eq. (60) has been used to calculate the spectrum of the local density of electromagnetic energy $U(z,\omega)$ in the far field ($z = 100$ μm) above a surface of SiC at 300 K. It is shown in Fig. 13(a).

The far-field spectrum exhibits indeed a blackbody like envelop and the expected broad minimum in the restrahlen band. As Eq. (60) is valid in any regime, the spectrum of $U(z,\omega)$ has also been calculated at shorter distances from the SiC surface [101]. A striking new feature appears within subwavelength distance from the material, i.e. for values of $z < \lambda_{max} \approx 10$ μm. It consists of a sharp peak superimposed on the far-field broadband spectrum. Calculations based on Eq. (60) show that the peak intensity increases dramatically as the height above the SiC surface is further reduced. In the near field at a height $z = 10$ nm, the calculated spectrum of $U(z,\omega)$ shown in Fig. 13(b) indicates that the intensity of this peak is several orders of magnitudes larger than the maximum of the far-field thermal emission spectrum. Such a short distance from the interface coincides with the quasielectrostatic limit in which Eq. (60) reduces to Eq. (64). The latter gives a better insight about the origin of the peak. The theoretical value of the peak position $\sigma_{max} = 948\ cm^{-1}$ satisfies the condition $\epsilon'_{SiC}(\sigma_{max}) = -1$. At this value, the denominator in Eq. (64) is minimum for a given value of z, which produces a sharp maximum in the LDOS. The dispersion relation of the surface phonon polaritons at the interface between vacuum and SiC satisfies

$$K^2 = 2\pi\sigma^2 \frac{\epsilon_{SiC}(\sigma)}{\epsilon_{SiC}(\sigma)+1} \tag{66}$$

Its representation is shown in Fig. 14. As expected, the peak of the LDOS at σ_{max} coincides with modes with large values of K

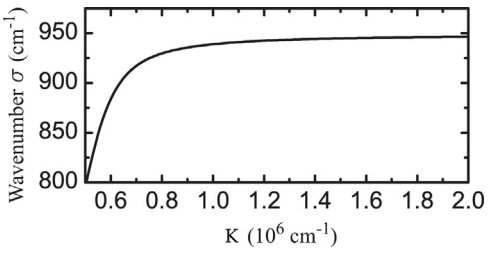

Fig. 14. Dispersion curve for surface phonon polaritons at a SiC/vacuum interface.

located near the asymptote. Such modes have $K > k_0$ and therefore correspond to surface waves. In other words, a SiC surface acts as a nonradiating source for wavenumber values $\sigma \approx \sigma_{max}$. Due to the large value of $|K|$ of the modes near σ_{max} with respect to plane propagating waves in free space [49], detecting their contribution to the local electromagnetic energy density requires a probe which can be approached at a distance smaller than λ_{max} from the SiC surface. Such a probe would detect a quasi-monochromatic thermal emission in the near-field due to the dominating contribution of surface modes to $U(z,\omega)$. This behavior strongly contrasts with the far-field thermal emission of SiC which spans over a broad energy range [101].

High harmonic demodulation of the signal is a known method in scattering NSOM microscopy to extract non-linear variations of the electromagnetic field from regions nearest the sample surface. The signal S modulated by a small oscillation of the tip position of maximum amplitude a normal to the sample surface $\Delta z = a\cos(\Omega t)$ around its average height z_0 can be approximated by an expression of the form

$$S(z_0+\Delta z) = A + B\frac{dS}{dz}(z_0)\cos(\Omega t) + C\frac{d^2S}{dz^2}(z_0)\cos(2\Omega t) + \cdots \tag{67}$$

where A, B, C are constants [119]. This method was used in TRSTM imaging on samples made of gold patterns on SiC to enhance the contribution from the surface phonon polaritons at the surface of SiC in the measured signal. Fig. 15(b) and (c) compares two TRSTM images obtained on a square region of SiC surrounded by 100 nm thick gold, whose topography is shown in Fig. 15(a), when demodulating the signal at 2Ω with a lock-in amplifier. Fig. 15(b) was obtained with a bandpass filter (bandwidth $\approx 100\ cm^{-1}$) detuned by $250\ cm^{-1}$ above the LDOS peak in SiC, while Fig. 15(c) was obtained with a filter overlapping the LDOS peak. A higher TRSTM signal at 2Ω is clearly observed in Fig. 15(c) on the SiC square area with respect to the surrounding gold. It is due to the contribution of the surface phonon polaritons within the peak which are highly confined near the SiC surface, producing a higher TRSTM signal taken at 2Ω than the surrounding gold film where surface plasmon polaritons exist but are poorly confined. A lower signal at 2Ω is observed on SiC in Fig. 15 (b) because in that situation the filter selects a wavenumber above the asymptote of the dispersion curve. The LDOS is thus close to 0 and no thermal emission due to surface phonon

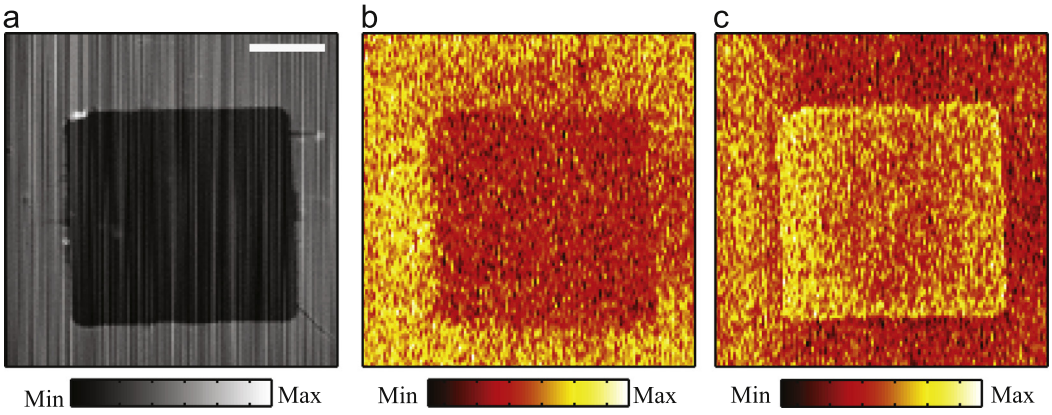

Fig. 15. (a) Topographic AFM image of a square of SiC in a 100 nm thick gold film. (b) Corresponding near-field thermal emission image taken at 2Ω when a bandpass filter detuned by 250 cm^{-1} above the peak in the LDOS is placed in front of the detector, and (c) when a bandpass filter which overlaps the peak in the LDOS is used. At 2Ω, the components of the TRSTM signal which are non-linear are enhanced. The highly confined modes of surface phonon polaritons within the peak of the LDOS of SiC then produce a higher TRSTM signal than the surface plasmon polaritons on gold when a filter which overlaps the SiC resonance is used. With a filter out of resonance, a higher signal is found on gold as the LDOS of the surface phonon polaritons on SiC is close to zero. These experimental observations are consistent with the theoretical predictions made in Fig. 12 which show that around the peak, the LDOS at nanometer distance from the sample is higher on SiC than on gold. Due to their large wavevector, the surface phonon polaritons on SiC at the resonance peak are highly confined, and the non-linear TRSTM signal components at 2Ω are in this case more important when the tip is on SiC than when it is on gold. Scale bar = 5 μm. (For interpretation of the references to color in this figure caption, the reader is referred to the web version of this paper.)

polaritons is detected. It is not the case for the surface plasmon polaritons on Au which exist up to the visible range and therefore have a non-zero LDOS even at the wavenumber set by the filter in Fig. 15(b).

The measurement of TRSTM images with bandpass filters have first provided a qualitative evidence of the sensitivity of TRSTM probes to the LDOS spectrum [98]. Scanning probes combining the capability of the TRSTM to image the LDOS with sub-wavelength resolution with local near-field spectroscopy measurements have subsequently been developed [107,108,110]. Fig. 16(a) shows a scanning probe allowing us to perform thermal infrared near-field spectroscopy (TINS) on a hot sample surface in TRSTM mode [98], or reversely, using a hot AFM tip as a local heater of the sample [107]. In the latter configuration, specially designed AFM probes allow for resistive tip heating. Nominal tip temperature of up to $T_{tip} = 700$ K can be achieved, producing a heating of the sample surface near the tip, experimentally estimated to be at least $T_{sample} = 550$ K. Once the temperature of the sample is raised, the AFM tip is used to scatter the near-field thermal emission to the far-field in order to perform its spectral analysis. Fig. 16(b) shows the same TRSTM instrument as in Fig. 11 adapted for point spectroscopy measurements [108] and superresolved hyperspectral measurements [110].

As for TRSTM, it uses a tungsten AFM tip to scatter the near-field thermal emission. The sample is placed on a flat resistor and isothermally heated up to 450 K typically, but operation at even lower temperature was also demonstrated [98,108]. Except for differences regarding the method used for the sample heating in order to populate the modes by thermal excitation, the two instruments shown in Fig. 16 operate according to the same principle as far as measuring the spectrum of the local energy density associated to the LDOS is concerned. The AFM tip, which oscillates at frequency Ω acts as a scatterer coupling the near field to the far field. The scattered near-field thermal emission is collected and guided towards a HgCdTe infrared detector through a Fourier transform infrared spectrometer (FTIR). A lock-in amplifier connected to the output of the detector allows one to measure the signal at Ω or, if possible, at a higher harmonic. The latter is crucial to validate unambiguously the near-field origin of the signal [108]. The FTIR includes a Michelson interferometer with variable path difference. Such a set-up is appropriate to investigate the temporal coherence of the scattered near-field signal both in the frequency [107,108,110] or in the time [111] domain.

Near-field thermal emission spectroscopy has been performed with the instruments shown in Fig. 16 to probe the LDOS on materials supporting surface wave excitations [107–111] or molecular resonances [107,109]. The expression of the LDOS in the near-field limit given in Eq. (64) strongly suggests the existence of a close relation between the near-field thermal emission spectrum which is the quantity experimentally measured and the dielectric function of the material located under the scattering tip. Besides probing the LDOS, this opens novel perspectives for the infrared spectroscopy of materials with subwavelength spatial resolution. This aspect is illustrated in the example of Fig. 17 which compares an experimental TINS spectrum obtained on a polytetrafluoroethylene (PTFE) surface, and a calculated LDOS spectrum on the same material [107]. The two spectra are clearly very similar.

In Fig. 18(a) and (b), we compare near-field thermal emission spectra obtained with a TRSTM on two polar materials supporting surface phonon polaritons, silicon carbide (SiC) and silicon dioxide (SiO_2), with calculated spectra of the LDOS based on Eq. (64) [108,113]. For both materials a peak in the LDOS spectra is expected at $\sigma_{max} = 948\ cm^{-1}$ for SiC and at $\sigma_{max} = 1156\ cm^{-1}$ for SiO_2. A large damping term in the expression of the dielectric function of SiO_2 is responsible for the rather large broadening of the LDOS, in comparison with SiC for which the

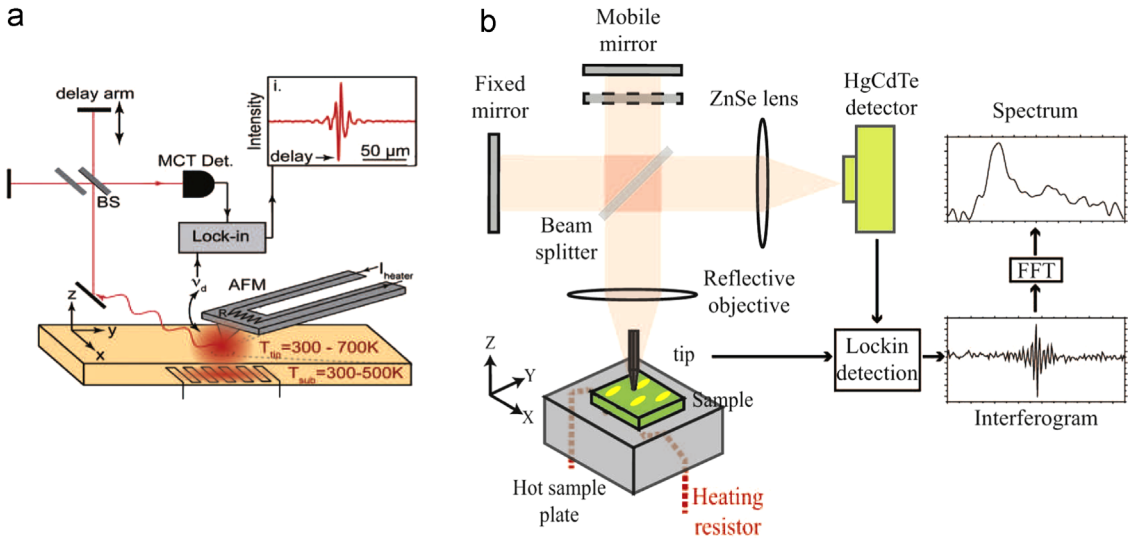

Fig. 16. (a) Near-field probe allowing to perform thermal infrared near-field spectroscopy of the spectral energy density associated with the LDOS. The probe utilizes a heated sample holder, or reversely a hot AFM tip to perform a thermal excitation of the modes at the sample surface. The tip scatters the near-field thermal emission which is analyzed by means of a FTIR spectrometer. Adapted from Ref. [107]. (b) Thermal radiation scanning tunnelling microscope (TRSTM) combined with a FTIR spectrometer to perform near-field spectroscopy of the LDOS by measurements of the spectral energy density. The set-up utilizes an oscillating tungsten AFM tip to scatter the near-field thermal emission on an isothermal sample whose temperature is below 470 K [108,110].

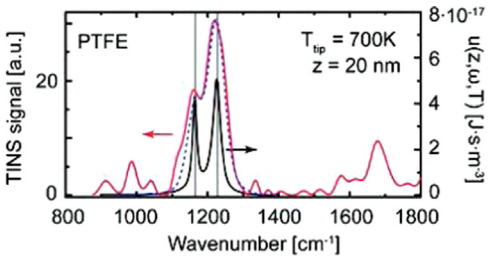

Fig. 17. Experimental thermal infrared near-field spectrum (TINS) obtained on a polytetrafluoroethylene (PTFE) sample (red curve) compared with the spectral energy density associated with the LDOS (black curve). From Ref. [107]. (For interpretation of the references to color in this figure caption, the reader is referred to the web version of this paper.)

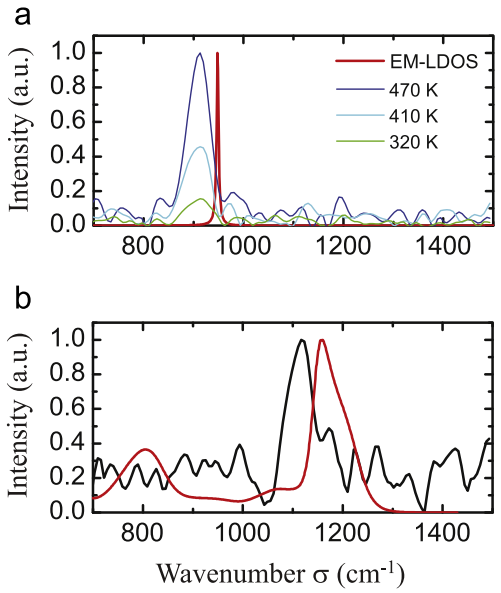

Fig. 18. (a) Experimental spectra of the near-field thermal emission associated with the LDOS of SiC measured with a TRSTM at three temperatures of the sample: 471 K (dark blue curve), 410 K (light blue curve), and 320 K (green). A single quasi-monochromatic peak is observed in the near-field thermal emission reflecting its partial temporal coherence associated to surface phonon polariton modes, as expected from calculations of the LDOS (red curve). The LDOS peak is only expected in the near-field at $\sigma_{max} = 948\ cm^{-1}$, but it is slightly red-shifted and broadened in the experimental spectra due to the near-field interaction between the tip and the sample, as discussed in the text. (b) Comparison of the experimental spectrum of the near-field thermal emission of SiO_2 showing a quasi-monochromatic peak as well (black curve) which is slightly red shifted from the LDOS peak (red curve) of this material [108,110]. (For interpretation of the references to color in this figure caption, the reader is referred to the web version of this paper.)

peak is much sharper. Fig. 18(a) shows that near-field thermal emission spectra measured at various temperatures of the SiC sample all exhibit a peak at $\sigma_{exp}^{SiC} = 913\ cm^{-1}$. The peak intensity decreases with the temperature, as expected for electromagnetic surface modes which are thermally excited. A single peak was also reported in TINS experiments performed on SiC using a heated tip [107,111]. This quasi-monochromatic peak is the signature of the partial temporal coherence of the near field thermal emission induced by the surface phonon polaritons.

The calculated LDOS peak of SiC at $\sigma_{max} = 948\ cm^{-1}$ is also represented in Fig. 18(a) (red curve). A red shift and a broadening of the near-field thermal emission peaks measured with TRSTM and TINS is observed with respect to the LDOS peak, whose values seem to strongly depend on the characteristics (shape, material) of the tip used to scatter the near-field thermal emission in the spectroscopy measurement [108,107,111]. A similar effect is also observed on SiO_2 in Fig. 18(b), but the broadening is less visible due to the intrinsic broadening of the LDOS of SiO_2. The discrepancy between the measured near-field thermal emission spectra using a scattering probe and the LDOS finds its origin in the near-field interaction between the tip and the sample material under it [108,113], and in a possible effective change of the

dielectric environment altering the surface phonon polariton resonance condition [111].

The assumption that the tip of a TRSTM is an ideal probe which only "reads" the near-field thermal emission, and hence the LDOS at its position is not valid. In fact, the sole presence of the tip at the sample surface modifies the field which would be there if the tip was absent. Fig. 19(a) gives a sketch of a theoretical model detailed in Ref. [113] which gives a full description of the interaction between a dipolar tip and the sample. This full dipole model goes beyond the quasi-electrostatic approximation by taking account of the phase acquired by the field scattered by the tip dipole and reflected on the sample. In reality, an infinite number of reflections of the field scattered by the dipolar tip occur between the latter and the sample surface. The multiple reflections are described in the model by means of a dressed polarizability tensor which depends on the reflected Green tensor giving the field at the tip position from an elementary dipole at the tip position. The components of this dressed polarizability tensor multiply various projections of the LDOS, including square terms and crossed products of electric and magnetic components. The signal at the detector also results from both the direct propagation of the scattered field to the detector, and from the indirect propagation after one reflection on the sample. The latter is described by its Fresnel coefficients [108]. Fig. 19(b) and (c) presents the comparison between the peaks experimentally observed in TRSTM measurements of near-field thermal emission spectra on SiC and SiO_2 and theoretical spectra based on the full dipole model. The latter was computed using the tip and the sample dielectric function, and assuming that the scattering dipole which mimics the elongated tungsten tip geometry is located 1.6 μm above the sample. The good agreement found in both cases between the experimental and the theoretical curves clearly indicates that the full dipole model grasps the essential parameters which characterize the coupling between the tip and the sample [108,110].

The full dipolar tip model sketched in Fig. 19(a) indicates that the near-field thermal emission signal from a scattering TRSTM tip can in general not be assumed to be simply proportional to the LDOS because it also depends on other terms which are functions of the dielectric properties of the sample and/or the tip. Nevertheless, the signal in the TRSTM and related techniques [98,106–108] and the LDOS are closely related and the theory allows one to evaluate the intrinsic instrumental response of the probe [108,113]. This is the usual requirement for most imaging and spectroscopy techniques. On the other hand, TRSTM and TINS probes still have the unique ability to measure both the spatial and the spectral variations of the near-field thermal emission in the mid-infrared region with subwavelength resolution. Regarding near-field FTIR spectroscopy, the major advantage of TINS and TRSTM is that the probes do not require any external sources, while they intrinsically operate over the full spectral range required to characterize the sample [107,108]. Until recently, the near-field thermal emission spectroscopy probes had only been used to record spectra at single locations and on homogeneous samples. Important progresses have been accomplished with

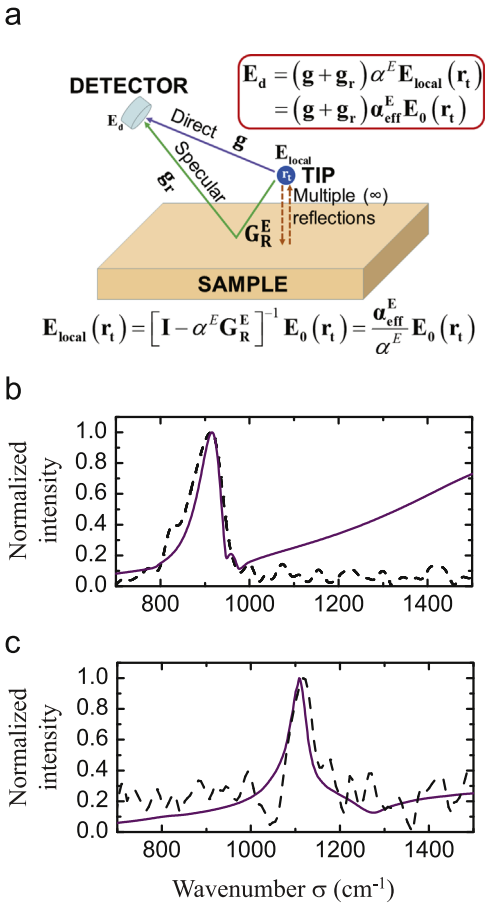

Fig. 19. (a) Illustration of the full dipole model discussed in Refs. [108,113], used to calculate the effect of the tip on the near-field thermal emission spectra. The electromagnetic field of the thermally emitted photons scattered by the tip (assumed to be a spherical dipole) can reach the detector either being before reflected on the sample or not. The local field at the tip position depends on multiple reflections on the sample, leading to an effective (or dressed) polarizability of the tip. Only an electric dipole is considered here, for a full description see Ref. [113]. (b) and (c) Simulations of the near-field thermal emission spectra based on the model for SiC and SiO_2 (purple curves), showing a good agreement with the experimental curves (black curves). Both the red-shift and broadening observed in the experiments with respect to the LDOS are reproduced by the model. Adapted from Ref. [108]. (For interpretation of the references to color in this figure caption, the reader is referred to the web version of this paper.)

the TRSTM to combine its subwavelength imaging capabilities with near-field thermal emission spectroscopy [110]. This has allowed for the first time the measurement of hyperspectral images on heterogeneous samples supporting surface plasmon polaritons in some area, and surface phonon polaritons in some others. The probe could be used to investigate the spatial evolution of the LDOS at a boundary where the two kinds of thermally excited surface waves meet. As an example, Fig. 20 shows the result of an hyperspectral line scan in which a near-field thermal emission FTIR spectrum has been acquired every 1 μm [Fig. 20(a)] and every 100 nm [Fig. 20(b), (c)] along a line crossing the boundary between a SiC substrate and a Au film [110]. The recording of the second harmonic demodulated signal on the smaller hyperspectral line scan allows one to improve even further the spatial resolution.

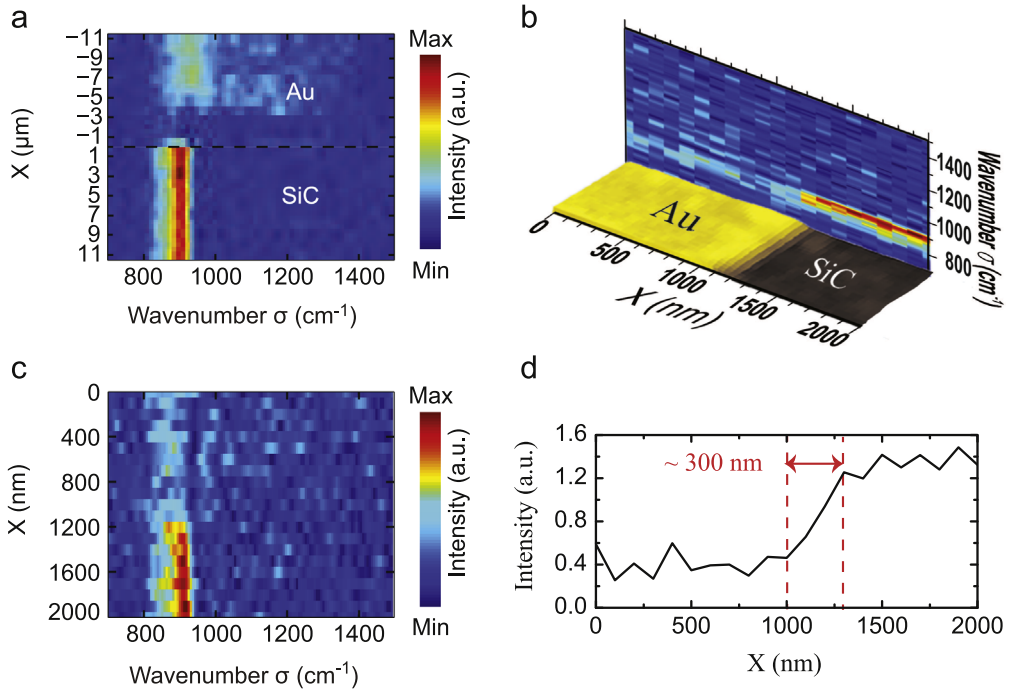

Fig. 20. (a) Experimental spectra of the near-field thermal emission associated to the LDOS taken at Ω every 1 μm along a 21 μm straight line crossing a SiC/Au boundary. (b) Experimental spectra of the near-field thermal emission associated to the LDOS taken at 2Ω every 100 nm along a 2 μm straight line crossing a SiC/Au boundary. The second harmonic demodulation of the signal (2Ω signal) is used to improve the spatial resolution. (c) The image is a hyperspectral representation of the measurements, showing at the same time the AFM topography of the boundary between the SiC substrate and a gold (Au) film (horizontal plane) and the spectra measured along the line (vertical plane). A quasi-monochromatic peak is clearly observed when the tip is on SiC. (d) TRSTM signal at the peak as a function of the position along the line, showing that this spectral feature disappears within less than 300 nm. Besides probing the LDOS, the results demonstrate that TRSTM allows us to perform a novel type of FTIR spectroscopy of materials, with a resolution which is well beyond the diffraction limit. Adapted from Ref. [110].

The TRSTM spectra on SiC exhibit the sharp quasimonochromatic peak at $\approx 915\,\mathrm{cm}^{-1}$ due to surface phonon polaritons, which disappears within less than 300 nm on the Au film. The measurements provide an estimate of the spatial resolution of the TRSTM for near-field FTIR spectroscopy [110]. While classical far-field FTIR spectroscopy has a resolution of tens of micrometers due to the diffraction limit, the TRSTM allows one to beat this limit by nearly two orders of magnitude, and to detect the contribution of surface waves in the near-field thermal emission spectrum, which would not be accessible otherwise. Near-field thermal emission imaging and spectroscopy should find useful applications not only in the field of plasmonics, but also as new tools to characterize the infrared dielectric properties of nanomaterials.

7. Spatial coherence and cross density of states

7.1. Field–field correlation and Green's function

In the description of blackbody radiation in Section 5.1, we have introduced the cross spectral density $W^E_{jk}(\mathbf{r},\mathbf{r}',\omega)$ as a measure of the spectral correlation of the components j and k of the electric field at two different points. Since $j,k \in (x,y,z)$, it defines a cross spectral density matrix that is the basic quantity in the theory of spatial coherence [120]. Indeed, for a statistically stationary field, the cross spectral density can be represented as a field–field correlation function in the frequency domain by the relation

$$\langle E_j(\mathbf{r},\omega)E^*_k(\mathbf{r}',\omega')\rangle = 2\pi W^E_{jk}(\mathbf{r},\mathbf{r}',\omega)\delta(\omega-\omega'). \tag{68}$$

The delta function shows that for a stationary field two different frequencies are uncorrelated.

From the fluctuation–dissipation relation (51), an interesting connection is established between the spectral field–field correlation function at two different points and the imaginary part of the Green function connecting these two points. Indeed, we have

$$\langle E_j(\mathbf{r},\omega)E^*_k(\mathbf{r}',\omega')\rangle = 8\pi\mu_0\omega\,\mathrm{Im}[G^E_{jk}(\mathbf{r},\mathbf{r}',\omega)] \times\Theta(\omega,T)\delta(\omega-\omega') \tag{69}$$

where $\mathbf{G}^E$ is the electric Green function. The connection between spatial field–field correlations and the imaginary part of the Green function is a well-known result in the study of equilibrium electromagnetic radiation [22,49,99,100]. The imaginary part of the Green function at two different points also appears in a number of situations where the spatial coherence of random fields produced by random noise [121,122], partially coherent sources [123], or multiple scattering [124–127] needs to be characterized. It turns out that the imaginary part of the Green function at two different points plays for the field–field correlation function a role that is similar to that played by the LDOS for the energy density. Indeed, for a random excitation of the medium, the remaining spatial correlation (spatial coherence) is given by the

imaginary part of the Green function that can be understood as the quantity describing the intrinsic spatial coherence of the medium sustained by the underlying eigenmodes, as initially put forward in Ref. [128]. This leads to the introduction of the concept of cross density of states (CDOS) that will be examined in detail in the next section.

7.2. Cross density of states

7.2.1. Definition

The cross density of states (CDOS) has been introduced as a quantity that characterizes quantitatively the spatial coherence of light in or out of any photonic and plasmonic structure [128]. Say differently, this quantity is an accurate indicator to describe the overall spatial extent of the eigenmodes of the structure. In particular, we will refer to it to address the spatial localization of light at the near-field of disordered fractal metallic films. We have seen previously that the imaginary part of the Green function taken at two different points plays a crucial role in many situations where field–field correlations are addressed [49,121,122,124,129]. Based on this observation and on the LDOS expression, we define a two-points quantity that we will refer to as CDOS by [128]

$$\rho_e(\mathbf{r},\mathbf{r}',\omega)=\frac{2\omega}{\pi c^2}\mathrm{Im}\left[\mathrm{Tr}\mathbf{G}^E(\mathbf{r},\mathbf{r}',\omega)\right]. \tag{70}$$

Although we define here a CDOS based on the electric Green function, the same can be done using the magnetic Green function. The choice made here amounts to considering spatial coherence in terms of spatial correlations of the electric field.

The prefactor in Eq. (70) has been chosen such that the CDOS coincides with the LDOS when $\mathbf{r}=\mathbf{r}'$. The physical picture of the LDOS is the counting of all eigenmodes of the structure crossing the point considered. In the same way, the CDOS can be interpreted as a quantity describing the counting of all eigenmodes connecting two different points. For example, a large CDOS (larger than the vacuum CDOS) would allow two quantum emitters at $\mathbf{r}$ and $\mathbf{r}'$ to couple efficiently. It would also ensure coherent (correlated) fluctuations of the light fields at $\mathbf{r}$ and $\mathbf{r}'$ under thermal excitation [49].

7.2.2. Non-absorbing closed cavity

This simple picture can be expanded on a more rigorous basis in the case of a non-absorbing medium placed in a closed cavity. As for the LDOS, the mode expansion of the Green function equation (6) can be used to rewrite the CDOS in the form

$$\rho_e(\mathbf{r},\mathbf{r}',\omega)=\sum_n\delta(\omega-\omega_n)\mathrm{Re}\left[\mathbf{e}_n^*(\mathbf{r}')\cdot\mathbf{e}_n(\mathbf{r})\right] + \frac{2\omega}{\pi}\sum_n\mathrm{PV}\left[\frac{1}{\omega_n^2-\omega^2}\right]\mathrm{Im}\left[\mathbf{e}_n^*(\mathbf{r}')\cdot\mathbf{e}_n(\mathbf{r})\right]. \tag{71}$$

This expression can be simplified by using the reciprocity theorem which reads as $G_{ij}^E(\mathbf{r},\mathbf{r}',\omega)=G_{ji}^E(\mathbf{r}',\mathbf{r},\omega)$, where G_{ij}^E is any matrix element of the tensor Green function. From the mode expansion equation (6), the reciprocity theorem becomes

$$\sum_n\left\{\mathrm{PV}\left[\frac{1}{\omega_n^2-\omega^2}\right]+\frac{i\pi}{2\omega_n}\delta(\omega-\omega_n)\right\} \times\left[\mathbf{e}_n^*(\mathbf{r}')\otimes\mathbf{e}_n(\mathbf{r})-\mathbf{e}_n(\mathbf{r}')\otimes\mathbf{e}_n^*(\mathbf{r})\right]=\mathbf{0}. \tag{72}$$

Since $\mathbf{e}_n^*(\mathbf{r}')\otimes\mathbf{e}_n(\mathbf{r})-\mathbf{e}_n(\mathbf{r}')\otimes\mathbf{e}_n^*(\mathbf{r})=2i\mathrm{Im}[\mathbf{e}_n^*(\mathbf{r}')\otimes\mathbf{e}_n(\mathbf{r})]$, the imaginary part of Eq. (72) is

$$\sum_n\mathrm{PV}\left[\frac{1}{\omega_n^2-\omega^2}\right]\mathrm{Im}\left[\mathbf{e}_n^*(\mathbf{r}')\otimes\mathbf{e}_n(\mathbf{r})\right]=\mathbf{0} \tag{73}$$

showing that the last term in Eq. (71) vanishes. This implies that the expression of the CDOS for a non-lossy system embedded in a close cavity reduces to

$$\rho_e(\mathbf{r},\mathbf{r}',\omega)=\sum_n\delta(\omega-\omega_n)\mathrm{Re}[\mathbf{e}_n^*(\mathbf{r}')\cdot\mathbf{e}_n(\mathbf{r})]. \tag{74}$$

This expression explicitly shows that the CDOS sums up all eigenmodes connecting $\mathbf{r}$ to $\mathbf{r}'$ at frequency ω, weighted by their strength at both points $\mathbf{r}$ and $\mathbf{r}'$.

7.2.3. Phenomenological theory for weak losses

In the case of an open and/or absorbing medium, the rigorous introduction of a basis of eigenmodes is more complex. Approaches have been developed in the quasi-static limit [130], or based on the introduction of quasi-normal modes in the fully retarded regime [15], or using statistical properties of the spectral expansion of non-Hermitian matrices [131]. Recently the quasi-normal approach has been used to provide a rigorous expansion of the CDOS in open and absorbing systems [16]. Here, we restrict ourselves to the phenomenological approach already used in Section 3.3. Assuming weak leakage, the expansion of the Green function equation (22) can be used to rewrite the CDOS in the form

$$\rho_e(\mathbf{r},\mathbf{r}',\omega)=\sum_n\frac{\gamma_n}{2\pi}\frac{\mathrm{Re}[\mathbf{e}_n^*(\mathbf{r}')\cdot\mathbf{e}_n(\mathbf{r})]}{(\omega-\omega_n)^2+(\gamma_n/2)^2} \tag{75}$$

where γ_n is the damping rate of mode n. Eq. (75) generalizes the expansion of the CDOS in the case of weakly lossy systems. Essentially this procedure amounts to replacing the Dirac delta function in Eq. (74) by a Lorentzian lineshape. Both expressions (Eqs. (74) and (75)) can be connected in the limit of vanishing losses using the identity

$$\lim_{\gamma_n\to0^+}\frac{1}{\pi}\frac{\gamma_n/2}{(\omega-\omega_n)^2+(\gamma_n/2)^2}=\delta(\omega-\omega_n). \tag{76}$$

7.2.4. Spatial coherence and polarization

The trace operator in the definition of the CDOS given by Eq. (70) has been introduced to restrict the CDOS as a concept characterizing spatial coherence by washing out the polarization degrees of freedom. This trace operator enters the definition of the degree of spatial coherence known in coherence theory [120]. In order to describe the coherence *and* polarization properties, a CDOS tensor can be defined that

takes into account cross-polarized components:

$$\boldsymbol{\rho}_e(\mathbf{r},\mathbf{r}',\omega)=\frac{2\omega}{\pi c^2}\mathrm{Im}\left[\mathbf{G}^E(\mathbf{r},\mathbf{r}',\omega)\right]. \tag{77}$$

This tensor shows that spatial coherence and polarization are intrinsically linked, a well-known issue in coherence theory [132]. Referring again for the sake of physical insight to the canonical situation in which a set of discrete eigenmodes can be defined, the CDOS tensor reduces to

$$\boldsymbol{\rho}_e(\mathbf{r},\mathbf{r}',\omega)=\sum_n \delta(\omega-\omega_n)\mathrm{Re}[\mathbf{e}_n^*(\mathbf{r}')\otimes\mathbf{e}_n(\mathbf{r})]. \tag{78}$$

This expression leads to a general term of the CDOS tensor given by

$$\rho_{e,ij}(\mathbf{r},\mathbf{r}',\omega)=\sum_n \delta(\omega-\omega_n)\mathrm{Re}[e_{n,i}^*(\mathbf{r}')e_{n,j}(\mathbf{r})] \tag{79}$$

where $e_{n,i}$ is the component of eigenmode $\mathbf{e}_n$ along the unit vector $\mathbf{u}_i$ defining the direction i. Eq. (79) shows that the co-polarized components along the direction $\mathbf{u}_i$ are described by the diagonal matrix elements $\rho_{e,ii}$ of the CDOS tensor, while the cross-polarized components between directions $\mathbf{u}_i$ and $\mathbf{u}_j$ are described by the non-diagonal elements $\rho_{e,ij}$. The scalar CDOS as defined in Eq. (70) only involves the co-polarized components of the CDOS tensor.

8. LDOS and CDOS on disordered plasmonic films

The LDOS and CDOS are fundamental concepts in the description of the photonic properties of complex samples. Their relevance for plasmonics is illustrated by the study of semicontinuous metallic films made of noble metals that are outstanding examples of complex systems in plasmonics. Around the percolation threshold, these plasmonic films are known to present unusual optical properties due to the strongly disordered and multiscale geometry of percolation clusters. These optical properties cannot be explained by using a mere effective medium theory, and extrapolated from either the dilute or continuous side. A picture of such samples is shown in Fig. 21. Thin gold films are obtained by depositing gold onto a glass cover slip. In the experiments described below, gold has been deposited by using e-beam evaporation. The massive thickness of the film can be monitored with a quartz microbalance located inside the vacuum deposition chamber. Films shown in Fig. 21 have a thickness going from 1.5 nm to 20 nm, obtained with a deposit speed of about 1 Å/s. The variation of the color of the samples with increasing thickness is a clear indicator of the rich optical properties. An explanation of such variation can be found by looking at the transmission electron microscope (TEM) images of the samples which are reported in the second row of Fig. 21. The morphology of the films exhibits a clear variation with the film thickness. For small quantities of deposited gold, the film is composed of regularly shaped clusters exhibiting independent plasmon resonances that are responsible for the pink color of the film, as it is confirmed by far field spectral measurements. Large quantities of deposited gold bring towards continuous films, which have optical properties similar to bulk gold. For a massive thickness of the order of 10 nm, the film is formed by an arrangement of large disordered clusters, connecting two opposite sides of the sample (the sample is said to be percolating), which are responsible for the blue color of the film. Indeed, far field spectra show a plateau extending from a wavelength of 600 nm to the infrared region of the spectrum [133]. By measuring the perimeter and the surface of the clusters on TEM images, one can demonstrate that clusters appearing for such massive thicknesses have a fractal dimension and therefore exhibit scale invariance.

An example of the perimeter versus surface plot is shown in Fig. 22, together with the corresponding TEM image, which is shown in the inset. Perimeter and surface are expected to follow the relation $P\propto S^{D/2}$ where $D=1$ for Euclidian clusters and $D=1.88$ for fractal clusters. As an example an Euclidian (fractal) cluster is colored in blue (red) on the TEM image and the corresponding point is highlighted in the same color in the perimeter versus surface plot. Fig. 22 clearly shows two different populations of clusters. By increasing the quantity of gold that is deposited, the number of fractal clusters increases. The amount of fractal clusters present in the sample can be quantified by calculating the ratio between the surface occupied by fractal clusters and the surface occupied by Euclidian clusters.

The unusual optical properties of fractal gold films have been studied theoretically and experimentally both in the far field and in the near field. These studies showed that the interplay between intrinsic material excitations (surface plasmons) and random scattering by multiscale (fractal) metallic clusters leads to spatial localization of the electromagnetic field in subwavelength areas (hot spots) [134–136]. At a given frequency, surface-plasmon modes consist of one or several hot spots, and can be localized (i.e., insensitive to the sample boundaries) or delocalized (spread over the entire system). The coexistence of both types of modes results from the self-similarity of the structure, and is referred to as inhomogeneous localization [134,137,138]. We have demonstrated the localization of surface plasmon modes on disordered metallic films with LDOS measurements, as it will be shown in detail in the following section. An advantage of our direct measurement of the LDOS is that the local intensity of both radiative and non-radiative (dark) modes is probed with the same weight. In an NSOM experiment, that is able to probe the intensity of both types of modes, scattering is necessary in order to couple external radiation to non-radiative modes, whereas radiative modes can be directly excited. This asymmetry is avoided by direct LDOS measurements.

8.1. Probing localized plasmons on disordered metallic films

In order to probe the LDOS in the near field of semicontinuous gold films we randomly spread some fluorescent beads on top of the films. The density of the beads (Invitrogen Red Fluosphere, diameter of 25 nm) was set such that the average distance between two beads was of the order of several microns. Therefore, we were able to address single beads by exciting them and collecting their fluorescence through a high

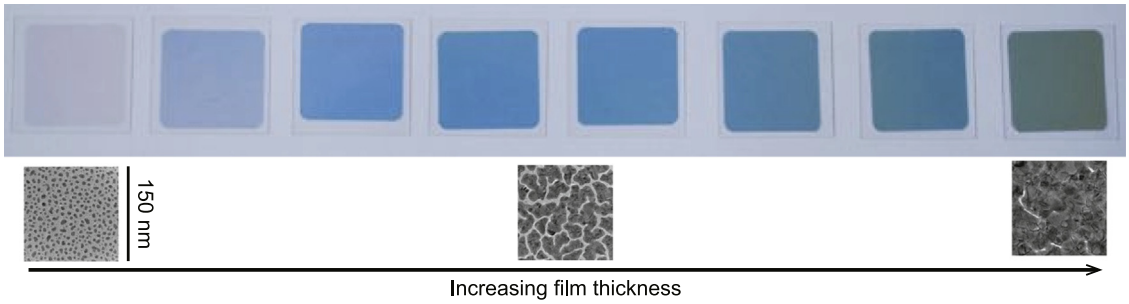

Fig. 21. First row: transmission image of thin gold films of different thicknesses deposited on a glass cover slip. The thickness of the film ranges from 1.5 nm to 20 nm. Second row: TEM images of the films, showing the appearance of fractal clusters. (For interpretation of the references to color in this figure caption, the reader is referred to the web version of this paper.)

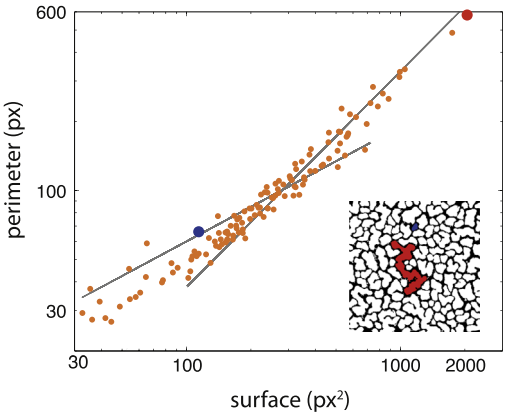

Fig. 22. Plot of the perimeter versus surface for the clusters in the TEM image shown in inset. The cluster colored in red has a fractal dimension while the cluster colored in blue is Euclidian. The corresponding points in the plot are highlighted in red and blue respectively. Adapted from Ref. [60]. (For interpretation of the references to color in this figure caption, the reader is referred to the online version of this paper.)

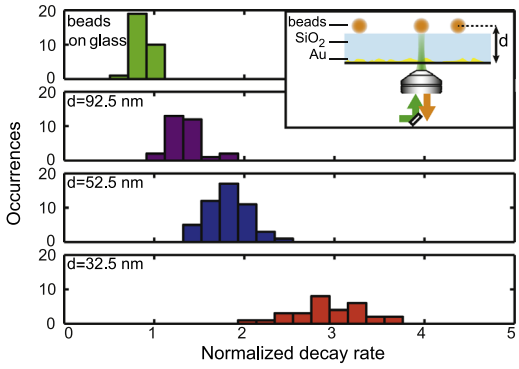

Fig. 23. Decay rate distributions measured at different distances d between the gold film and the fluorescent beads. The inset shows a sketch of the experimental setup. From Ref. [47].

numerical aperture objective (oil immersion objective, NA= 1.3). The excitation is performed by using a super-continuum laser (Fianium SC450) filtered at 560 nm. Fluorescence filters centered at 607 nm with a bandwidth of 70 nm are used to separate fluorescence photons from excitation photons. Fluorescence photons are detected by an avalanche photodiode (Perkin Elmer SPCM-AQR-15). Lifetime measurements are performed by time-correlated single photon counting (PicoQuant TimeHarp200). The samples are fabricated as follows. First, a gold layer with a given thickness is deposited by e-beam evaporation on a glass cover-slip. Second, a silica spacer with a thickness d varying from 20 to 80 nm is deposited on the top of the gold layer. Third, fluorescent beads are spin-coated on the top of the silica layer. The decay rate of about 30 nanobeads located in different regions of the sample has been measured for each samples. Fig. 23 shows the obtained distributions, for a film close to the percolation threshold, as well as a sketch of the experimental setup (in the inset). The decay rate distribution measured for the beads spread on glass is also reported for the sake of completeness and can be interpreted as the measure obtained for an infinite distance between the beads and the metallic film. As one can see, the proximity of gold has a clear effect on both the mean value and the variance of the distribution. The mean value increases as the distance to the gold layer decreases, due to the fact that the beads feel a large number of non-radiative channels available for their decay, as also observed for a fluorescent emitter approaching a continuous metallic film. The variance of the distribution decreases when the spacer thickness increases. This effect would not occur on a continuous gold film and is intrinsically related to the presence of disorder. The trend observed on the variance of the decay rate distribution is due to spatial filtering of optical modes laterally confined on scales below the wavelength. Indeed, the field distribution in a plane at a distance d is exponentially filtered in Fourier space by a factor $\exp(-Kd)$ compared to the distribution at $d=0$ nm, with K being the spatial frequency in the transverse direction (parallel to the film plane). This is a feature of near-field optics. The study of the variance as a function of the distance to the film allows us to have an estimate of the spatial extension of the modes in the near field of the sample which is of the order of 60 nm [47]. In order to have a better insight in the experimental results we performed numerical simulations that are reported in Section 8.3.2.

The distributions of the LDOS in the near field of gold films have also been studied as a function of the gold layer thickness, for a fixed distance between the fluorescent beads and the gold layer. In this study we expect to observe the influence of the appearance of fractal clusters on the LDOS distribution. In this part of the experimental investigation, the thickness of the SiO_2

layer has been fixed at 20 nm and the massive thickness of the gold films has been varied between 1.5 and 20 nm. The acquisition of TEM images for each film allows us to introduce another quantity that better characterizes the quantity of gold on the sample: the gold filling fraction, which is the fraction of the surface occupied by gold over the total surface of the sample. For the samples under study, the gold filling fraction ranges from 0 (a bare glass coverslip, without gold) to 99% (corresponding to a massive thickness of 20 nm). In the following discussion, we will always refer to the quantity of gold deposited on the sample in terms of the filling fraction which is a more relevant quantity. The decay rate distribution measured for two gold films showing a completely different topology is shown in Fig. 24. The TEM images of the films, in the insets, show that the first film is formed by well separated clusters showing independent plasmonic resonances, while the second one is formed by fractal clusters.

As one can observe, the two distributions are completely different. As expected, the mean of the distribution is shifted towards large values of Γ as the quantity of deposited gold increases. The width of the distribution experiences an enhancement as the quantity of gold on the sample increases. This is due to the presence of disordered clusters on the sample. The scale-invariant nature of the fractal clusters is responsible for collective resonant plasmon excitations at any wavelength [139]. As a result, the amplitude of the plasmon modes exhibits large spatial fluctuations which are confined in a sub-wavelength region [135]. Furthermore, fractal films are characterized by the coexistence of spatially localized and delocalized modes, a phenomenon referred to as inhomogeneous localization in Ref. [137]. Delocalized modes are formed by a number of separated hot spots that are distributed in a region with size comparable to the sample size. The spatial fluctuations of the LDOS observed in this regime reflect the spatial fluctuations of the amplitude of individual modes, and therefore the nature of the modes.

In order to have a thorough understanding of the behavior of the LDOS on thin gold films, we measured the decay rate distribution for several films with gold filling fractions ranging from 0 to 99% and we characterized the distributions by measuring the mean value and the variance. Fig. 25(a) reports the normalized variance, $\sigma^2(\Gamma)/\langle\Gamma^2\rangle$, as a function of the filling fraction f.

As the filling fraction goes above 60%, an asymmetric double peak structure appears in the normalized variance of the LDOS, with a sharp peak occurring at $f=82\%$. Since huge fluctuations of the LDOS are expected to appear in correspondence with the onset of fractal clusters on the films, we plotted in Fig. 25(b) the ratio of the surface occupied by fractal clusters divided by the surface occupied by Euclidean clusters, which gives a measurement of the fractal character of a sample. This ratio grows very rapidly for $f > 65\%$, confirming the fact that huge LDOS fluctuations, and therefore plasmon localized modes, are strictly related to the presence of fractal clusters.

The correlation between huge LDOS fluctuations and the presence of localized modes is corroborated by a theoretical model built on the inverse participation ratio. The inverse participation ratio R_{IP} is a quantity used in the theory of Anderson localization to measure the spatial extent of wavefunctions [140] and it is defined by

$$R_{IP} = \frac{\int |\mathbf{E}(\mathbf{r})|^4 \, d^2r}{(\int |\mathbf{E}(\mathbf{r})|^2 \, d^2r)^2} \tag{80}$$

where in our case the integrals are performed along a plane

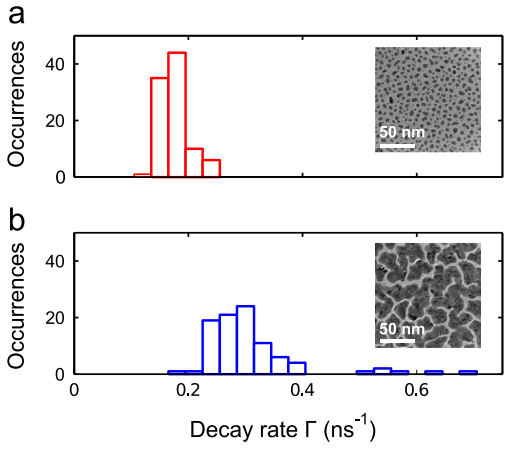

Fig. 24. Decay rate distributions measured for two different samples. The corresponding TEM images are shown in the inset. (a) $f=30\%$ (independent clusters). (b) $f=82\%$ (fractal clusters). From Ref. [60].

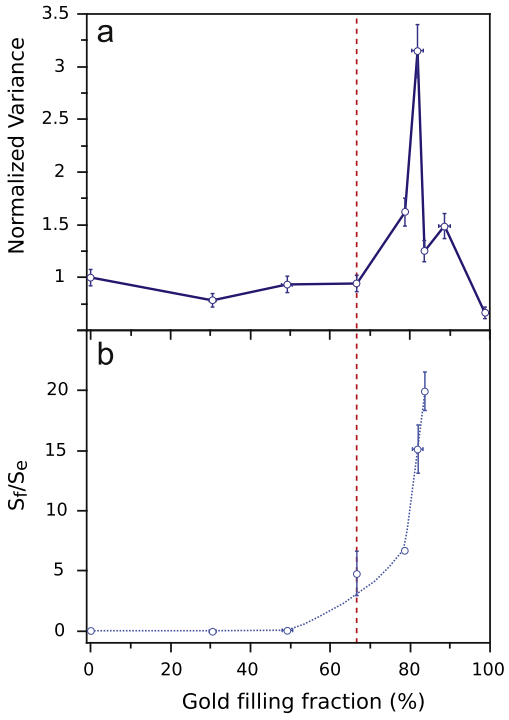

Fig. 25. (a) Normalized variance of the LDOS distributions measured in the near-field of several thin gold films. Data are shown as a function of the gold filling fraction measured from the TEM image of each sample. (b) Ratio between the surface of the sample occupied by fractal clusters and the surface occupied by Euclidian clusters as a function of the gold filling fraction. The dotted line is a guide for the eye. Adapted from Ref. [60].

parallel to the sample surface. For spatially localized modes, R_{IP} is independent of the sample size L, whereas for extended modes, R_{IP} scales as L^{-2} [141].

To get some insight, let us assume that the field is a pattern of N_h hot spots with intensity I_0 and extension ξ (each spot covers a surface ξ^2). Then $R_{IP} = (N_h\xi^2)^{-1}$ and gives the surface occupied by this pattern.

In order to connect the LDOS fluctuations to R_{IP}, we can make the following hypothesis. Since the hot-spot modes in the fractal clusters regime are known to have a chaotic behavior [134], the probability of having more than one mode giving a high electric field at a given point and given frequency is very small. Therefore, we can assume that at a given point $\mathbf{r}$ and at a given frequency ω, the electric field is dominated by one mode. In this case, the LDOS is essentially [see Eq. (4)]

$$\rho_e(\omega,\mathbf{r}) \propto \sum_n |\mathbf{E}_n(\mathbf{r})|^2 \delta(\omega-\omega_n) \simeq \frac{1}{\Delta\omega}|\mathbf{E}(\mathbf{r})|^2 \tag{81}$$

where $\Delta\omega$ is the spectral width of the mode and $|\mathbf{E}(\mathbf{r})|^2 = I(\mathbf{r})$ its local intensity. The approximation leading to the result in Eq. (81) is supported by the similarity between the double-peak structure of the normalized variance of the LDOS and the relative variance of the near-field intensity pattern measured by NSOM on similar samples [138].

Under the approximation in Eq. (81), the inverse participation ratio reads as

$$R_{IP} = \frac{\int |I(\mathbf{r})|^2 \, \mathrm{d}^2 r}{(\int I(\mathbf{r}) \, \mathrm{d}^2 r)^2} = \frac{\langle \rho_e^2 \rangle}{S\langle \rho_e \rangle^2} \tag{82}$$

where S is the sample surface. In the last equality, we have assumed ergodicity so that spatial and statistical averaging have been considered as equal [142]. This expression shows that measuring the LDOS fluctuations provides a direct measurement of R_{IP}. As a result, we can infer the increase of LDOS fluctuations as a signature of an increased contribution of localized modes. Indeed, for delocalized modes, one has N_h hot spots ($N_h \gg 1$), each of them with typical extent ξ [137]. The inverse participation is $R_{IP} \sim (N_h\xi^2)^{-1}$. For localized modes, one has $N_h \sim 1$, with a localization length $\xi_l \lesssim \xi$, so that $R_{IP} \sim \xi_l^{-2} \gg (N_h\xi^2)^{-1}$. This simple analysis shows that the peak in the LDOS fluctuations observed in Fig. 25(a) is the signature of an increased number of localized surface-plasmon modes in the regime where the disordered film contains a substantial fraction of fractal clusters.

8.2. Modelling plasmon excitations on disordered metallic films

In this section, we describe the numerical study of the near-field optical properties of disordered metallic films. The numerical method is implemented in two steps. Firstly, we use a Monte-Carlo algorithm to simulate the growth of a gold film during an evaporation/deposition process, and check that the geometrical properties of the film near the percolation threshold are in agreement with measurements. Secondly, we solve Maxwell's equations in 3D, taking into account polarization and retardation effects, in order to compute the LDOS and the CDOS. The computations are compared to the experimental results described in the previous section.

8.2.1. Simulation of the film growth process

Our first goal is to generate numerically disordered metallic films with the same geometrical features as the real films. The algorithm is based on a kinetic Monte-Carlo scheme as suggested in Ref. [144] and detailed in Ref. [143]. The idea is to randomly deposit 5 nm gold nanoparticles on a square grid via an iterative algorithm, and let the particles diffuse under the influence of an interaction potential until a stable geometry is reached. At every iteration of the algorithm, one randomly chooses either to deposit a new particle (probability p_0) or to make a particle on the grid jump to a more stable neighbor site (probability $p_{i\to j}$ to scatter from site i to site j). These probabilities are respectively given by

$$\begin{cases} p_0 = aNF \\ p_{i\to j} = a\exp\left[-\dfrac{\Delta E_{i\to j}}{k_B T}\right], \end{cases} \tag{83}$$

where a is a constant determined by the normalization condition

$$p_0 + \sum_{i,j\neq i} p_{i\to j} = 1. \tag{84}$$

To determine the relative weight of each process, one needs to pick a random number in the range $[0,1]$. N is the number of particles that remains to be deposited in order to reach the prescribed filling fraction, and F is a constant modelling the experimental deposition rate. k_B is the Boltzmann constant, T the temperature of the surface and $\Delta E_{i\to j}$ the activation energy barrier. Computing $\Delta E_{i\to j}$ is a complex issue for atoms [145,146], and is not possible from first principles for nanometer sized particles. To proceed, we have chosen to deal with a rescaled atomic potential that renormalizes the energy barrier in order to apply to a nanoparticle. We assume that $\Delta E_{i\to j} = \alpha(E_i - E_j)$, where α is a positive dimensionless adjustable parameter taking into account the influence of the substrate and the scaling. E_i is the rescaled "atomic" potential of a particle located on site i, which is allowed to jump to the neighbor site j if $E_i > E_j$. This potential is given by the following expression based on a tight-binding second moment method [147]:

$$E_i = A\sum_{i\neq j} \exp\left[-p\left(\frac{r_{ij}}{r_0}-1\right)\right] - B\left\{\sum_{i\neq j}\exp\left[-2q\left(\frac{r_{ij}}{r_0}-1\right)\right]\right\}^{1/2}. \tag{85}$$

In this expression, r_0 is the size of one nanoparticle, r_{ij} the distance between two sites i and j and A, B, p and q are constants that were tabulated for atoms [147]. The iterative deposition process is stopped when all particles have been deposited (so that the prescribed filling fraction has been reached) and no particle can move to a more stable site. Three

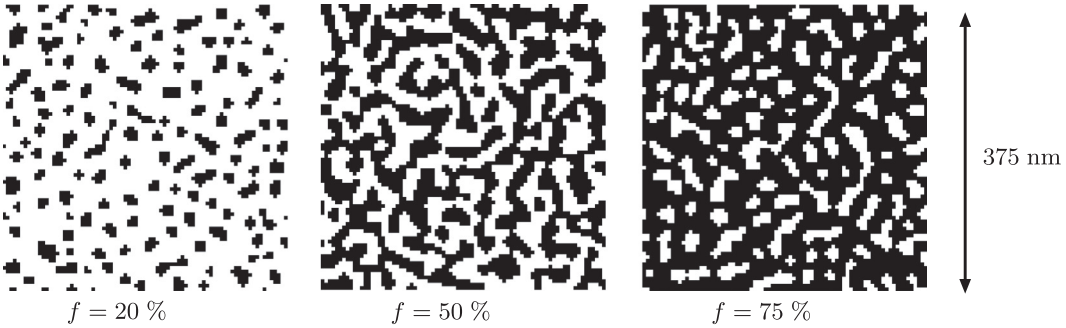

Fig. 26. Numerically generated gold films for three different filling fractions f (gold is represented in dark). The parameters for the computation are $T = 300$ K, $\alpha = 2.58 \times 10^{-2}$, $F = 10^{14}$, $A = 0.2061$ eV, $B = 1.79$ eV, $p = 10.229$, $q = 4.036$. From Ref. [143].

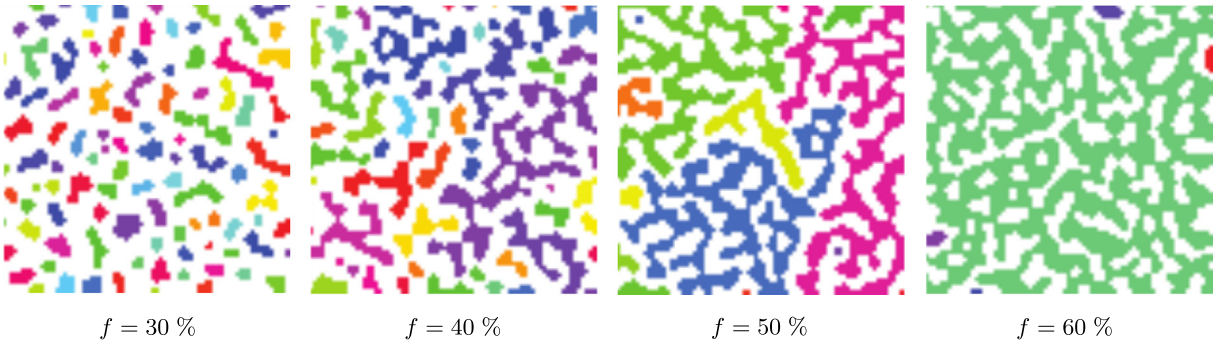

Fig. 27. Disordered films generated numerically for four filling fractions between $f = 30\%$ and $f = 60\%$. Clusters have been labelled using the Hoshen–Kopelman algorithm, a given color identifying a single cluster. The films with filling fractions $f = 50\%$ and $f = 60\%$ are percolated. (For interpretation of the references to color in this figure caption, the reader is referred to the online version of this paper.)

examples of films with size 375×375 nm^2 generated using this algorithm are shown in Fig. 26, for three different surface filling fractions f.

When the filling fraction is large enough, a continuous metallic path appears between two sides of the sample, showing the onset of the percolation phenomenon. The critical filling fraction is called the percolation threshold. It is possible to determine roughly the percolation threshold on the numerical films by using the Hoshen–Kopelman algorithm [148]. This algorithm is designed to label all continuous clusters of the films. Four films generated with different filling fractions are shown in Fig. 27 in which each cluster has been identified by a given color. We observe that the percolation threshold is close to $f = 50\%$.

As seen in Fig. 27, at filling fractions $f \simeq 50\%$, clusters with complex shapes appear. Percolation clusters are known to exhibit a fractal structure that confers a multiscale geometry to the disordered metallic films [149,139]. The perimeter P of a cluster is said to be fractal when $P \propto S^{D/2}$, where S is the cluster surface and D is a non-integer number called fractal dimension [150]. On the other hand, usual Euclidian 2D surfaces have a perimeter satisfying $P \propto S^{1/2}$. It has been shown experimentally that on disordered metallic films, the fractal dimension is $D = 1.88$ [151], a feature that can be checked by generating 100 films numerically the filling fraction of which is $f = 20\%$ and $f = 50\%$. For each film the use of the Hoshen–Kopelman algorithm allows the extraction of the perimeter and surface of all clusters. The surface is defined as the number of pixels and the perimeter as the number of empty neighbor pixels. The location of each cluster in a perimeter/surface diagram in log–log scale and for both filling fractions is shown in Fig. 28. For low filling fractions, every cluster has an Euclidian perimeter (i.e. $D = 1$) while for a filling fraction close to $f = 50\%$, we clearly see the existence of fractal clusters with $D \approx 1.88$ [144,143]. This value is consistent with experimental observations [149,152] and is a strong evidence that the geometrical features of a real film are well described by the numerical generation method. The contour fractal dimension satisfies the relation $1 \leq D \leq 2$ because of the fundamentally two-dimensional approach used for its characterization. Experimental studies of the surface/volume relation taking into account the three-dimensional roughness of the films exist. A fractal dimension $D = 2.26$, satisfying $2 \leq D \leq 3$, has been reported [153]. Although this approach is more complete, it does not contradict the method used here. The very good results obtained in the 2D analysis seem to indicate that the most important physical features are a consequence of the 2D geometrical properties of the film. The ability to reproduce the fractal geometry in the simulations is a key point since the appearance of fractal clusters has been correlated experimentally to the existence of spatially localized modes probed from LDOS fluctuations [60].

8.2.2. Numerical solution of Maxwell's equations in the near field of disordered metallic films

In order to compute the LDOS and the CDOS in the near field of disordered metallic films, one has to solve numerically

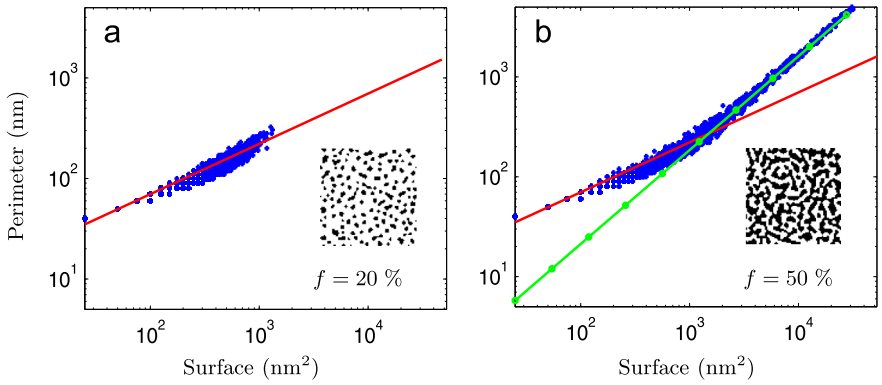

Fig. 28. Distribution in a perimeter/surface diagram of the clusters taken out from 100 numerically generated films. Left: filling fraction $f = 20\%$. Right: filling fraction $f = 50\%$. The red solid line and green dotted line are guides for the eye, corresponding to $P = 7S^{1/2}$ and $P = 0.28S^{1.88/2}$, respectively. From Ref. [143]. (For interpretation of the references to color in this figure caption, the reader is referred to the web version of this paper.)

Maxwell's equations in a complex geometry. The numerical algorithm presented in the following is based on the solution of a volume integral equation for the electric field obtained from a moments method [154]. This method allows one to solve Maxwell's equations in 3D in systems with low symmetry, taking into account polarization and retardation effects. The convergence of the algorithm is only limited by the size of the discretization cells. The electric field in the harmonic regime is solution of the vector Helmholtz equation

$$\nabla \times \nabla \times \mathbf{E}(\mathbf{r},\omega) - k_0^2 \epsilon(\mathbf{r},\omega)\mathbf{E}(\mathbf{r},\omega) = i\omega\mu_0 \mathbf{j}(\mathbf{r},\omega) \tag{86}$$

where $\epsilon(\mathbf{r},\omega)$ is the space and frequency-dependent dielectric function that equals the bulk dielectric function of gold when $\mathbf{r}$ coincides with the gold structure, and the dielectric function of the reference background medium otherwise. $\mathbf{j}(\mathbf{r},\omega)$ is an external current source that generates the incident field. As shown in Appendix A.2, the solution of Eq. (86) can be written using the Green tensor in the reference background medium $\mathbf{G}^E_{\mathrm{ref}}(\mathbf{r},\mathbf{r}',\omega)$ in the form

$$\mathbf{E}(\mathbf{r},\omega) = \mathbf{E}_{\mathrm{ref}}(\mathbf{r},\omega) + k_0^2 \int [\epsilon(\mathbf{r},\omega) - \epsilon_{\mathrm{ref}}(\mathbf{r},\omega)]\mathbf{G}^E_{\mathrm{ref}}(\mathbf{r},\mathbf{r}',\omega)\mathbf{E}(\mathbf{r}',\omega)\, \mathrm{d}^3 r'. \tag{87}$$

This volume integral equation is often denoted as the Lippmann–Schwinger equation. $\mathbf{E}_{\mathrm{ref}}(\mathbf{r},\omega)$ is the reference field given by

$$\mathbf{E}_{\mathrm{ref}}(\mathbf{r},\omega) = i\omega\mu_0 \int \mathbf{G}^E_{\mathrm{ref}}(\mathbf{r},\mathbf{r}',\omega)\mathbf{j}(\mathbf{r}',\omega)\, \mathrm{d}^3 r'. \tag{88}$$

Eq. (87) is an exact integral equation, from which the moments method has been developed [154]. In the following, we consider that the metallic disordered films generated using the kinetic Monte-Carlo algorithm are 5 nm thick and are lying in a reference background medium assumed to be a vacuum. In that case, Eq. (87) reduces to

$$\mathbf{E}(\mathbf{r},\omega) = \mathbf{E}_0(\mathbf{r},\omega) + k_0^2 \int_V [\epsilon(\omega) - 1]\mathbf{G}_0(\mathbf{r}-\mathbf{r}',\omega)\mathbf{E}(\mathbf{r}',\omega)\, \mathrm{d}^3 r' \tag{89}$$

where $\epsilon(\omega)$ is the bulk dielectric function of gold (tabulated in Ref. [155]), V is the volume occupied by the metal and $\mathbf{E}_0(\mathbf{r},\omega)$ is the reference field in vacuum (incident field). $\mathbf{G}_0(\mathbf{r}-\mathbf{r}',\omega)$ is the dyadic Green function in free space given in Eq. (37). In order to solve numerically Eq. (89), we divide the volume V into cubic cells with lateral size $\Delta = 2.5$ nm. On each cell, the field is considered constant, but the Green tensor $\mathbf{G}_0$ is integrated to improve convergence. Note that this integration makes the difference between the moments method and the so-called Discrete Dipole Approximation (DDA), this integration being necessary in order to properly deal with near fields in the presence of resonances, a situation often encountered in plasmonics. Beyond the discretization procedure, this numerical approach is free of any approximation. Denoting the volume of cell number j by V_j, the Green function integrated over the cell reads as

$$\mathbf{G}^{\mathrm{int}}_{ij} = \int_{V_j} \mathbf{G}_0(\mathbf{r}_i - \mathbf{r}',\omega)\, \mathrm{d}^3 r' \tag{90}$$

and the discrete form of Eq. (89) leads to the following linear system equations:

$$\mathbf{E}_i - k_0^2[\epsilon(\omega) - 1]\sum_j \mathbf{G}^{\mathrm{int}}_{ij}\mathbf{E}_j = \mathbf{E}_0(\mathbf{r}_i) \tag{91}$$

where $\mathbf{E}_i$ is the electric field in the cell number i. The computation of the electric field inside the structure thus amounts to solving a linear system of coupled equations. The computation of $\mathbf{G}^{\mathrm{int}}_{ii}$ has to be performed with care, due to the singularity of the dyadic Green function $\mathbf{G}_0$ at the origin. This can be done quasi-analytically in Fourier space using a Weyl expansion, as described in Ref. [156] and detailed in Appendix A.3. The computation of $\mathbf{G}^{\mathrm{int}}_{ij}$ for $j \neq i$ is done numerically. Once $\mathbf{E}_i$ is known, it is straightforward to compute the electric field at any position outside the metal using once again the discrete form of Eq. (89).

8.3. LDOS calculations on disordered plasmonic films

In order to compute the LDOS in the vicinity of the disordered metallic films, we use the numerical algorithm described above in the particular case of an external excitation generated by a point electric-dipole source $\mathbf{p}(\omega)$ placed at position $\mathbf{r}_0$ [i.e. $\mathbf{j}(\mathbf{r}',\omega) = -i\omega\mathbf{p}(\omega)\delta(\mathbf{r}'-\mathbf{r}_0)$]. Computing the

total electric field $\mathbf{E}(\mathbf{r},\omega)$ resulting from the scattering process leads to a computation of the full Green tensor in the presence of the metallic film thanks to the relation

$$\mathbf{E}(\mathbf{r},\omega) = \mu_0\omega^2\mathbf{G}^E(\mathbf{r},\mathbf{r}_0,\omega)\mathbf{p}(\omega). \quad (92)$$

From the Green function, the full or projected LDOS can be computed using Eq. (8) or (13). The radiative and non-radiative components of the LDOS defined in Section 3.5 can also be deduced from the calculation of the radiated and absorbed powers.

8.3.1. Radiative and non-radiative LDOS

We first compute the LDOS at a distance of 40 nm above the film. The calculation is performed for 60 films and for two filling fractions and the results are gathered in a histogram [143]. This specific distance has been chosen since it provides substantial near-field effects and remains compatible with standard computational resources (handling small distances require small cell sizes, thus increasing the size of the linear system to solve numerically). Note that our purpose here is not to describe quantitatively the experiment, but to reproduce and understand the general trends. The results are shown in Fig. 29. The calculated histograms of the total (radiative + non-radiative) LDOS ρ_e/ρ_0 have to be compared to the experimental results presented in Fig. 24 and taken from Ref. [60]. The qualitative agreement is very good. Two major differences are observed as one goes from low to intermediate filling fractions close to the percolation threshold: (1) The mean value of the LDOS increases and (2) the fluctuations of the LDOS are enhanced. In particular, very high values of the LDOS are observed, which is a direct signature of spatially localized modes as discussed in Section 8.1. It is known that the appearance of fractal clusters is correlated to enhanced fluctuations of the near-field intensity and of the LDOS [60,135]. Let us comment on the difference between the experimental and numerical parameters. In the simulations, $\lambda = 780$ nm, a wavelength chosen because fluctuations are known to be stronger in this regime. The filling fractions are also different but correspond to identical regimes (i.e. Euclidian for $f = 20\%$ and fractal for $f = 50\%$). A detailed study of the dependence of the optical properties on the filling fraction would require a more refined algorithm to simulate the growth of the films. Let us stress also that neither the size of the fluorescent beads nor the presence of the substrate is accounted for in the simulation described here.

Looking at the other histograms in Fig. 29 that correspond to the fluctuations of the radiative and non-radiative contributions to the LDOS, we clearly see that at a distance of 40 nm from the surface, LDOS fluctuations are mainly driven by non-radiative channels. To get more insights about this feature, we have plotted in Fig. 30 maps of the total, radiative and non-radiative LDOS. Near the percolation threshold, complicated LDOS structures appear, with local enhancements on sub-wavelength areas confirming the presence of spatially localized modes. Moreover, the similarity between the full LDOS and non-radiative LDOS maps shows that the spatial fluctuations of the LDOS are mainly due to non-radiative channels.

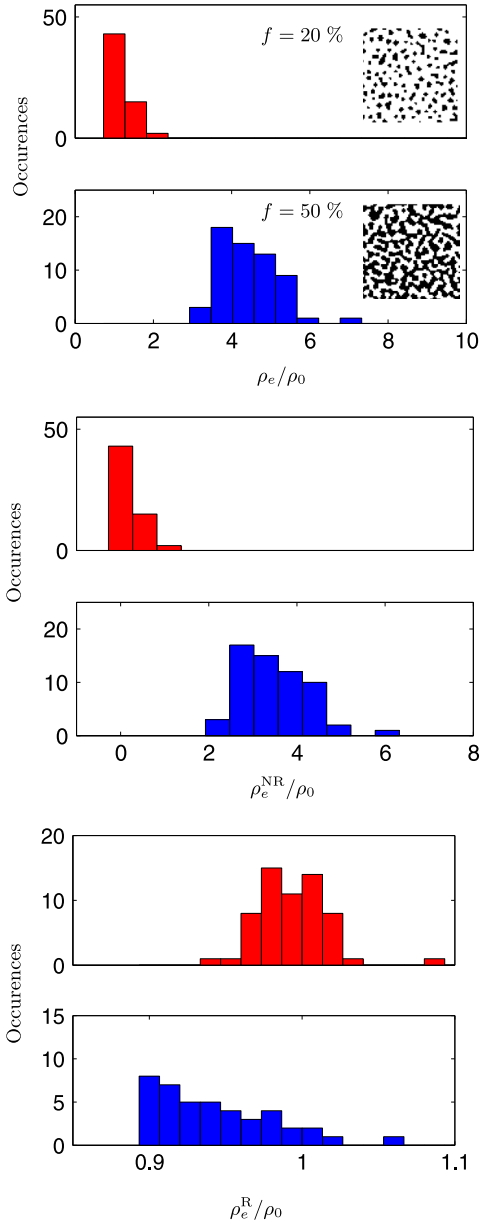

Fig. 29. Histograms of the total (ρ_e), non-radiative (ρ_e^{NR}) and radiative LDOS (ρ_e^R) normalized by the LDOS in vacuum (ρ_0) at 40 nm distance above two series of films of the same filling fraction (red: $f = 20\%$; blue: $f = 50\%$). Every generated film has a lateral size of 375 nm. From Ref. [143]. (For interpretation of the references to color in this figure caption, the reader is referred to the web version of this paper.)

Finally, let us stress that the computations are performed on samples with lateral size on the order of $\lambda/2$, so that the LDOS spatial distributions and maps might be affected by finite-size effects. Although not shown for brevity, we have performed computations with sample sizes from 150 nm to 375 nm. These computations have shown that although the statistical distribution of ρ_e^R is size-dependent, the distributions of ρ_e and ρ_e^{NR} are quite robust.

8.3.2. Distance dependence of the LDOS

We have also performed simulations of LDOS maps at different distances from the film, in the range $d \approx 30$–90 nm

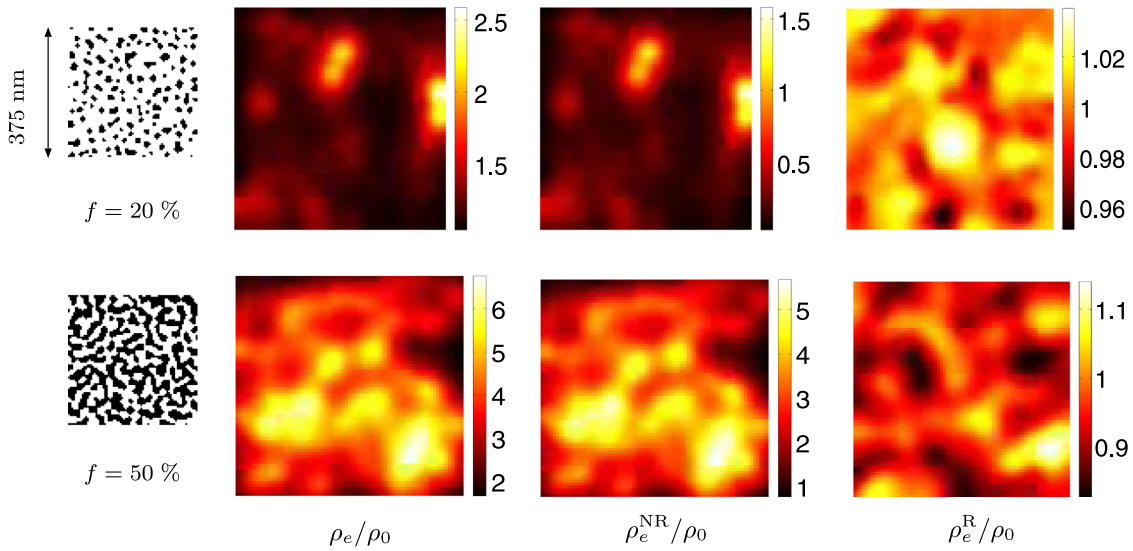

Fig. 30. Maps of the total (ρ_e), non-radiative (ρ_e^{NR}) and radiative LDOS (ρ_e^{R}) normalized by the LDOS in vacuum (ρ_0) at 40 nm distance above two films with filling fractions $f = 20\%$ and $f = 50\%$. The wavelength is $\lambda = 780$ nm. Note that the color scale is different for every map. From Ref. [143]. (For interpretation of the references to color in this figure caption, the reader is referred to the web version of this paper.)

[47]. The results are shown in Fig. 31. In this case, the nanosources (beads) are modelled by orientationally averaged electric dipoles distributed inside a sphere of diameter 25 nm, in order to account for the spatial extent of the beads. The metal film and the nanosources are immersed in a homogeneous glass background that models the glass substrate and the silica spacer. Experimental and numerical data show a very good qualitative agreement for the trends of both the mean and the width of the distributions. The behavior of the mean value can be qualitatively understood replacing the disordered film by an effective homogeneous film. The averaged LDOS close to this absorbing effective homogeneous film is expected to be larger than that on the glass cover slide (the reference) due to an increase of the non-radiative LDOS at short distance, a known behavior close to homogeneous metal surfaces [20,157]. The broadening of the decay rate distribution when the distance to the film decreases is more interesting. As shown above, close to the film, high fluctuations of the LDOS are induced by the disorder of the surface. In particular, substantial changes in the width of the statistical distribution are visible, when moving from short to larger distances from the film. This is due to spatial filtering of optical modes laterally confined on scales below the wavelength. Indeed, the field distribution in a plane at a distance d is exponentially filtered in Fourier space by a factor $\exp[-Kd]$ compared to the distribution at $d = 0$ nm, K being the spatial frequency in the transverse direction (parallel to the film place) [3]. From this simple observation, an order of magnitude of the lateral confinement ξ of the field can be extracted. Since field variations giving rise to substantial fluctuations of the LDOS strongly attenuate between $d = 32.5$ nm and $d = 52.5$ nm, the attenuation length can be estimated to be $1/K = 10$ nm. One can deduce $\xi \approx 2\pi/K \approx 60$ nm as a typical size of hot spots. This is in agreement with orders of magnitude found by near-field optical microscopy [135,158].

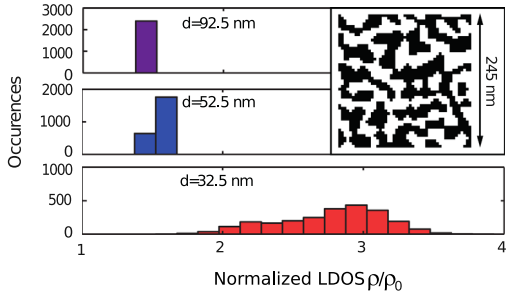

Fig. 31. Calculated distributions of the normalized LDOS ρ_e/ρ_0 for different distances d corresponding to the spacer thickness + 12.5 nm (bead radius). $\lambda = 605$ nm. Inset: Film used in the simulation (black color corresponds to gold). From Ref. [47].

To get more physical insight, we have also computed the mean value and the variance of the distributions of ρ_e/ρ_0, ρ_e^{R}/ρ_0 and ρ_e^{NR}/ρ_0 versus the distance d to the film. Results are shown in Fig. 32. The increase of the averaged value $\langle\rho\rangle$ at short distance is mainly due to the increase of $\langle\rho_e^{NR}\rangle$. This can be understood recalling the effective homogeneous film approach. Indeed, one does not expect significant variations of $\langle\rho_e^{R}\rangle$ on such a distance range, since variations in the radiative rate are due to interference effects that build up on a length scale on the order of $\lambda/2$ that remains large compared to the distance d. Interestingly, the broadening at short distance is also driven by non-radiative decay channels. The confined near-field variations responsible for large near-field fluctuations of the LDOS are chiefly generated by non-radiative modes.

8.4. CDOS and spatial coherence on disordered plasmonic films

Experiments and theory show that disordered fractal metallic films exhibit optical properties that strongly differ from

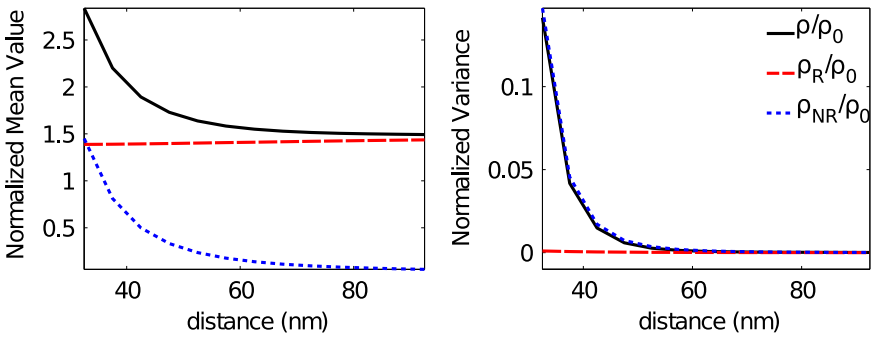

Fig. 32. Mean value (left) and variance (right) of the distribution of ρ_e/ρ_0 (black solid line), $\rho_e^{\mathrm{NR}}/\rho_0$ (blue dotted line) and $\rho_e^{\mathrm{R}}/\rho_0$ (red dashed line) versus the distance d. Adapted from Ref. [47]. (For interpretation of the references to color in this figure caption, the reader is referred to the web version of this paper.)

wthose of bulk metals or ensembles of isolated nanoparticles. In particular, spatial localization of light in subwavelength areas, initially demonstrated using near-field optical microscopy techniques [135,139,158], is an interesting feature, since it provides an efficient way to concentrate visible or near IR light at the nanoscale, and also allows one to strongly modify the absorption of noble metal layers. Spatial localization results from the interplay between surface-plasmon resonances and multiple scattering by fractal percolation clusters. In such a multiscale geometry, that exhibits long-range correlation, simple models as white-noise potentials or effective medium theory are invalid, and apart from direct numerical simulations, it is difficult to develop a multiple scattering theory.

Using a scaling theory in the quasi-static limit, a mechanism based on Anderson localization has been put forward [159]. In the context of electronic transport on percolated systems, Anderson localization has been studied [160,161] and a theory of localization of electromagnetic waves could be developed by mapping the electronic picture. Nevertheless, electromagnetic waves have the possibility to interact with matter both through near-field and far-field interactions, which certainly makes the mechanism different from that put forward for scalar electron waves. Indeed, numerical simulations of light scattering on percolating metallic systems (also called planar random composites) have shown that localized and delocalized plasmonic eigenmodes could coexist [137]. This new picture has been confirmed by computations and measurements of intensity fluctuations in the near field [142,138]. Moreover, a theoretical model has proved the existence of localized modes characterized by algebraic rather than exponential spatial confinement [131]. These results show that the mechanism of spatial localization differs in some essential features from that of Anderson localization of electrons. Measurements of near-field LDOS statistics, described in previous sections, also confirmed the existence of spatially localized modes in the regime dominated by fractal clusters [60].

As far as the spatial extent of the eigenmodes of a complex plasmonic system is concerned, the concept of CDOS appears as a natural tool since it measures the intrinsic spatial coherence of the system. In the following, we present numerical maps of the CDOS in the vicinity of disordered metallic films, and we demonstrate unambiguously an overall spatial squeezing of the optical modes near the percolation threshold, as initially reported in Ref. [128]. To be more quantitative, we introduce the intrinsic coherence length ℓ_{coh} as a measure of this overall spatial extent, and study its dependence on the metal surface filling fraction. Numerically, the computation of the CDOS is not more challenging than the computation of the LDOS. The simulation is performed using the same algorithm (see Section 8.2.2) except that the imaginary part of the Green function $\mathbf{G}^E(\mathbf{r},\mathbf{r}',\omega)$ is computed for $\mathbf{r}\neq\mathbf{r}'$.

Results for two different films corresponding to a regime far from percolation ($f=20\%$) and a second one close to percolation ($f=50\%$) are shown in Fig. 33. First, as a reminder, we have plotted LDOS maps (middle column) calculated in a plane at a distance $z=40$ nm above the films. For low filling fractions (top row), LDOS peaks are observed on top of isolated nanoparticles that are resonant at the observation wavelength. A correspondence between LDOS peaks and the position of one or several nanoparticles is easily made. We have checked that for a different observation wavelength, particles can switch on or off resonance and the position of the LDOS peaks changes, remaining attached to individual particles. The sample behaves as a collection of individual nanoparticles with well identified surface plasmon resonances (since the size and shape of the particles are different, their resonance frequencies do not coincide). In the multiscale resonant regime (bottom row), the LDOS structure is more complex and there is no obvious correspondence between the film topography (composed of fractal clusters in which the concept of individual nanoparticles becomes meaningless) and the localized field enhancements responsible for LDOS fluctuations. This is a known feature of fractal metallic films that has been observed using different kinds of near-field microscopy techniques [135,137,158,162].

Second, we have plotted CDOS maps (right column). The position $\mathbf{r}'$ is fixed and chosen at the center of the sample while the position $\mathbf{r}$ describes a square above the films, and the maps display the CDOS versus $\mathbf{r}$. We recall that the CDOS implicitly sums up the spatial extent of the full set of eigenmodes. Thus it quantifies the ability of a point $\mathbf{r}$ to be connected to the center point $\mathbf{r}'$ through the underlying structure of the optical eigenmodes. In that way, the CDOS allows one to discriminate between two hot spots at $\mathbf{r}$ and $\mathbf{r}'$

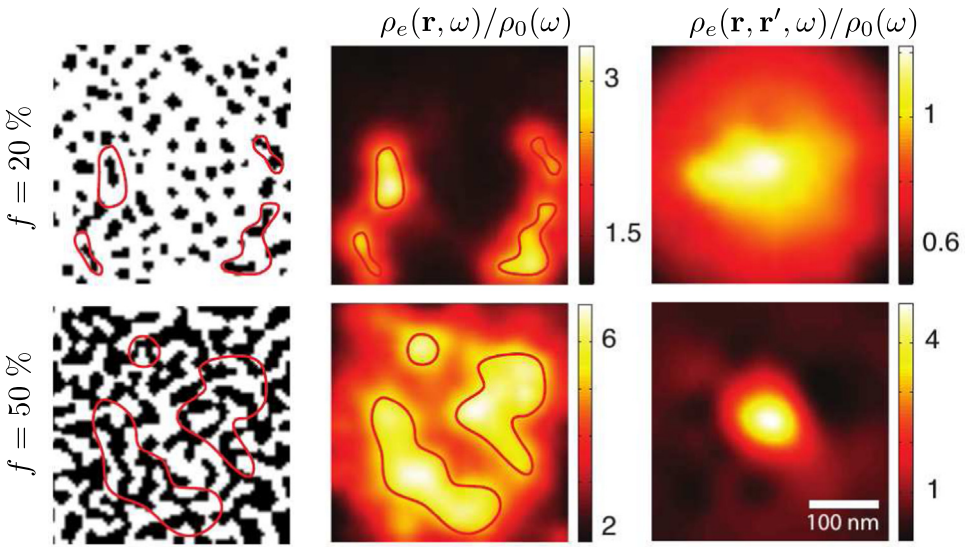

Fig. 33. Left column: geometry of the disordered films generated numerically (with gold in black color). Top: $f = 20\%$, Bottom: $f = 50\%$. Middle column: maps of the normalized LDOS $\rho_e(\mathbf{r},\omega)/\rho_0(\omega)$ calculated in a plane at a distance $z = 40$ nm above the film surface, $\rho_0(\omega)$ being the LDOS in vacuum. Right column: maps of the normalized CDOS $\rho_e(\mathbf{r},\mathbf{r}',\omega)/\rho_0(\omega)$ with $\mathbf{r}'$ fixed at the center of the sample. $\lambda = 780$ nm. Adapted from Ref. [128].

that belong, or not, to at least one identical eigenmode. It is also a natural tool to describe the overall spatial localization in the multiscale resonant regime. In Fig. 33, we clearly see that the extent of the CDOS in the multiscale resonant regime is reduced to a smaller range compared to the case of a film composed of isolated nanoparticles. The reduction of the extent of the CDOS clearly demonstrates an overall spatial squeezing of the eigenmodes close to the percolation threshold. Let us stress that the approach based on the CDOS gives a non-ambiguous description of this overall spatial squeezing, whatever the underlying mechanism. It is based on a concept implicitly related to field–field spatial correlations as in classical spatial coherence theory that seems to carry sufficient information to describe one of the most striking features in the optics of disordered fractal metallic films.

In order to study quantitatively the overall reduction of the spatial extent of eigenmodes in the multiscale resonant regime, we introduce an intrinsic coherence length ℓ_{coh}, defined from the width of the CDOS. More precisely, fixing $\mathbf{r}'$ at the center of the sample, we use polar coordinates in the plane $z = 40$ nm parallel to the sample mean surface to write $\rho_e(\mathbf{r},\mathbf{r}',\omega) = \rho_e(R,\theta,\omega)$ with $R = |\mathbf{r} - \mathbf{r}'|$ and define an angularly averaged CDOS by

$$\overline{\rho}_e(R,\omega) = \frac{1}{2\pi}\int_0^{2\pi} \rho_e(R,\theta,\omega)\,\mathrm{d}\theta. \tag{93}$$

The intrinsic coherence length ℓ_{coh} is defined as the half width at half maximum of $\overline{\rho}_e(R,\omega)$ considered as a function of R. It is important to note that ℓ_{coh} is not necessarily the size of the hot spots observed on the surface, since a given eigenmode can be composed of several hot spots. Two different hot spots separated by a distance smaller than ℓ_{coh} can be intrinsically connected (meaning that they are connected by at least one eigenmode). The ability to clarify this distinction between eigenmodes and hot spots is an essential feature of the CDOS. We have computed the statistical distribution of ℓ_{coh} by generating numerically several realizations of disordered films and by computing the CDOS at the near-field of each film. The average value of $\langle \ell_{\mathrm{coh}} \rangle$ (solid line) and its variance $\mathrm{Var}(\ell_{\mathrm{coh}})$ (error bars) are shown in Fig. 34 as a function of the film filling fraction for two different wavelengths $\lambda = 650$ nm and $\lambda = 780$ nm.

For both wavelengths, the average value $\langle \ell_{\mathrm{coh}} \rangle$ is significantly smaller near the percolation threshold than for lower filling fractions. This is another way to visualize the overall spatial squeezing of eigenmodes in the regime dominated by fractal clusters, with a stronger squeezing at $\lambda = 780$ nm where more pronounced resonances occur [139]. The curve for $\lambda = 780$ nm even shows a minimum near the percolation threshold. Our approach provides a theoretical description of the experimental result presented in Fig. 25. In this figure, a substantial enhancement of the variance of the LDOS distribution is observed, that was qualitatively associated to a decrease of the inverse participation ratio, the latter measuring the spatial extent of localized modes in the structure. We point out that only a qualitative comparison between the curve in Fig. 34 and that in Fig. 25 is possible, since the inverse participation ratio and the intrinsic coherence length are not the same quantities. Moreover, the precise shape of the calculated curves in Fig. 34 might also be influenced by finite-size effects inherent to the numerical simulation, although we have verified that by increasing the size of the sample generated numerically, the general shape of the curve is not affected. The behavior of $\mathrm{Var}(\ell_{\mathrm{coh}})$, that is indicated by the error bars, is also instructive. Strong fluctuations are observed in the regime of isolated nanoparticles. In this regime, both optical modes attached to isolated particles, and delocalized modes spreading over the whole sample, are observed. This is a major difference with the known behavior in quantum electronic transport where only localized wavefunctions can exist on isolated metallic atoms or

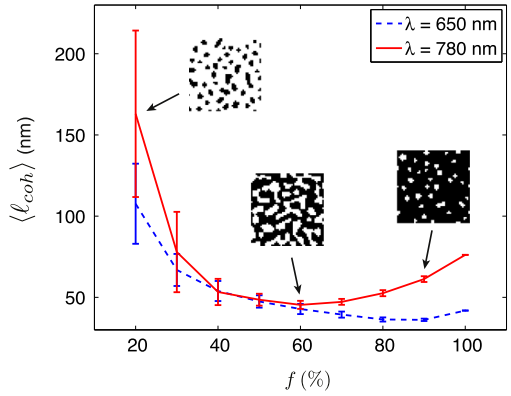

Fig. 34. Averaged value (solid line) and variance (error bars) of the intrinsic coherence length $\ell_{\rm coh}$ calculated at a distance $z=40$ nm above a disordered film, versus the gold filling fraction f. The error bars indicate the real variance of $\ell_{\rm coh}$, and not computation errors due to lack of numerical convergence, the latter being ensured by a sufficiently large set of realizations. Inset: Typical film geometries (black color corresponds to gold). From Ref. [128].

clusters [160,161]. The strong fluctuations in $\ell_{\rm coh}$ reflect the fluctuations of the relative weight of localized and delocalized eigenmodes. Conversely, in the multiscale resonant regime, the reduction of the fluctuations reinforces the assumption of a mechanism based on collective interactions that involve the sample as a whole, and that favors the existence of localized modes. The spatial localization of eigenmodes, and the reduction of fluctuations of the intrinsic coherence length, are two features that illustrate the richness of plasmonics on complex systems.

9. Conclusion

Together with the development of near-field imaging techniques, the progress in the design and realization of nanostructures has made possible an engineering approach towards the control of light emission and absorption at scales below the vacuum wavelength. Nanophotonics, including plasmonics, is at a stage where, on the one hand, fundamental studies of light–matter interaction are possible based on almost ideal experiments (e.g. a single emitter interacting with single shaped nano-objects), and on the other hand, the development of real devices is emerging. The concept of LDOS has become widely used in this field, either to describe basic experiments or as a central quantity in the engineering of systems with targeted functionalities (such as enhanced local or spectral absorption, or antenna-based coupling of quantum emitters). In complex system, i.e. exhibiting a large number of degrees of freedom, the LDOS is also a convenient tool that describes many observables without accounting explicitly for the detailed structure of the photonic eigenmodes. The concept of LDOS does not even require the existence of a basis of eigenmodes, an appealing property in the study of open and dissipative systems often encountered in nanophotonics and plasmonics. Beyond LDOS, the concept of CDOS that we have introduced permits a description of the intrinsic spatial coherence sustained by the system itself, independently of the illumination or excitation conditions. Although the CDOS has been a natural concept in the field of thermal radiation for a long time, it is of much broader interest and, as the LDOS, enters the description of many processes involved in light–matter interaction. Getting familiar with these concepts, and understanding their relevance for fundamental and applied studies in nanophotonics and plasmonics, are the main objectives of this review.

Acknowledgments

This work was supported by LABEX WIFI (Laboratory of Excellence within the French Program “Investments for the Future”) under references ANR-10-LABX-24 and ANR-10-IDEX-0001-02 PSL*. We acknowledge the support from CNRS and DIM NanoK through the allocation of doctoral grants.

Appendix A

A.1. Green function expansion in eigenmodes

In this appendix, we derive the expression of the Green function as a function of the eigenmodes of a closed non-absorbing cavity. This derivation was first suggested in Ref. [14]. Inside the cavity, the permittivity depends on the position $\epsilon(\mathbf{r})$, which is supposed to be real (no absorption) and positive and not depending on the frequency (no dispersion). In that case, a set of discrete eigenmodes exists. Each eigenmode denoted by the subscript n is defined by an eigenvalue ω_n and an eigenvector $\mathbf{e}_n(\mathbf{r})$ obeying the wave equation without any source term

$$\nabla\times\nabla\times\mathbf{e}_n(\mathbf{r})-\epsilon(\mathbf{r})\frac{\omega_n^2}{c^2}\mathbf{e}_n(\mathbf{r})=0. \tag{94}$$

Using the change of variable $\mathbf{u}_n(\mathbf{r})=\sqrt{\epsilon(\mathbf{r})}\mathbf{e}_n(\mathbf{r})$, Eq. (94) becomes

$$\left[\frac{1}{\sqrt{\epsilon(\mathbf{r})}}\nabla\times\nabla\times\frac{1}{\sqrt{\epsilon(\mathbf{r})}}\right]\mathbf{u}_n(\mathbf{r})=\frac{\omega_n^2}{c^2}\mathbf{u}_n(\mathbf{r}). \tag{95}$$

This last expression is interesting because it is an eigenvalue equation with a Hermitian operator thus admitting a set of orthogonal solutions (eigenmodes) satisfying the orthogonality relationship

$$\int\mathbf{u}_m(\mathbf{r})\cdot\mathbf{u}_n^*(\mathbf{r})\,\mathrm{d}^3r=\delta_{mn} \tag{96}$$

where δ stands for the Kronecker-delta operator. As a result, the orthogonality condition for the eigenmodes solution of Eq. (94) reads as

$$\int\epsilon(\mathbf{r})\mathbf{e}_m(\mathbf{r})\cdot\mathbf{e}_n^*(\mathbf{r})\,\mathrm{d}^3r=\delta_{mn}. \tag{97}$$

We now perform the expansion of the Green function on this basis of eigenmodes in the form

$$\mathbf{G}^E(\mathbf{r},\mathbf{r}',\omega)=\sum_n\mathbf{A}_n(\mathbf{r}',\omega)\otimes\mathbf{e}_n(\mathbf{r},\omega). \tag{98}$$

The Green function corresponds to the solution of the wave equation for a Dirac-delta source term thus satisfying

$$\nabla \times \nabla \times \mathbf{G}^E(\mathbf{r},\mathbf{r}',\omega) - \epsilon(\mathbf{r})\frac{\omega_n^2}{c^2}\mathbf{G}^E(\mathbf{r},\mathbf{r}',\omega) = \delta(\mathbf{r}-\mathbf{r}')\mathbf{I}. \quad (99)$$

Inserting Eq. (98) into Eq. (99) yields

$$\sum_n \mathbf{A}_n(\mathbf{r}',\omega) \otimes \left[\nabla \times \nabla \times \mathbf{e}_n(\mathbf{r}) - \epsilon(\mathbf{r})\frac{\omega^2}{c^2}\mathbf{e}_n(\mathbf{r})\right] = \delta(\mathbf{r}-\mathbf{r}')\mathbf{I} \quad (100)$$

which, using Eq. (94), leads to

$$\sum_n \mathbf{A}_n(\mathbf{r}',\omega) \otimes (\omega_n^2-\omega^2)\epsilon(\mathbf{r})\mathbf{e}_n(\mathbf{r}) = c^2\delta(\mathbf{r}-\mathbf{r}')\mathbf{I}. \quad (101)$$

Multiplying both sides of the above equation by $\mathbf{e}_m^*(\mathbf{r})$, integrating over $\mathbf{r}$ and using the orthogonality condition given by Eq. (97) lead to

$$(\omega_n^2-\omega^2)\mathbf{A}_n(\mathbf{r}',\omega) = c^2\mathbf{e}_n^*(\mathbf{r}'). \quad (102)$$

In the sense of distributions, the solution of this equation writes

$$\mathbf{A}_n(\mathbf{r}',\omega) = c^2\mathbf{e}_n^*(\mathbf{r}')\left\{\mathrm{PV}\left[\frac{1}{\omega_n^2-\omega^2}\right] + \varpi\delta(\omega-\omega_n) + \varpi'\delta(\omega+\omega_n)\right\} \quad (103)$$

where ϖ and ϖ' are two complex constants. One way to set ϖ and ϖ' is to consider the case of a very slowly damped harmonic oscillator. Taking the limit when the damping tends to zero should give the exact physical result of the ideal case of a non-damped oscillator. Mathematically speaking, we use the identity

$$\lim_{\eta\to 0^+}\frac{1}{x+i\eta} = \mathrm{PV}\left[\frac{1}{x}\right] - i\pi\delta(x). \quad (104)$$

This implies that $\varpi = i\pi/(2\omega_n)$ and $\varpi' = -i\pi/(2\omega_n)$. The final form of Eq. (103) becomes

$$\mathbf{A}_n(\mathbf{r}',\omega) = c^2\mathbf{e}_n^*(\mathbf{r}')\left\{\mathrm{PV}\left[\frac{1}{\omega_n^2-\omega^2}\right] + \frac{i\pi}{2\omega_n}\delta(\omega-\omega_n) - \frac{i\pi}{2\omega_n}\delta(\omega+\omega_n)\right\}. \quad (105)$$

Dropping the term proportional to $\delta(\omega+\omega_n)$ and corresponding to a non-physical negative frequency, the Green function reads

$$\mathbf{G}^E(\mathbf{r},\mathbf{r}',\omega) = \sum_n c^2\mathbf{e}_n^*(\mathbf{r}') \otimes \mathbf{e}_n(\mathbf{r})\left\{\mathrm{PV}\left[\frac{1}{\omega_n^2-\omega^2}\right] + \frac{i\pi}{2\omega_n}\delta(\omega-\omega_n)\right\}, \quad (106)$$

expression usually reduced to

$$\mathbf{G}^E(\mathbf{r},\mathbf{r}',\omega) = \sum_n \frac{c^2\mathbf{e}_n^*(\mathbf{r}') \otimes \mathbf{e}_n(\mathbf{r})}{\omega_n^2-\omega^2} \quad (107)$$

for the sake of brevity (in this last expression, the expansion into the principal value and the Dirac-delta function is implicit).

A.2. Lippmann–Schwinger equation

In this appendix, we derive the Lippmann–Schwinger equation from the Helmholtz equation. The latter is given by

$$\nabla \times \nabla \times \mathbf{E}(\mathbf{r},\omega) - k_0^2\epsilon(\mathbf{r},\omega)\mathbf{E}(\mathbf{r},\omega) = i\omega\mu_0\mathbf{j}(\mathbf{r},\omega). \quad (108)$$

Let us recall that the electric field is related to the Green tensor of the system by the relation

$$\mathbf{E}(\mathbf{r},\omega) = i\omega\mu_0\int \mathbf{G}^E(\mathbf{r},\mathbf{r}',\omega)\mathbf{j}(\mathbf{r}',\omega)\,\mathrm{d}^3r'. \quad (109)$$

The main idea is to expand the electric field $\mathbf{E}(\mathbf{r},\omega)$ into a term corresponding to an incident field propagating in a reference medium with the same source term, and a term corresponding to the field scattered by the inhomogeneities (difference between the permittivity $\epsilon(\mathbf{r},\omega)$ and the permittivity $\epsilon_{\mathrm{ref}}(\mathbf{r},\omega)$ in the reference medium). The field $\mathbf{E}_{\mathrm{ref}}(\mathbf{r},\omega)$ propagating in the reference medium satisfies

$$\nabla \times \nabla \times \mathbf{E}_{\mathrm{ref}}(\mathbf{r},\omega) - k_0^2\epsilon_{\mathrm{ref}}(\mathbf{r},\omega)\mathbf{E}_{\mathrm{ref}}(\mathbf{r},\omega) = i\omega\mu_0\mathbf{j}(\mathbf{r},\omega). \quad (110)$$

Subtracting Eq. (110) from Eq. (108) leads to an equation on the scattered part of the field $\mathbf{E}_s(\mathbf{r},\omega) = \mathbf{E}(\mathbf{r},\omega) - \mathbf{E}_{\mathrm{ref}}(\mathbf{r},\omega)$ given by

$$\nabla \times \nabla \times \mathbf{E}_s(\mathbf{r},\omega) - k_0^2\epsilon_{\mathrm{ref}}(\mathbf{r},\omega)\mathbf{E}_s(\mathbf{r},\omega) = k_0^2[\epsilon(\mathbf{r},\omega)-\epsilon_{\mathrm{ref}}(\mathbf{r},\omega)]\mathbf{E}(\mathbf{r},\omega)\Big). \quad (111)$$

This equation shows that the scattered field propagates in the reference medium and is generated by a source term proportional to the total field. Thus it can be expressed using the Green tensor in the reference medium $\mathbf{G}^E_{\mathrm{ref}}(\mathbf{r},\mathbf{r}',\omega)$ as follows:

$$\mathbf{E}_s(\mathbf{r},\omega) = k_0^2 \times \int \mathbf{G}^E_{\mathrm{ref}}(\mathbf{r},\mathbf{r}',\omega)[\epsilon(\mathbf{r}',\omega)-\epsilon_{\mathrm{ref}}(\mathbf{r}',\omega)]\mathbf{E}(\mathbf{r}',\omega)\,\mathrm{d}^3r'. \quad (112)$$

Using the expression of the scattered field as a function of the total and incident fields, one obtains

$$\mathbf{E}(\mathbf{r},\omega) = \mathbf{E}_{\mathrm{ref}}(\mathbf{r},\omega) + k_0^2 \times \int \mathbf{G}^E_{\mathrm{ref}}(\mathbf{r},\mathbf{r}',\omega)[\epsilon(\mathbf{r}',\omega)-\epsilon_{\mathrm{ref}}(\mathbf{r}',\omega)]\mathbf{E}(\mathbf{r}',\omega)\,\mathrm{d}^3r'. \quad (113)$$

Eq. (113) is the Lippmann–Schwinger equation and shows that the total electric field is given by the superposition of the incident field given by

$$\mathbf{E}_{\mathrm{ref}}(\mathbf{r},\omega) = i\omega\mu_0\int \mathbf{G}^E_{\mathrm{ref}}(\mathbf{r},\mathbf{r}',\omega)\mathbf{j}(\mathbf{r}',\omega)\,\mathrm{d}^3r' \quad (114)$$

and the scattered field itself depending on the total field (multiple scattering).

A.3. Green's tensor in the moments method

In this appendix the details of the analytical integration of the Green tensor in vacuum $\mathbf{G}_0(\mathbf{r}_i-\mathbf{r}',\omega)$ over the cell number i of volume V_i are presented. This integration is based on a Weyl expansion of the Green tensor exposed in the following.

The Green tensor in vacuum satisfies

$$\nabla \times \nabla \times \mathbf{G}_0(\mathbf{r},\omega) - k_0^2 \mathbf{G}_0(\mathbf{r},\omega) = \delta(\mathbf{r})\mathbf{I}. \tag{115}$$

Taking the Fourier transform of Eq. (115) leads to the expression of the Green tensor in Fourier space as follows:

$$\mathbf{G}_0(\mathbf{k},\omega) = \frac{1}{k^2 - k_0^2}\left[\mathbf{I} - \frac{\mathbf{k}\otimes\mathbf{k}}{k_0^2}\right]. \tag{116}$$

This form allows us to compute the Weyl expansion by performing the inverse Fourier transform of $\mathbf{G}_0(\mathbf{k},\omega)$ along the z coordinate which gives

$$\mathbf{G}_0\left(k_x,k_y,z,\omega\right) = \int_{-\infty}^{+\infty} \mathbf{G}_0(\mathbf{k},\omega)\exp(ik_z z)\frac{\mathrm{d}k_z}{2\pi}. \tag{117}$$

If we denote by k_z^+ the complex number satisfying $(k_z^+)^2 = k_0^2 - k_x^2 - k_y^2$ and $\mathrm{Im}[k_z^+] > 0$, we obtain the following identities from the residue theorem:

$$\int_{-\infty}^{+\infty} \frac{\exp(ik_z z)}{k^2 - k_0^2}\frac{\mathrm{d}k_z}{2\pi} = \frac{i}{2k_z^+}\exp\left(ik_z^+|z|\right), \tag{118}$$

$$\int_{-\infty}^{+\infty} \frac{k_z\exp\left(ik_z z\right)}{k^2 - k_0^2}\frac{\mathrm{d}k_z}{2\pi} = \frac{i\,\mathrm{sign}\,z}{2}\exp\left(ik_z^+|z|\right), \tag{119}$$

$$\int_{-\infty}^{+\infty} \frac{k_z^2\exp\left(ik_z z\right)}{k^2 - k_0^2}\frac{\mathrm{d}k_z}{2\pi} = \frac{ik_z^+}{2}\exp\left(ik_z^+|z|\right) + \delta(z), \tag{120}$$

where sign z denotes the sign of the real z. By using the above identities, Eq. (117) becomes

$$\mathbf{G}_0\left(k_x,k_y,z,\omega\right) = \mathrm{PV}\left[\frac{i\mathbf{M}}{2k_z^+ k_0^2}\exp\left(ik_z^+|z|\right)\right] - \frac{\delta(z)}{k_0^2}\mathbf{e}_z\otimes\mathbf{e}_z \tag{121}$$

where the matrix $\mathbf{M}$ is given by

$$\mathbf{M} = \begin{bmatrix} k_0^2 - k_x^2 & -k_x k_y & -k_x k_z^+\,\mathrm{sign}\,z \\ -k_x k_y & k_0^2 - k_y^2 & -k_y k_z^+\,\mathrm{sign}\,z \\ -k_x k_z^+\,\mathrm{sign}\,z & -k_y k_z^+\,\mathrm{sign}\,z & k_x^2 + k_y^2 \end{bmatrix}. \tag{122}$$

Finally, the Weyl formula gives the expression of the Green function in terms of its Fourier transform with respect to x and y. It reads

$$\mathbf{G}_0(\mathbf{r},\omega) = \frac{i}{2k_0^2}\int\frac{\mathbf{M}}{k_z^+}\exp(ik_x x + ik_y y + ik_z^+|z|)\frac{\mathrm{d}k_x}{2\pi}\frac{\mathrm{d}k_y}{2\pi} - \frac{\delta(\mathbf{r})}{k_0^2}\mathbf{e}_z\otimes\mathbf{e}_z. \tag{123}$$

Eq. (123) is convenient for the integration of the Green tensor $\mathbf{G}_0(\mathbf{r}_i - \mathbf{r}',\omega)$ over the volume V_i. Assuming that a cubic cell of lateral size Δ yields

$$\mathbf{G}_{\mathrm{ii}}^{\mathrm{int}} = \frac{i}{8\pi^2 k_0^2}\iiint_{-\Delta/2}^{\Delta/2}\mathrm{d}^3 r\iint\mathrm{d}k_x\,\mathrm{d}k_y\frac{\mathbf{M}}{k_z^+} \times\exp\left(\mathrm{i}k_x x + \mathrm{i}k_y y + \mathrm{i}k_z^+\Big|z|\right) - \frac{\mathbf{e}_z\otimes\mathbf{e}_z}{k_0^2}. \tag{124}$$

In the following, we focus on the computation of $\mathbf{G}_{ii,zz}^{\mathrm{int}}$ as all diagonal terms are equal and all non-diagonal terms vanish [156]. To do so, we need again some identities:

$$\int_{-\Delta/2}^{\Delta/2}\exp(ik_x x)\,\mathrm{d}x = \frac{2\sin\left(k_x\Delta/2\right)}{k_x}, \tag{125}$$

$$\int_{-\Delta/2}^{\Delta/2}\exp(ik_z^+|z|)\,\mathrm{d}z = \frac{2}{ik_z^+}\left[\exp(ik_z^+\Delta/2) - 1\right], \tag{126}$$

$$\iint\frac{\sin\left(k_x\Delta/2\right)\sin\left(k_y\Delta/2\right)}{k_x k_y}\mathrm{d}k_x\,\mathrm{d}k_y = \pi^2. \tag{127}$$

We use Eqs. (125) and (126) to perform the spatial integration in Eq. (124). Then, we reinject the singularity inside the integral by using Eq. (127) to finally end up with

$$\mathbf{G}_{\mathrm{ii,zz}}^{\mathrm{int}} = \frac{1}{\pi^2 k_0^2}\iint\frac{\sin\left(k_x\Delta/2\right)\sin\left(k_y\Delta/2\right)}{k_x k_y (k_z^+)^2} \times\left[\left(k_x^2 + k_y^2\right)\exp\left(\mathrm{i}k_z^+\Delta/2\right) - k_0^2\right]\mathrm{d}k_x\,\mathrm{d}k_y. \tag{128}$$

We now perform the polar change of variable $k_x = K\cos\theta$, $k_y = K\sin\theta$ which leads to

$$\mathbf{G}_{ii,zz}^{\mathrm{int}} = \frac{1}{\pi^2 k_0^2}\int_{K=0}^{+\infty}\frac{K^2\exp[i\Delta/2\sqrt{k_0^2 - K^2}] - k_0^2}{k_0^2 - K^2}\frac{\mathrm{d}K}{K} \times\int_{\theta=0}^{2\pi}\frac{\sin\left(K\Delta/2\cos\theta\right)\sin\left(K\Delta/2\sin\theta\right)}{\cos\theta\sin\theta}\mathrm{d}\theta. \tag{129}$$

Finally, by making the change of variable $k_z^+ = \sqrt{k_0^2 - K^2}$, one obtains

$$\mathbf{G}_{\mathrm{ii,zz}}^{\mathrm{int}} = \frac{4}{\pi^2 k_0^2}\left[\int_{k_z^+ = k_0}^{0} + \int_{k_z^+ = i0}^{+i\infty}\right]\frac{k_0^2 - K^2\exp\left(\mathrm{i}k_z^+\Delta/2\right)}{\mathrm{K}^2\,\mathrm{k}_z^+}\mathrm{dkz} + \times\int_{\theta=0}^{\pi/2}\frac{\sin\left(K\Delta/2\cos\theta\right)\sin\left(K\Delta/2\sin\theta\right)}{\cos\theta\sin\theta}\mathrm{d}\theta. \tag{130}$$

Going further Eq. (130) analytically is not possible to our knowledge. Thus, a numerical integration is required and this form is the most convenient to proceed.

References

[1] H. Raether, Surface Plasmons, Springer-Verlag, Berlin, 1988.
[2] D. Mills, Surface Polaritons, North-Holland, Amsterdam, 1982.
[3] L. Novotny, B. Hecht, Principle of Nano-Optics, Cambridge University Press, Cambridge, 2006.
[4] S.A. Maier, Plasmonics: Fundamentals and Applications, Springer New-York, 2007.
[5] W.L. Barnes, A. Dereux, T.W. Ebbesen, Nature 424 (2003) 824.
[6] S.A. Maier, H.A. Atwater, J. Appl. Phys. 98 (2005) 011101.
[7] D.K. Gramotnev, S.I. Bozhevolnyi, Nat. Photonics 4 (2010) 83.
[8] J.A. Schuller, E.S. Barnard, W. Cai, Y.C. Jun, J.S. White, M.L. Brongersma, Nat. Mater. 9 (2010) 193.
[9] H.A. Atwater, A. Polman, Nat. Mater. 9 (2010) 865.
[10] M.I. Stockman, Opt. Express 19 (2011) 22029.
[11] L. Novotny, N.F. van Hulst, Nat. Photonics 5 (2011) 83.
[12] K.F. MacDonald, N.I. Zheludev, Laser Photonics Rev. 4 (2010) 562.
[13] M.S. Tame, K.R. McEnery, S.K. Ozdemir, J. Lee, S.A. Maier, M.S. Kim, Nat. Phys. 9 (2013) 329.
[14] R.J. Glauber, M. Lewenstein, Phys. Rev. A 43 (1991) 467–491.

[15] C. Sauvan, J.P. Hugonin, I.S. Maksymov, P. Lalanne, Phys. Rev. Lett. 110 (2013) 237401.
[16] C. Sauvan, J.P. Hugonin, R. Carminati, P. Lalanne, Phys. Rev. A 89 (2014) 043825.
[17] C.-A. Guérin, B. Gralak, A. Tip, Phys. Rev. E 75 (2007) 056601.
[18] J.D. Jackson, Classical Electrodynamics, John Wiley and Sons, New-York, 1962.
[19] J. van Bladel, Singular Electromagnetic Fields and Sources, Oxford University Press, New York, 1991.
[20] R. Carminati, J.J. Greffet, C. Henkel, J.M. Vigoureux, Opt. Commun. 261 (2006) 368.
[21] K. Joulain, R. Carminati, J.P. Mulet, J.J. Greffet, Phys. Rev. B 68 (2003) 245405.
[22] G.S. Agarwal, Phys. Rev. A 11 (1975) 230–242.
[23] J.M. Wylie, J.E. Sipe, Phys. Rev. A 30 (1984) 1185.
[24] M. Born, Atomic Physics, Dover, New York, 1936.
[25] E.M. Purcell, Phys. Rev. 69 (1946) 681.
[26] S. Haroche, in: J. Dalibard, J.M. Raimond, J. Zinn-Justin (Eds.), Cavity Quantum Electrodynamics in Fundamental Systems in Quantum Optics, Elsevier Science Publishers, Amsterdam, 1992.
[27] A.F. Koenderink, Opt. Lett. 35 (2010) 4208.
[28] S.A. Maier, Opt. Express 14 (2010) 1957.
[29] J.J. Greffet, M. Laroche, F. Marquier, Phys. Rev. Lett. 105 (2010) 117701.
[30] C. Weisbuch, M. Nishioka, A. Ishikawa, Y. Arakawa, Phys. Rev. Lett. 69 (1992) 3314.
[31] T. Yoshie, A. Scherer, J. Hendrickson, G. Khitrova, H.M. Gibbs, G. Rupper, C. Ell, O.B. Shchekin, D.G. Deppe, Nature 432 (2004) 200.
[32] E. Peter, P. Senellart, D. Martrou, A. Lemaître, J. Hours, J.M. Gérard, J. Bloch, Phys. Rev. Lett. 95 (2005) 067401.
[33] A. Trügler, U. Hohenester, Phys. Rev. B 77 (2008) 115403.
[34] C. Van Vlack, P.T. Kristensen, S. Hughes, Phys. Rev B 85 (2012) 075303.
[35] D.E. Chang, A.S. Sørensen, E.A. Demler, M.D. Lukin, Nat. Phys. 3 (2007) 807.
[36] S. Aberra Guebrou, C. Symonds, E. Homeyer, J.C. Plenet, Y.N. Gartstein, V.M. Agranovich, J. Bellessa, Phys. Rev. Lett. 108 (2012) 066401.
[37] R. Vasa, W. Wang, R. Pomraenke, M. Lammers, M. Maiuri, C. Manzoni, G. Cerullo, C. Lienau, Nat. Photonics 7 (2013) 128.
[38] L. Sapienza, H. Thyrrestrup, S. Stobbe, P.D. Garcia, S. Smolka, P. Lodahl, Science 327 (5971) (2010) 1352–1355, http://dx.doi.org/10.1126/science.1185080.
[39] J. Gao, S. Combrie, B. Liang, P. Schmitteckert, G. Lehoucq, S. Xavier, X. Xu, K. Busch, D.L. Huffaker, A.D. Rossi, C.W. Wong, Sci. Rep. 3 (2013) 1994.
[40] A. Cazé, R. Pierrat, R. Carminati, Phys. Rev. Lett. 111 (2013) 053901.
[41] D. Cao, A. Cazé, M. Calabrese, R. Pierrat, N. Bardou, S. Collin, R. Carminati, V. Krachmalnicoff, Y. De Wilde, Mapping the radiative and non-radiative local density of states in the near field of a gold nanoantenna, ⟨http://arxiv.org/abs/1401.2858⟩.
[42] E. Castanié, M. Boffety, R. Carminati, Opt. Lett. 35 (2010) 291.
[43] G.W. Ford, W.H. Weber, Phys. Rep. 113 (1984) 195.
[44] I.A. Larkin, M.I. Stockman, M. Achermann, V.I. Klimov, Phys. Rev. B 69 (2004) 121403(R).
[45] G. Colas des Francs, A. Bouhelier, E. Finot, J.C. Weeber, A. Dereux, C. Girard, E. Dujardin, Opt. Express 16 (2008) 17654.
[46] S. Albaladejo, R. Gómez-Medina, L.S. Froufe-Pérez, H. Marinchio, R. Carminati, J.F. Torrado, G. Armelles, A. García-Martín, J.J. Sáenz, Opt. Express 18 (2010) 3556.
[47] E. Castanié, V. Krachmalnicoff, A. Cazé, R. Pierrat, Y. De Wilde, R. Carminati, Opt. Lett. 37 (2012) 3006–3008.
[48] J.E. Sipe, J. Opt. Soc. Am. B 4 (1987) 481.
[49] K. Joulain, J. Mulet, F. Marquier, R. Carminati, J.J. Greffet, Surf. Sci. Rep. 57 (2005) 59.
[50] P. Leung, J. Vielma, J. Chem. Phys. 126 (2007) 194704.
[51] P.O. Chapuis, S. Volz, C. Henkel, K. Joulain, J.J. Greffet, Phys. Rev. B 77 (2008) 035431.
[52] R. Esteban, A.G. Borisov, P. Nordlander, J. Aizpurua, Nat. Commun. 3 (2012) 825.
[53] K.J. Savage, M.M. Hawkeye, R. Esteban, A.G. Borisov, J. Aizpurua, J. Baumberg, Nature 491 (2012) 574.
[54] P.V. Ruijgrok, R. Wüest, A.A. Rebane, A. Renn, V. Sandoghdar, Opt. Express 18 (6) (2010) 6360–6365, http://dx.doi.org/10.1364/OE.18.006360.
[55] M.D. Birowosuto, S.E. Skipetrov, W.L. Vos, A.P. Mosk, Phys. Rev. Lett. 105 (2010) 013904, http://dx.doi.org/10.1103/PhysRevLett.105.013904.
[56] R. Sapienza, P. Bondareff, R. Pierrat, B. Habert, R. Carminati, N.F. van Hulst, Phys. Rev. Lett. 106 (2011) 163902, http://dx.doi.org/10.1103/PhysRevLett.106.163902.
[57] K. Hennessy, A. Badolato, M. Winger, D. Gerace, M. Atatüre, S. Gulde, S. Fält, E.L. Hu, A. Imamoglu, Nature 445 (2007) 896–899.
[58] F.A. Inam, T. Gaebel, C. Bradac, L. Stewart, M.J. Withford, J.M. Dawes, J.R. Rabeau, M.J. Steel, New J. Phys. 13 (7) (2011) 073012.
[59] S. Smolka, H. Thyrrestrup, L. Sapienza, T.B. Lehmann, K.R. Rix, L.S. Froufe-Pérez, P.D. Garcia, P. Lodahl, New J. Phys. 13 (6) (2011) 063044.
[60] V. Krachmalnicoff, E. Castanié, Y. De Wilde, R. Carminati, Phys. Rev. Lett. 105 (2010) 183901.
[61] I. Mallek-Zouari, S. Buil, X. Quélin, B. Mahler, B. Dubertret, J.-P. Hermier, Appl. Phys. Lett. 97 (5) (2010) doi: http://dx.doi.org/10.1063/1.3467264.
[62] D. Canneson, I. Mallek-Zouari, S. Buil, X. Quélin, C. Javaux, B. Mahler, B. Dubertret, J.P. Hermier, Phys. Rev. B 84 (2011) 245423, http://dx.doi.org/10.1103/PhysRevB.84.245423.
[63] S. Kühn, C. Hettich, C. Schmitt, J.-P. Poizat, V. Sandoghdar, J. Microsc. 202 (1) (2001) 2–6, http://dx.doi.org/10.1046/j.1365-2818.2001.00829.x.
[64] A. Cuche, O. Mollet, A. Drezet, S. Huant, Nano Lett. 10 (11) (2010) 4566–4570, http://dx.doi.org/10.1021/nl102568m.
[65] A.W. Schell, P. Engel, J.F.M. Werra, C. Wolff, K. Busch, O. Benson, Nano Lett. 14 (5) (2014) 2623–2627, http://dx.doi.org/10.1021/nl500460c.
[66] M. Frimmer, Y. Chen, A.F. Koenderink, Phys. Rev. Lett. 107 (2011) 123602, http://dx.doi.org/10.1103/PhysRevLett.107.123602.
[67] V. Krachmalnicoff, D. Cao, A. Cazé, E. Castanié, R. Pierrat, N. Bardou, S. Collin, R. Carminati, Y. De Wilde, Opt. Express 21 (9) (2013) 11536–11545, http://dx.doi.org/10.1364/OE.21.011536.
[68] J. Michaelis, C. Hettich, J. Mlynek, V. Sandoghdar, Nature 405 (2000) 325.
[69] P. Maletinsky, S. Hong, M.S. Grinolds, B. Hausmann, M.D. Lukin, R.-L. Walsworth, M. Loncar, A. Yacoby, Nat. Nanotechnol. 7 (5) (2012) 320–324.
[70] B.C. Buchler, T. Kalkbrenner, C. Hettich, V. Sandoghdar, Phys. Rev. Lett. 95 (2005) 063003, http://dx.doi.org/10.1103/PhysRevLett.95.063003.
[71] J. Berthelot, S.S. Aćimović, M.L. Juan, M.P. Kreuzer, J. Renger, R. Quidant, Nat. Nanotechnol. 9 (2014) 295.
[72] J.N. Farahani, D.W. Pohl, H.J. Eisler, B. Hecht, Phys. Rev. Lett. 95 (2005) 017402, http://dx.doi.org/10.1103/PhysRevLett.95.017402.
[73] A. Singh, G. Calbris, N.F. van Hulst, Nano Lett. 14 (2014) 4715.
[74] T. van der Sar, E.C. Heeres, G.M. Dmochowski, G. de Lange, L. Robledo, T.H. Oosterkamp, R. Hanson, Appl. Phys. Lett. 94 (17) (2009) doi: http://dx.doi.org/10.1063/1.3120558.
[75] D. Englund, B. Shields, K. Rivoire, F. Hatami, J. Vuckovic, H. Park, M.D. Lukin, Nano Lett. 10 (10) (2010) 3922–3926, http://dx.doi.org/10.1021/nl101662v.
[76] A.W. Schell, G. Kewes, T. Hanke, A. Leitenstorfer, R. Bratschitsch, O. Benson, T. Aichele, Opt. Express 19 (8) (2011) 7914–7920, http://dx.doi.org/10.1364/OE.19.007914.
[77] S. Kumar, N.I. Kristiansen, A. Huck, U.L. Andersen, Nano Lett. 14 (2) (2014) 663–669, http://dx.doi.org/10.1021/nl403907w.
[78] F.J. García de Abajo, Rev. Mod. Phys. 82 (2010) 209.
[79] M. Kociak, O. Stéphan, A. Gloter, L.F. Zagonel, L.H. Tizei, M. Tencé, K. March, J.D. Blazit, Z. Mahfoud, A. Losquin, S. Meuret, C. Colliex, C. R. Phys. 15 (2014) 158–175 http://dx.doi.org/http://dx.doi.org/10.1016/j.crhy.2013.10.003.
[80] M. Kociak, O. Stephan, Chem. Soc. Rev. 43 (2014) 3865–3883.
[81] A. Losquin, Surface plasmon modes revealed by fast electron based spectroscopies: from simple model to complex systems (Ph.D. thesis), Université Paris Sud, 2013.

[82] A. Losquin, S. Camelio, D. Rossouw, M. Besbes, F. Pailloux, D. Babonneau, G.A. Botton, J.-J. Greffet, O. Stéphan, M. Kociak, Phys. Rev. B 88 (2013) 115427, http://dx.doi.org/10.1103/PhysRevB.88.115427.
[83] M. Kuttge, E.J.R. Vesseur, A.F. Koenderink, H.J. Lezec, H.A. Atwater, F.J. García de Abajo, A. Polman, Phys. Rev. B 79 (2009) 113405, http://dx.doi.org/10.1103/PhysRevB.79.113405.
[84] R. Sapienza, T. Coenen, J. Renger, M. Kuttge, N.F. Van Hulst, A. Polman, Nat. Mater. 11 (2012) 781.
[85] V.M. Shalaev, Nat. Photonics 1 (2007) 41.
[86] C.M. Soukoulis, M. Wegener, Nat. Photonics 5 (2011) 523.
[87] J.B. Pendry, A. Aubry, D.R. Smith, S.A. Maier, Science 337 (2012) 549.
[88] C. Enkrich, M. Wegener, S. Linden, S. Burger, L. Zschiedrich, F. Schmidt, J.F. Zhou, T. Koschny, C.M. Soukoulis, Phys. Rev. Lett. 95 (2005) 203901.
[89] M. Husnik, M.W. Klein, N. Feth, M. Koenig, J. Niegemann, K. Busch, S. Linden, M. Wegener, Nat. Photonics 2 (2008) 614.
[90] I. Sersic, M. Frimmer, A.F. Koenderink, Phys. Rev. Lett. 103 (2009) 213902.
[91] I. Sersic, C. Tuambilangana, T. Kampfrath, A.F. Koenderink, Phys. Rev. B 83 (2011) 245102.
[92] A. Kwadrin, A.F. Koenderink, Phys. Rev. B 87 (2013) 125123.
[93] S. Karaveli, R. Zia, Opt. Lett. 35 (2010) 3318.
[94] S. Karaveli, R. Zia, Phys. Rev. Lett. 106 (2011) 193004.
[95] T.H. Taminiau, S. Karaveli, N.F. van Hulst, R. Zia, Nat. Commun. 3 (2012) 979.
[96] N. Noginova, R. Hussain, M.A. Noginov, J. Vella, A. Urbas, Opt. Express 21 (2013) 23087.
[97] L. Aigouy, A. Cazé, P. Gredin, M. Mortier, R. Carminati, Mapping and quantifying electric and magnetic dipole luminescence at the nanoscale, Phys. Rev. Lett. 113 (2014) 076101, http://dx.doi.org/10.1103/PhysRevLett.113.076101 ⟨http://arxiv.org/abs/1404.1369⟩.
[98] Y. De Wilde, F. Formanek, R. Carminati, B. Gralak, P.-A. Lemoine, K. Joulain, J.P. Mulet, Y. Chen, J.J. Greffet, Nature 444 (2006) 740.
[99] S.M. Rytov, Y.A. Kravtsov, V.I. Tatarskii, Principles of Statistical Radiophysics, vol. 3, Springer-Verlag, Berlin, 1989.
[100] L.D. Landau, E.M. Lifshitz, L.P. Pitaevskii, Statistical Physics, vol. 1, Pergamon Press, Oxford, 1980.
[101] A.V. Shchegrov, K. Joulain, R. Carminati, J.J. Greffet, Phys. Rev. Lett. 85 (2000) 1548.
[102] R. Carminati, J.J. Greffet, Phys. Rev. Lett. 82 (1999) 1660.
[103] J.-J. Greffet, R. Carminati, K. Joulain, J.-P. Mulet, S. Mainguy, Y. Chen, Nature 416 (2002) 61.
[104] M. Laroche, C. Arnold, F. Marquier, R. Carminati, J.J. Greffet, S. Collin, N. Bardou, J.L. Pelouard, Opt. Lett. 30 (2005) 2623.
[105] C. Arnold, F. Marquier, M. Garin, F. Pardo, S. Collin, N. Bardou, J. L. Pelouard, J.J. Greffet, Phys. Rev. B 86 (2012) 035316.
[106] Y. Kajihara, K. Kosaka, S. Komiyama, Rev. Sci. Instrum. 81 (2010) 033706.
[107] A.C. Jones, M.B. Raschke, Nano Lett. 12 (2012) 1475.
[108] A. Babuty, K. Joulain, P.-O. Chapuis, J.-J. Greffet, Y. De Wilde, Phys. Rev. Lett. 110 (2013) 146103.
[109] A.C. Jones, B.T. OćallahanH.U. Yang, M.B. Raschke, Prog. Surf. Sci. 88 (2013) 349.
[110] F. Peragut, J.-B. Brubach, P. Roy, Y. De Wilde, Appl. Phys. Lett. 104 (2014) 251118.
[111] B.T. OćallahanW.E. Lewis, A.C. Jones, M.B. Raschke, Phys. Rev. B 89 (2014) 245446.
[112] R. Carminati1, J.J. Sáenz, Phys. Rev. Lett. 84 (2000) 5156.
[113] K. Joulain, P. Ben-Abdallah, P.-O. Chapuis, Y. De Wilde, A. Babuty, C. Henkel, J. Quant. Spectrosc. Radiat. Transfer 136 (2014) 1.
[114] R.L. Olmon, B. Slovick, T.W. Johnson, D. Shelton, S.-H. Oh, G.D. Boreman, M.B. Raschke, Phys. Rev. B 86 (2012) 235147.
[115] J.P. Tetienne, A. Bousseksou, D. Costantini, R. Colombelli, A. Babuty, I. Moldovan-Doyen, Y. De Wilde, C. Sirtori, G. Beaudoin, L. Largeau, O. Mauguin, I. Sagnes, Appl. Phys. Lett. 97 (2010) 211110.
[116] M. Schnell, A. Garcia-Etxarri, J. Alkorta, J. Aizpurua, R. Hillenbrand, Nano Lett. 10 (2010) 3524.
[117] P.O. Chapuis, M. Laroche, S. Volz, J.J. Greffet, Appl. Phys. Lett. 92 (2008) 201906.
[118] W. Spitzer, D. Kleinman, D. Walsh, Phys. Rev. 113 (1959) 127.
[119] A. Bousseksou, A. Babuty, J.P. Tetienne, I. Moldovan-Doyen, R. Braive, G. Beaudoin, I. Sagnes, Y. De Wilde, R. Colombelli, Opt. Exp. 20 (2012) 13738.
[120] L. Mandel, E. Wolf, Optical Coherence and Quantum Optics, Cambridge University Press, Cambridge, 1995.
[121] R.L. Weaver, O.I. Lobkis, Phys. Rev. Lett. 87 (2001) 134301.
[122] E. Larose, L. Margerin, A. Derode, B.A. van Tiggelen, M. Campillo, N. Shapiro, A. Paul, L. Stehly, M. Tanter, Geophysics 71 (2006) SI11–SI21.
[123] T. Setala, K. Blomstedt, M. Kaivola, A.T. Friberg, Phys. Rev. E 67 (2003) 026613.
[124] P. Sheng, Introduction to Wave Scattering, Localization and Mesoscopic Phenomena, Academic Press, San Diego, 1995.
[125] R. Carminati, Phys. Rev. A 81 (2010) 053804.
[126] K. Vynck, R. Pierrat, R. Carminati, Phys. Rev. A 89 (2014) 013842.
[127] A. Dogariu, R. Carminati, Electromagnetic field correlations in three-dimensional speckles, Phys. Rep., http://dx.doi.org/10.1016/j.physrep.2014.11.003, in press.
[128] A. Cazé, R. Pierrat, R. Carminati, Phys. Rev. Lett. 110 (2013) 063903.
[129] T. Setälä, K. Blomstedt, M. Kaivola, A.T. Friberg, Phys. Rev. E 67 (2003) 026613.
[130] G. Boudarham, M. Kociak, Phys. Rev. B 85 (2012) 245447.
[131] V.A. Markel, J. Phys.: Condens. Matter 18 (2006) 11149.
[132] E. Wolf, Introduction to the Theory of Coherence and Polarization of Light, Cambridge University Press, Cambridge, 2007.
[133] S. Buil, J. Aubineau, J. Laverdant, X. Quélin, J. Appl. Phys. 100 (6) (2006) http://dx.doi.org/10.1063/1.2335664.
[134] M.I. Stockman, Phys. Rev. E 56 (1997) 6494–6507, http://dx.doi.org/10.1103/PhysRevE.56.6494.
[135] S. Grésillon, L. Aigouy, A.C. Boccara, J.C. Rivoal, X. Quelin, C. Desmarest, P. Gadenne, V.A. Shubin, A.K. Sarychev, V. M. Shalaev, Phys. Rev. Lett. 82 (1999) 4520.
[136] A.K. Sarychev, V.M. Shalaev, Phys. Rep. 335 (6) (2000) 275–371 http://dx.doi.org/10.1016/S0370-1573(99)00118-0.
[137] M.I. Stockman, S.V. Faleev, D.J. Bergman, Phys. Rev. Lett. 87 (2001) 167401.
[138] K. Seal, D.A. Genov, A.K. Sarychev, H. Noh, V.M. Shalaev, Z.C. Ying, X. Zhang, H. Cao, Phys. Rev. Lett. 97 (2006) 206103.
[139] V M. Shalaev, Nonlinear Optics of Random Media: Fractal Composites and Metal-Dielectric Films, Springer Tracts in Modern Physics, Berlin, Heidelberg, 2000.
[140] A.D. Mirlin, Phys. Rep. 326 (5–6) (2000) 259–382 doi: http://dx.doi.org/10.1016/S0370-1573(99)00091-5.
[141] L. Zekri, R. Bouamrane, N. Zekri, F. Brouers, J. Phys.: Condens. Matter 12 (3) (2000) 283.
[142] D.A. Genov, A.K. Sarychev, V.M. Shalaev, Phys. Rev. E 67 (2003) 056611.
[143] A. Cazé, R. Pierrat, R. Carminati, Photonics Nanostruct. Fundam. Appl. 10 (2012) 339–344.
[144] J. Aubineau, Modélisation de couches minces métalliques fractales et calculs d'exaltations de champs électromagnétiques (Ph.D. thesis), Université de Versailles Saint-Quentin, 2005.
[145] R. Ferrando, G. Tréglia, Phys. Rev. B 50 (1994) 12104–12117.
[146] C. Mottet, R. Ferrando, F. Hontinfinde, A.C. Levi, Surf. Sci. 417 (1998) 220–237.
[147] F. Cleri, V. Rosato, Phys. Rev. B 48 (1993) 22–33.
[148] J. Hoshen, R. Kopelman, Phys. Rev. B 14 (1976) 3438–3445.
[149] R.F. Voss, R.B. Laibowitz, E.I. Allessandrini, Phys. Rev. Lett. 49 (1982) 1441–1444.
[150] B. Mandelbrot, The Fractal Geometry of Nature, Freeman, New York, USA, 1983.
[151] P. Gadenne, Croissance de couches minces d'or : propriétés optiques, conductivité électrique et étude morphologique (Ph.D. thesis), University of Paris VI, 1986.
[152] E. Castanié, Émission dipolaire et absorption en champ proche de nanostructures (Ph.D. thesis), Université Pierre et Marie Curie, 2011.
[153] S.I. Bozhevolnyi, B. Vohnsen, A.V. Zayats, I.I. Smolyaninov, Surf. Sci. 356 (1996) 268–274.

[154] R.F. Harrington, Field Computations by Moment Methods, IEEE Press, New-York, 1992.
[155] E.D. Palik, Handbook of Optical Constants of Solids, Academic Press, New-York, 1985.
[156] P.C. Chaumet, A. Rahmani, Phys. Rev. E 70 (2004) 036606.
[157] R.R. Chance, A. Prock, R. Silbey, Adv. Chem. Phys. 37 (1978) 1.
[158] J. Laverdant, S. Buil, B. Bérini, X. Quélin, Phys. Rev. B 77 (2008) 165406.
[159] A.K. Sarychev, V.A. Shubin, V.M. Shalaev, Phys. Rev. B 60 (1999) 16389–16408.
[160] C.M. Soukoulis, Q. Li, G.S. Grest, Phys. Rev. B 45 (1992) 7724–7729.
[161] I. Chang, Z. Lev, A.B. Harris, J. Adler, A. Aharony, Phys. Rev. Lett. 74 (1995) 2094–2097.
[162] C. Awada, G. Barbillon, F. Charra, L. Douillard, J.J. Greffet, Phys. Rev. B 85 (2012) 045438.